Differential cross section measurement and phase shift analysis for $\Sigma^+ p$ elastic scattering

Takuya Nanamura

Abstract

By investigating interactions between octet baryons, we can extend the nuclear force based on the flavor SU(3) symmetry and reveal the role of dynamics of quarks and gluons in the short-range part of baryon-baryon interaction (BB interaction). In particular, it is expected that ΣN interaction is strongly affected by the Pauli principle at the quark level (quark Pauli effect). A larger repulsive core is expected to be observed in the $^3S_1$ channel of the Σ^+p system than in the core of nuclear force. Unfortunately, the predicted strengths of the repulsive force changes so much according to theoretical models. Reliable experimental input is needed to understand the BB interactions. A scattering experiment is the most direct method to investigate the two-body BB interactions. However, hyperon-nucleon scattering experiments have been difficult for a long time due to a short lifetime of hyperons, typically 10^{-10} s. The past scattering data have a large uncertainty due to poor statistics.

Recently, we successfully performed a novel $\Sigma^\pm p$ scattering experiment with high-statistics of more than a few thousands of the scattering events at the J-PARC Hadron Experimental Facility by 2020 June. In this experiment, we measured the differential cross sections for the $\Sigma^\pm p$ elastic scattering and $\Sigma^- p \to \Lambda n$ inelastic scattering. In this thesis, the data taking and results of the Σ^+p elastic scattering is reported.

A liquid hydrogen target was used for both a Σ^+ production target and Σ^+p scattering target. In the former process, Σ^+ particles were produced via the $\pi^+p \to K^+\Sigma^+$ reaction induced by a high intensity π^+ beam with a momentum of 1.41 GeV/c. Momentum range of the produced Σ^+ were from 0.44-0.80 GeV/c in the laboratory frame, where typical distances between two particles in the Σ^+p scatterings are 0.8-0.5 fm and they would overlap each other. In total, 4.9×10^7 Σ^+ production events were tagged. The recoil proton from the Σ^+p scattering and proton from the $\Sigma^+ \to p\pi^0$ decay were detected with a detector system CATCH, surrounding a target. The Σ^+p scattering events were identified by the kinematical consistency check method. In total, approximately 2400 Σ^+p elastic scattering events were identified.

The differential cross sections of the Σ^+p scattering in a momentum range 0.44 to 0.80 GeV/c were derived, with the small uncertainties of approximately 15% and a fine angular step of $\Delta \cos\theta_{\rm CM} = 0.1$. Owing to precise data points and the simple representation of the Σ^+p system with respect to the flavor SU(3) symmetry, we could reveal the strength of interaction in the $^3S_1$ and $^1P_1$ states quantitatively with the phase shift analysis. The phase shift of the $^3S_1$ state, where a large repulsive core was predicted owing to the quark Pauli effect, was determined with a precision of approximately 4 degrees for each of three momentum regions. The absolute values of the phase shift for the $^3S_1$ state range from $20^\circ < |\delta_{^3S_1}| < 35^\circ$ in the present momentum range, which suggests the repulsive force is relatively moderate. Since theoretical models describing BB interaction has been built on little hyperon-proton scattering data, these data will be essential inputs in constructing realistic BB interaction models.

Contents

1 Introduction **4**
- 1.1 Baryon-Baryon interaction and importance of ΣN interaction 4
  - 1.1.1 Quark Pauli effect in the quark cluster model (QCM) 5
- 1.2 Equation of state for neutron stars, hyperon puzzle, and three body force . 6
- 1.3 Theoretical Models for BB interaction 8
  - 1.3.1 Nijmegen Extended-soft-core Model (ESC) 8
  - 1.3.2 Chiral Effective Field Theory (χEFT) 8
  - 1.3.3 BB interaction including QCM 8
  - 1.3.4 Lattice QCD 9
  - 1.3.5 Theoretical predictions for $\Sigma N(I = 3/2, {}^3S_1)$ interaction 10
- 1.4 Previous experimental studies on ΣN and Σ-nucleus interaction 11
  - 1.4.1 $\Sigma^{\pm} p$ scattering experiment 11
  - 1.4.2 Σ hypernuclei and quasi-free Σ production 11
  - 1.4.3 Σ^- atom 13
  - 1.4.4 Femtoscopy technique 13
- 1.5 Present experiment: J-PARC E40 experiment 14
- 1.6 Thesis composition 15

2 Experiment **17**
- 2.1 Outline 17
- 2.2 J-PARC and Hadron Experimental Facility 17
- 2.3 K1.8 beam line 19
- 2.4 K1.8 beam-line spectrometer 21
  - 2.4.1 Hodoscopes in the K1.8 beam-line spectrometer 23
  - 2.4.2 Trackers in the K1.8 beam-line spectrometer 23
- 2.5 KURAMA spectrometer 24
  - 2.5.1 Detectors in the KURAMA spectrometer 26
- 2.6 Liquid-hydrogen (LH_2) target 33
- 2.7 CATCH 33
  - 2.7.1 Detectors of CATCH 34
- 2.8 Trigger 36
- 2.9 DAQ 38
- 2.10 Data Summary 39

3 Analysis flow and Monte Carlo simulation **40**
- 3.1 Analysis flow 40
- 3.2 Monte Carlo simulations 41

4 Analysis-I:Analysis of spectrometers and CATCH **44**
4.1 π^+ analysis using the K1.8 beam-line spectrometer 44
4.1.1 BFT analysis 45
4.1.2 Local Tracking for BCout (BCout Tracking) 46
4.1.3 K1.8 Tracking 47
4.2 K^+ analysis using the KURAMA spectrometer 48
4.2.1 SDCin Tracking 50
4.2.2 SDCout Tracking 52
4.2.3 KURAMA Tracking 53
4.2.4 K^+ identification 54
4.3 Σ^+ identification with (π^+, K^+) analysis 56
4.4 CATCH for the recoil/decay protons 59
4.4.1 Outline 59
4.4.2 CFT Tracking 59
4.4.3 Energy measurement with CFT and BGO 64
4.4.4 Particle identification 67
4.5 Evaluations of the system specification by combined analysis 68
4.5.1 The vertex resolution evaluation of the spectrometer system using the $\pi^+ p \to \pi^+\pi^+\pi^- p$ reaction 68
4.5.2 The momentum resolution evaluation of KURAMA using the $\pi^+ p$ elastic scattering 70
4.5.3 The detection probability estimation for accidental proton by CATCH 71

5 Analysis-II:Identification of the $\Sigma^+ p$ scattering events **72**
5.1 Outline 72
5.2 Kinematical consistency check method 72
5.2.1 Kinematical consistency check for the decay proton from $\Sigma^+ \to p\pi^0$ decay 72
5.2.2 Kinematical consistency check for the decay proton of pp scattering following the $\Sigma^+ \to p\pi^0$ decay 74
5.2.3 Kinematical consistency check for the recoil proton from the $\Sigma^+ p$ scattering 75
5.3 Cut conditions to select the $\Sigma^+ p$ scattering events 78
5.3.1 Vertex cut and closest distance cut 79
5.3.2 Missing mass cut to select the scattered Σ^+ decay 80
5.3.3 Kinematical cut for secondary pp scattering 80
5.3.4 Kinematical cut for $\pi^+ p$ elastic scattering 81
5.3.5 $\Sigma^+ p$ scattering identification after all cuts 82
5.4 Estimation of the number of $\Sigma^+ p$ scattering events 83

6 Analysis III: Evaluations of factors to derive the differential cross sections **88**
6.1 Outline 88
6.2 Total track length of the incident Σ^+ in the LH_2 target 88
6.3 Average efficiency of the $\Sigma^+ p$ scattering events including the detection and analysis efficiency 90
6.3.1 Detection efficiency of CATCH 90

6.3.2 Average efficiency for the Σ^+p scattering events considering the real detection efficiency 94

7 Experimental result and discussion **96**
7.1 Differential cross sections 96
7.2 Comparison with the past experiments and theoretical calculations 96
7.3 Phase-shift analysis 98
7.3.1 Specific expressions of differential cross section as a function of phase shifts 98
7.3.2 Consideration of the fixed phase shifts in the fitting 100
7.3.3 Fitting results and phase shifts of $^3S_1$ and $^1P_1$ states 101

8 Summary **104**

Acknowledgements **106**

A Tables of the differential cross sections **112**

B Derivation of the integrated cross sections for the Σ^+p elastic scattering with a fine momentum step **114**

Chapter 1

Introduction

1.1 Baryon-Baryon interaction and importance of ΣN interaction

The nuclear force, interaction between nucleons (NN interaction), plays a very important role in forming elements and nuclear matter like neutron stars as they exist now. Owing to a plenty of proton-proton and neutron-proton scattering experiments, the nuclear force is well described: The nuclear force is attractive in the middle to long ranges (>1 fm) and repulsive in the short range so called repulsive core. The behavior at the middle and long ranges is explained by meson exchange model. In contrast, the origin of the short-range repulsion is still unclear. In pioneering nuclear force research, the short-range repulsion was treated phenomenologically [1] or was attributed to the ω exchange in a boson-exchange picture [2]. The effect of antisymmetrization between quarks on short-range interactions was first considered using the quark cluster model (QCM) by Oka and Yazaki [3, 4]. They reported that the short-range repulsion could be explained by the Pauli principle between quarks (quark Pauli effect) and the color-magnetic interactions.

In order to understand the role of quarks in the nuclear force, it is important to extend the nuclear force to baryon-baryon interactions (BB interactions) adding another species of quarks. One of simple extended systems is the octet baryons composed of u, d, s quarks ($n, p, \Lambda, \Sigma^-, \Sigma^0, \Sigma^+, \Xi^-, \Xi^0$). The latter six baryons include at least one s quark and are called Hyperons (Y). Because the mass of s quark is relatively similar to ones of u, d quarks, the BB interactions can be approximately treated under the flavor SU(3) symmetry. The possibility of hyperon appearance in neutron stars (NSs) is discussed [5]. The BB interactions between the octet baryons are labeled by the multiplets as

$$8 \otimes 8 = 27 \oplus 8_s \oplus 1 \oplus 10^* \oplus 10 \oplus 8_a. \tag{1.1}$$

And the relationship between the isospin basis and the flavor SU(3) basis for the BB interaction channels with $S = 0$ and $S = -1$ are summarized in Table 1.1.

Although the 27-plet and the 10^*-plet can be examined from the NN interactions, the other four multiplets can be studied only from hyperon-nucleon (YN) and hyperon-hyperon (YY) interactions. They could be expected to have different features from the NN interaction in the short-range region, where interactions between quarks and gluons should be considered. For example, the 8_s-plet and the 10-plet are predicted to be a quite large repulsive force due to a Pauli forbidden state at a quark level. In contrast to them,

Table 1.1: Relationship between the isospin and flavor SU(3) bases for the BB interaction channels. Spin states S and a parity of the orbital angular momentum L are denoted as $^{2S+1}(-1)^L$, such as singlet-even (^{1}even) and triplet-odd (^{3}odd).

strangeness	BB channel (I)	^{1}even or ^{3}odd	^{3}even or ^{1}odd
0	$NN(I=0)$	–	$(\mathbf{10^*})$
	$NN(I=1)$	$(\mathbf{27})$	–
-1	$\Lambda N(I=\frac{1}{2})$	$\frac{1}{\sqrt{10}}[(\mathbf{8_s})+3(\mathbf{27})]$	$\frac{1}{\sqrt{2}}[-(\mathbf{8_a})+(\mathbf{10^*})]$
	$\Sigma N(I=\frac{1}{2})$	$\frac{1}{\sqrt{10}}[3(\mathbf{8_s})-(\mathbf{27})]$	$\frac{1}{\sqrt{2}}[(\mathbf{8_a})+(\mathbf{10^*})]$
	$\Sigma N(I=\frac{3}{2})$	$(\mathbf{27})$	$(\mathbf{10})$

the 8_a-plet and 1-plet are expected to have a weakly repulsive core and attractive pocket, respectively. These were firstly predicted by QCM [6] and recently reproduced by a lattice QCD simulations [7][8]. Therefore, revealing the natures of the flavor SU(3) multiplets is important for the systematic understanding of the BB interactions. In the ΣN channels, five SU(3) multiplets except for the 1-plet are included. Especially, the $\Sigma^+ p$ and $\Sigma^- n$ channel are the pure $I = 3/2$ and their triplet-even and singlet-odd states are suitable to investigate states the 10-plet, whose $^3S_1$ state is expected to have a large repulsive core originated from the quark Pauli effect.

1.1.1 Quark Pauli effect in the quark cluster model (QCM)

In the framework of QCM, the wave function for a baryon-baryon, (3q)-(3q) system, is expressed as

$$\Phi(1,2,\cdots,6) = \sum_\beta \mathcal{A}[\phi_A(1,2,3)\phi_B(4,5,6)\chi_\beta(\boldsymbol{R})], \tag{1.2}$$

where $\chi(\boldsymbol{R})$ is the relative wave function and $\mathcal{A}$ is the antisymmetrization operator for the six constituent quarks. A and B specify the baryon species and the β represents quantum numbers of the two-baryon channel. $\phi = \phi^{(\mathrm{orb})}\xi^{\mathrm{SF}}\xi^{\mathrm{C}}$ is the internal baryon wave function, composed of the orbital part, the isospin-coupled basis of the spin-flavor SU(6) wave functions, which incorporates the Pauli principle in the baryon level, and the color-singlet wave function. For $\phi_A^{\mathrm{orb}}(123)$, the product of three $(0s)$ wave functions in the harmonic oscillator potential is adopted. In the ground state of two-baryon relative motion, six constituent quarks are in the $(0s)$ state of the harmonic oscillator potential. Figure 1.1 shows the schematic drawings of the quark Pauli effect mechanism for the $^3S_1$ state in the $\Sigma^+ p$ system, where two u quarks have the same spin and color with a high probability. In this situation, at least one u quark must be excited to the higher orbit in order to satisfy the Pauli principle. Because quark-Pauli forbidden states with $(0s)^6$ configuration are vanished due to the antisymmetrization, the $\chi(\boldsymbol{R})$ components orthogonal to the ground state of the two-baryon relative motion increases depending on the appearance probability of the forbidden states. This makes a node of the relative wave function at short distance and the effective repulsive force.

Historically, the short range core of α-α system had been explained by similar mechanism [9] [10], so to speak, "nucleon Pauli effect" before the QCM for BB interaction was presented. The quark Pauli effect is analogous to that.

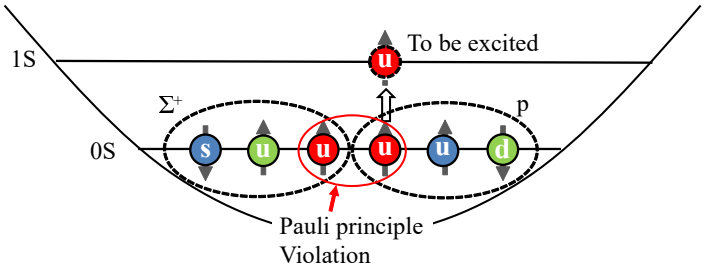

Figure 1.1: Rough sketch of the quark Pauli effect in the $\Sigma^+ p$ system. Two u quarks have the same spin and color with a high probability. In order to avoid violating Pauli principle, one u quarks should be excited, which result in the short range repulsive force.

1.2 Equation of state for neutron stars, hyperon puzzle, and three body force

The YN and YY interactions and potentials of hyperons in a nuclear matter, U_Y, are also important to discuss the structure of the neutron stars (NSs). Hyperons may appear in the inner core of NSs at densities of about 2-3ρ_0, where ρ_0 is the nuclear saturation density. In such a high density, the nucleon chemical potential is large enough to make the conversion of nucleons into hyperons energetically favourable. Not only the lightest hyperon, Λ, but also hyperons with negative charge, Σ^- and Ξ^-, are important because the onset of negative-charged hyperons permits the appearance of protons owing to charge neutrality. According to the relativistic mean-field models by J. Schaffner and I. N. Mishustin [11], the fraction of baryons and leptons in neutron star matter is calculated as shown in Figure 1.2. The Λ and Ξ^- present at 2.3 ρ_0 and 2.7 ρ_0, respectively. In contrast, Σ doesn't appear even at 10 ρ_0 because of its repulsive single-particle potential ($U_\Sigma = +30$ MeV). These conversion relieves the Fermi pressure exerted by the baryons and makes the Equation of state (EOS) softer. Consequently, the predicted maximum mass of NS becomes smaller than that without hyperon. Although this induction seems to be natural, the predicted maximum masses of NS with hyperons are incompatible with observations, such as the PSR J0740+6620 [12] which has the mass of $2.14^{+0.10}_{-0.09} M_\odot$. This problem is called "hyperon puzzle". To solve it, a mechanism is necessary that could provide the additional repulsion needed to make the EoS stiffer and therefore the maximum mass compatible with the current observational limits.

One of the possible mechanisms that could provide such an additional repulsion is the inclusion of repulsive hyperonic three-body forces. D. Lonardoni et al. calculated the EOS of NS with the auxiliary field diffusion Monte Carlo algorithm [13]. They indicated the importance of the three-body YN interaction for hardening the EOS. Two types of the ΛNN force were constructed in order to reproduce the hyperon separation energies of light or medium mass hypernuclei. Figure 1.3 shows the relation between the mass and radius of NS. The both types of three-body force make the EOS stiffer but the maximum masses strongly depend on the type of three-body force: 1.36 $M_\odot$ for type-(I) three-body force and 2.09 $M_\odot$ for type-(II) one, which has additional repulsive force from type-(I).

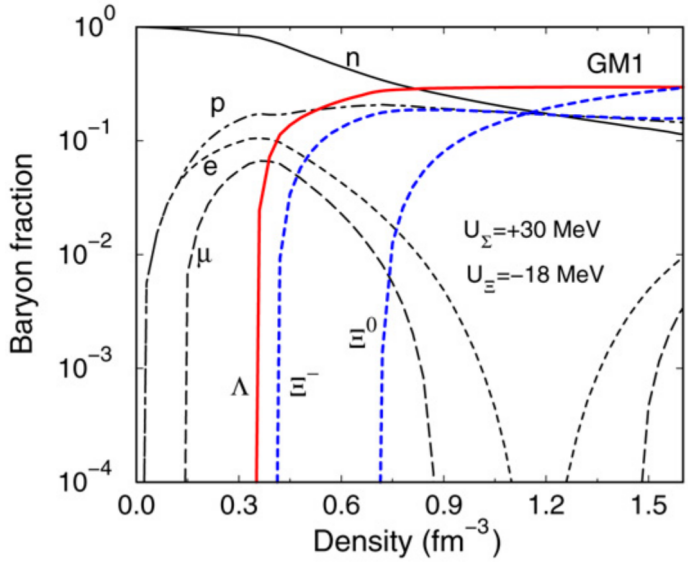

Figure 1.2: Calculated fraction of baryons and leptons in neutron star matter for a RMF calculation by J. Schaffner and I. N. Mishustin [11]

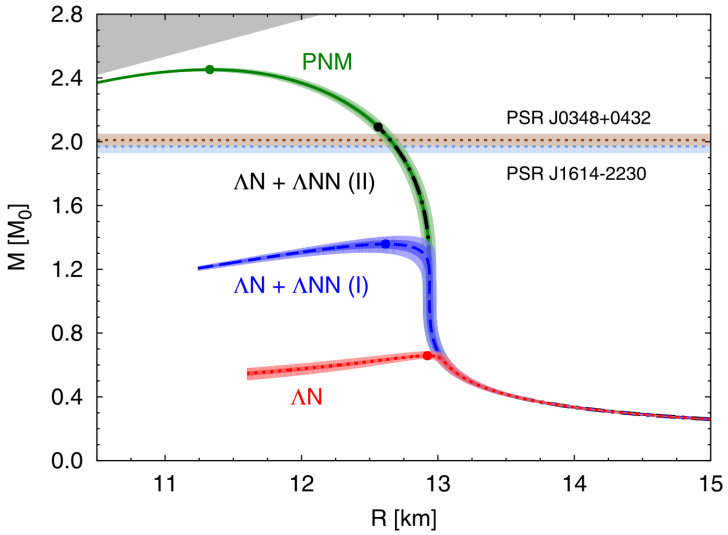

Figure 1.3: Mass-radius relations of NS for pure nucleon matter (PNM) and hyperon appearance cases [13].

In order to investigate a three-body force, both accurate understanding of the two-body force and the high-resolution experimental data of hypernuclei are needed. Establishing the experimental method for the YN scattering with a small error is quite important to get information on the former.

1.3 Theoretical Models for BB interaction

Many theoretical models have been constructed to describe the BB interactions. In this section, typical models are briefly introduced. In regard to the $\Sigma N(I = 3/2, {}^3S_1)$ interaction, a large repulsive force due to quark Pauli effect is expected to work. However, theoretical predictions for the strength of "large repulsive force" are different from each other.

1.3.1 Nijmegen Extended-soft-core Model (ESC)

The Nijmegen soft core models and extended-soft-core models, such as NSC97[14] and ESC08[15], are constructed based on the meson exchange picture between two baryons. For example, ESC08 consists of (i) One-boson-exchange, in which pseudo scaler mesons (π, η, η', K), vector mesons (ρ, ϕ, K^*, ω), scaler mesons ($a_0(962), f_0(993), \kappa(800), f_0(760)$), and axial-vector-mesons (a_1, b_1, f_1, K_1, f_1') are considered, (ii) two pseudo scalar mesons exchange and (iii) Meson-Pair-exchange. To explain the short range force, the ESC models additionally include (iv) multiple-gluon-exchange (Pomeron and Odderon exchange) and (v) structural effects due to the quark-core of the baryons, which is related to the quark-Pauli effect. In ESC models, the coupling constants of each particles, QCD cut-off masses are treated as parameters. These parameters are determined by fitting to abundant NN scattering data below $T_{\rm lab} = 350$ MeV and 52 YN scattering data with constraints from information derived from hypernuclei and hypernuclear matter.

1.3.2 Chiral Effective Field Theory (χEFT)

The χEFT models has successed for the derivation of the NN interaction. Applying the power counting to the effective potential, the calculations can be improved systematically by going to higher orders in a perturbative expansion. In higher order calculations, many body forces are also derived in a consistent way. For the NN interaction, χEFT has reached up to the fifth order (N^{4}LO) and the sixth order calculations have started [16]. For the YN interaction, This method is applied up to the second order (next-to-leading order, NLO [17][18]). The chiral YN potential consists of pseudo scalar meson (π, K, η) exchange and a series of contact interactions with an increasing number of derivatives, which corresponds to the order of momentum. The coupling constants and coefficients of contact interactions (low energy constants, LEC) are the parameters in χEFT frameworks. As a basis of LECs, one can select partial wave contributions for each of the flavor SU(3) multiplets. For example, six LECs are considered at the 0-th order (LO) ($C^{27}_{{}^1S_0}, C^{10*}_{{}^3S_1}, C^{8s}_{{}^1S_0}, C^{8a}_{{}^3S_1}, C^{10}_{{}^3S_1}, C^{1}_{{}^1S_0}$). For the NLO calculation, additional three and thirteen LECs for the contributions of $S-D$ transition and P waves are needed. These LECs are determined by fitting to experimental data. Based on available NN scattering data and low energy YN scattering data, LECs for all S wave contributions and higher-partial wave contributions of only 27-plet and 10*-plet are determined.

1.3.3 BB interaction including QCM

FSS and fss2 [19] use QCM for describing the short-range interaction and an effective meson exchange potential for the middle and long range interactions. In these models,

the quantum mechanical Hamiltonian of BB interaction is defined as a Hamiltonian for 6-body mechanics as

$$H = \sum_{i=1}^{6}\Big(m_i c^2 + \frac{p_i^2}{2m_i} - T_G\Big) + \sum_{i<j}^{6}\Big(U_{ij}^{\rm Cf} + U_{ij}^{\rm FB} + \sum_{\beta} U_{ij}^{{\rm S}\beta} + \sum_{\beta} U_{ij}^{{\rm PS}\beta} + \sum_{\beta} U_{ij}^{{\rm V}\beta}\Big), \quad (1.3)$$

where $U_{ij}^{\rm CF}$ is the confinement potential of quarks , $U_{ij}^{\rm FB}$ is the Fermi-Breit interaction related to quark-quark interaction and $U_{ij}^{\rm S}, U_{ij}^{\rm PS}, U_{ij}^{\rm V}$ are effective-meson exchange potentials, in which the flavor singlet and octet mesons are considered. The Quark cluster models has four parameters: size parameter b defining the internal harmonic oscillator potential for quarks, the up-down quark mass m_{ud}, the strength of the quark-gluon coupling constant α_S and the mass ratio of the strange to up-down quarks $\lambda = m_s/m_{ud}$. For the meson exchange part, the quark-meson coupling constants of the singlet and octet meson and singlet-octet mixing angle for each of the scaler, pseudo scaler and vector mesons are parameters. Mass of scaler mesons are also parameters within some appropriate ranges. These parameters are determined by fitting to NN scattering data ($J \leq 2, T_{\rm lab} = 350$ MeV) and low-energy YN total cross sections.

1.3.4 Lattice QCD

Recently, a numerical QCD simulation called Lattice QCD was successfully carried out for the BB interactions owing to developments of calculation techniques and great progress of computer performance. HAL QCD collaborations performed a large scale lattice QCD calculation with the almost physical quark masses corresponding to $(m_\pi, m_K) = (146, 525)$ MeV and large volume $(La)^4 = (8.1{\rm fm})^4$. Figure 1.4 shows the six calculated potentials for baryon-baryon S wave interactions by a lattice QCD simulation. The strong repulsive forces in 8s-plet and 10-plet and the attractive core in 1-plet are reproduced. These features indicates the importance of the quark Pauli effect for the short-range baryon-baryon interaction.

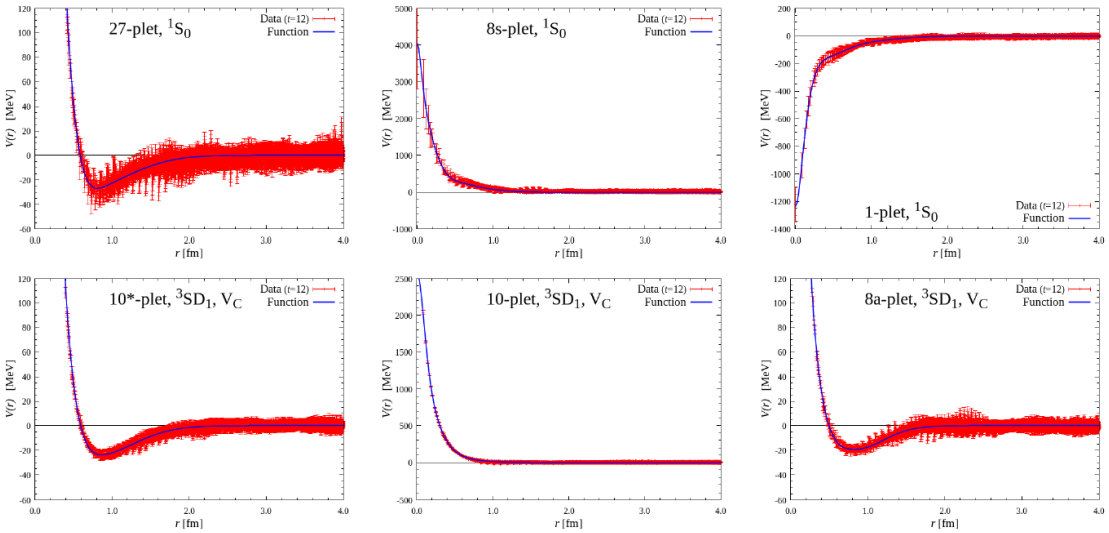

Figure 1.4: Calculated potentials for baryon-baryon S wave interactions by the HAL-QCD collaboration [20]. These are obtained from hyperon interaction potentials in the baryon-basis in strangeness $S = -2$ sector by rotation assuming the exact flavor $SU(3)$ symmetry.

Although calculations for potentials of higher partial waves need huge computational resources, they are expected to be realized with the supercomputer Fugaku.

1.3.5 Theoretical predictions for $\Sigma N(I = 3/2,^3 S_1)$ interaction

Theoretical treatments of the short-range interaction in the BB interactions had led to considerably different results on the ΣN ($I = 3/2$, $^3S_1$) interaction. The momentum dependence of the calculated phase shift of $^3S_1$ state is shown in Figure 1.5. fss2, which

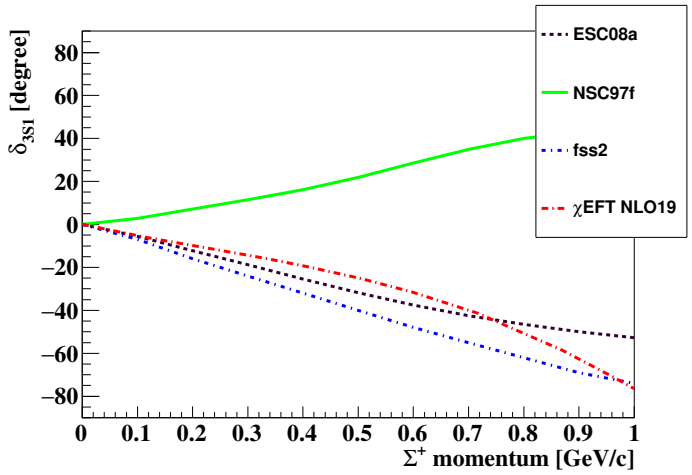

Figure 1.5: Calculated phase shifts of $^3S_1$ state for the Σ^+p scattering as a function of the incident Σ^+ momentum.

includes QCM in the short-range region, naturally predicts a considerably repulsive interaction [19]. However, the pure meson-exchange models, such as the NSC models [21, 14], which represent the short-range interaction from a heavy vector-meson exchange, predicted attractive interaction. In the Nijmegen ESC model, the additional short-range interaction owing to Pomeron exchange is newly included to explain the repulsive nature of this channel [15, 22]. Recent calculations by χEFT predict repulsive interaction for this channel [17, 18]. By the recent lattice QCD simulation in the almost physical quark masses, the ΣN ($I = 3/2$, $^3S_1$) potential was demonstrated a repulsive core in the short-range region without any attractive pocket in the middle-range region as shown the "10-plet" in Figure 1.4.

In summary, all of recent theoretical calculations predict repulsive interactions in the ΣN ($I = 3/2$, $^3S_1$) channel. However, the strength of the repulsive interaction, i.e., the phase shift value of the $^3S_1$ channel, is quite different from each other and it should be determined from experiments.

1.4 Previous experimental studies on ΣN and Σ-nucleus interaction

1.4.1 $\Sigma^{\pm}p$ scattering experiment

A YN scattering experiment is the most direct method to derive the YN interaction as in the case of the NN interaction. However, the YN scattering experiment is quite difficult due to the short lifetime of hyperons and data are quite scarce.

For a low momentum region of around 0.15 GeV/c, where the S wave is dominant, the $\Sigma^{\pm}p$ scattering cross section was measured with a few tens percent error using a bubble chamber [23].

Data for higher momentum range more than 0.4 GeV/c is desired in order to investigate short-range interactions and higher wave contributions. Accumulating enough scattering events is generally more difficult for the higher momentum because the cross section decreases proportionately to $1/k^2 = (\hbar/p_{\mathrm{CM}})^2$. In past KEK E251 [24] and E289 [25] [26] experiments, a scintillation fiber (SCIFI) active target, which is a triggerable imaging detector, was used in order to recognize the $\Sigma^{\pm}p$ scattering events and they were accumulated efficiently. Nevertheless, statistics of the $\Sigma^{\pm}p$ scatterings for 0.3-0.75 [GeV/c] region were limited to less than 100 events and the errors of the differential cross sections were more than 50%, which were too large to restrict BB interaction models well. Although there is one spin-observable measurement on the $\Sigma^{+}p$ channel in the KEK E452 experiment [27], no phase shift value has been obtained experimentally.

1.4.2 Σ hypernuclei and quasi-free Σ production

Since YN scattering measurements are difficult, information on the YN interactions have been studied through hypernuclear data. Especially, this method has been succeeded for the ΛN hypernuclei. For the ΣN interaction, there are important results for light Σ hypernuclei and medium-to-heavy Σ hypernuclei. The former is for the $A = 4$ hypernnuclei. T. Nagae et al.[28] revealed that a clear peak below the Σ^+ production threshold could be observed in the ^{4}He(K^-, π^-) reaction at 600 MeV/c, whereas in ^{4}He(K^-, π^+) reaction

no such peak was found as shown in Figure 1.6. This result meant only the $T = 1/2$ state was bound state because it can be produced only by the ^{4}He(K^-, π^-) reaction. It was caused by the large isospin dependence in the ΣN interaction: $T = 1/2$ state is attractive and $T = 3/2$ state is strongly repulsive. Only $^4_\Sigma$He state is observed as a bound Σ hypernuclear state.

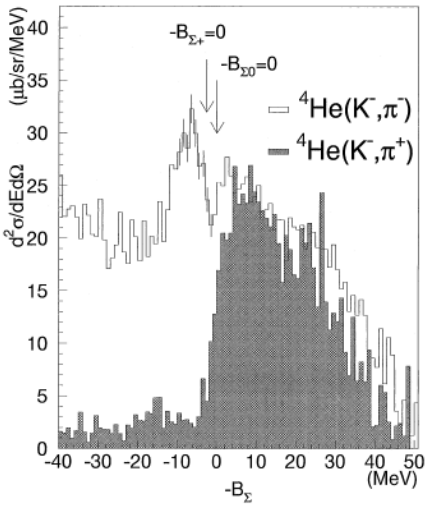

Figure 1.6: Excitation energy spectra of ^{4}He(K^-, π^-) and ^{4}He(K^-, π^+) at 600 MeV/c K^- momentum measured at 4° in the BNL E905 experiment[28].

While medium-to-heavy Σ hypernuclei bound states have not been observed, Σ-nucleus potential was investigated by analyzing the spectrum of the (π^-, K^+) reaction on the various nuclear targets in KEK E438 experiment [29][30]. The missing mass spectrum of the ^{28}Si(π^-, K^+) reaction at the beam momentum of 1.2 GeV/c is shown in Figure 1.7. In the analysis, the spin-isospin averaged potential was assumed to be Woods-Saxon (WS) type potential as

$$U^\Sigma = \frac{V_0^\Sigma + iW_0^\Sigma}{1 + \exp\left(\frac{r-R}{a}\right)} \tag{1.4}$$

where V_0^Σ and W_0^Σ are the strength of the real and imaginary parts of the potential. The best V_0^Σ and W_0^Σ were evaluated to be $(V_0^\Sigma, W_0^\Sigma) = (30\text{MeV}, -40\text{MeV})$ by T. Harada and Y. Hirabayashi [31]. This result indicates that the single particle potential of a Σ particle in nuclei is repulsive.

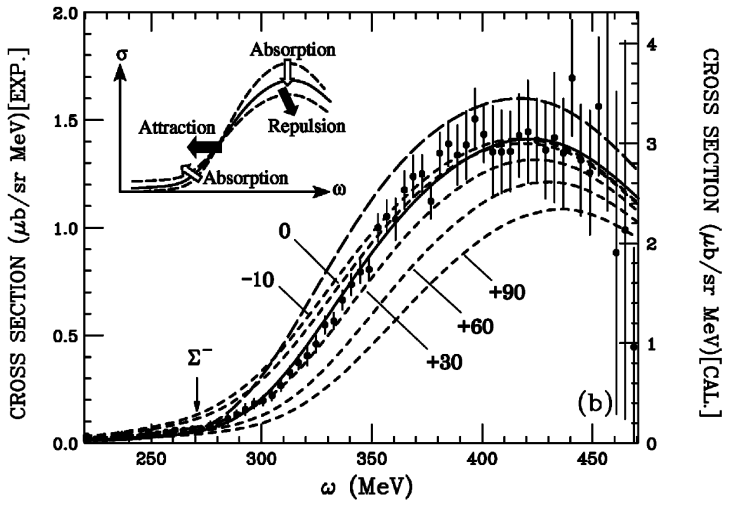

Figure 1.7: Missing mass spectrum of the ^{28}Si(π^-, K^+) reaction at the beam momentum of 1.2 GeV/c [29][30]. The DWIA calculation results with several parameters of Σ-nucleous potential [31] were overlaid as lines.

1.4.3 Σ^- atom

When a hadron with a negative charge is captured in an atomic orbit around a nucleus, the hadron and nucleus can overlap because its orbital radii is much shorter than the ordinary atomic states. Such exotic atoms are a probe to the strong interaction between the hadron and nuclei at the surface of nuclei. The X-ray energy shift from the electromagnetic interaction gives information on the real part of the optical potential and the X-ray width is relevant to the imaginary part. The Σ^- atom data had been taken for the 11 kinds of nuclei (O, Mg, Al, Si, S [32], C, Ca, Ti, Ba [33], W and Pb [34]). The latest analysis [31] confirmed that the Σ-nucleus potential having a repulsion inside the nuclear surface and an attraction outside the nucleus with a sizable absorption, which is similar to the potential mentioned in the previous subsection, can explain simultaneously the data of the Σ^- atoms and ^{28}Si(π^-, K^+) reaction.

1.4.4 Femtoscopy technique

Recently, the study of two-particle correlations in momentum space measured in ultra-relativistic p-p and p-Pb collisions at the LHC has provided access to the interaction between particle pairs in vacuum. In this process, all hadrons originate from very small space-time volumes and typical distances between two particles are about 1 fm. From the uncertainty principle, the interaction between baryon pairs can be investigated for relative momentum up to 200 MeV/c. With this method, many channels of the BB interactions are investigated, such as the $pp, p\Lambda, \Lambda\Lambda$ [35], and $p\Xi^-$ [36] interactions. For the ΣN interactions, ALICE collaboration applied this technique to the $p\Sigma^0$ channel [37], in which the $\Sigma^0 \to \Lambda\gamma$ decay can be reconstructed relatively easily by the ALICE detectors. At present, the experimental precision is not enough to select the best theoretical model. With the expected larger data samples to be obtained in LHC Run3 and Run4, low-momentum ΣN interactions will be constrained from femtoscopic measurements in future.

1.5 Present experiment: J-PARC E40 experiment

The J-PARC E40 experiment [38] was proposed to confirm predicted strong repulsive force in the Σ^+p channel, which is related to the quark Pauli effect, and to study the ΣN interaction systematically. The purpose of this experiment is to measure the differential cross sections of Σ^+p elastic, Σ^-p elastic, and $\Sigma^-p \to \Lambda n$ inelastic scattering with high statistics. Momentum range of the incident $\Sigma^\pm$ were from 0.45-0.85 GeV/c, where typical distances between two particles in the $\Sigma^\pm$ scatterings are 0.8-0.5 fm and they would overlap each other. Since the large uncertainties of cross sections in previous experiments were predominantly caused by the lack of statistics, high-statistics scattering experiment is essential to improve the data quality. More reliable data enables comparison with theoretical calculations. For example, the differences of phase shifts shown in Figure 1.5 result in the difference of differential cross sections by approximately 30 %. In order to distinguish which theoretical calculation agrees with data, more precise data is needed. High-statistics data further enables us to obtain the precise angular dependence of the differential cross sections. It reflects the contributions of higher partial waves, for which there are few reliable experimental data. Moreover, exploiting high-quality differential cross section data and the simple representation of Σ^+p interaction in the SU(3) flavor symmetry, a phase shift analysis on Σ^+p scattering were realized as later explained in Chapter 7.

This experiment was performed at K1.8 beamline in the J-PARC hadron experimental facility in the separated periods of June 2018, February-March 2019 (for Σ^-p scattering data taking), April 2019 and May-June 2020 (for Σ^+p scattering data taking).

To achieve the high-statistic $\Sigma^\pm p$ scattering experiment, production of many incident Σ^+ particles are essential. In order to produce many incident Σ^+ particles via the $\pi^\pm p \to K^+\Sigma^\pm$ reaction, a high intensity π^+ beam of approximately 1.0×10^7 Hz and large acceptance spectrometer for the outgoing K^+ were used. Additionally, so-called CATCH system [39] surrounding the target was developed, which has enough rate tolerance against the high intensity beam condition and a large acceptance for recoil protons from Σ^+p scattering ($-1 < \cos\theta_{\rm CM} < 0.5$). Owing to these experimental features, a high-statistical hyperon-proton scattering experiment was realized.

Results on the Σ^-p elastic scattering [40] and $\Sigma^-p \to \Lambda n$ inelastic scattering [41] have already been reported. Regarding the statistics, approximately 4500 Σ^-p elastic and 2300 $\Sigma^-p \to \Lambda n$ inelastic scattering events were identified. The derived differential cross sections for Σ^-p elastic and $\Sigma^-p \to \Lambda n$ inelastic scatterings are shown in Figure 1.8 and Figure 1.9, respectively. The statistical error of the 10% level was achieved even with a fine angular step of $d\cos\theta = 0.1$ and the data compared to predictions of theoretical models. These data will be reliable input to determine the 8_s-plet and 8_a-plet interactions, as shown in Table 1.1.

In this thesis, whole of the Σ^+p scattering experiment as an important part of J-PARC E40 experiment is described.

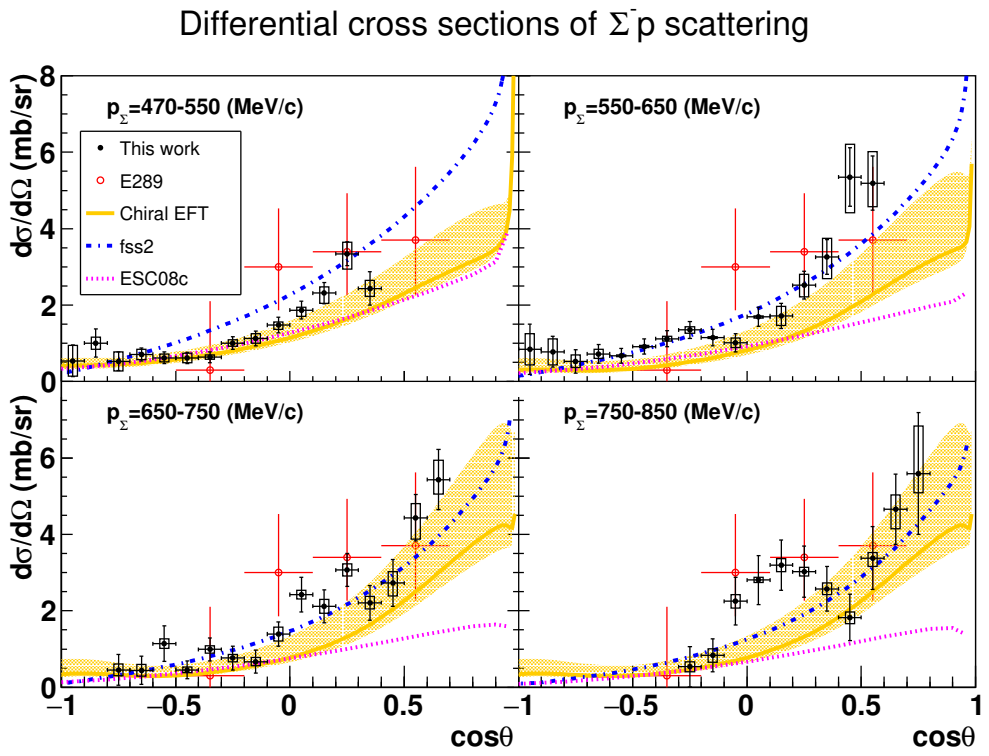

Figure 1.8: Differential cross sections for the $\Sigma^- p$ elastic scattering obtained from the J-PARC E40 experiment [40]. The black point represents the J-PARC E40 result.

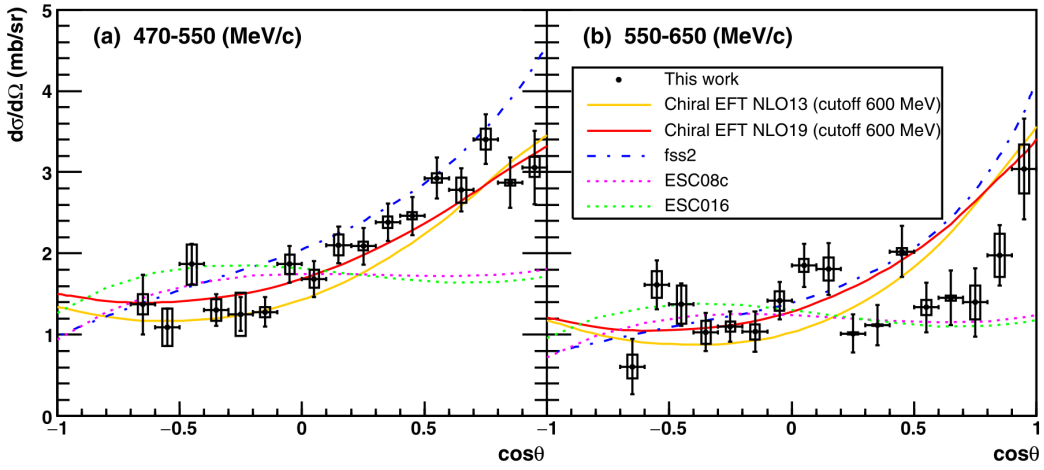

Figure 1.9: Differential cross sections for the $\Sigma^- p \to \Lambda$ elastic scattering obtained from the J-PARC E40 experiment [41]. The black point represents the J-PARC E40 result.

1.6 Thesis composition

The setup of present experiment is described in Chapter 2. The whole analysis flow to derive the differential cross sections for the $\Sigma^+ p$ scatterings is briefly summarized in

Chapter 3. The analysis was divided into three stages, the analysis of spectrometers and CATCH, identification of the $\Sigma^+ p$ scattering events, and evaluation of factors to derive the differential cross sections. These are described in Chapter 4, 5, and 6, respectively. The obtained results are presented and $\Sigma N(I = 3/2)$ interaction are discussed in Chapter 7. Finally, the $\Sigma^+ p$ scattering experiment is summarized in Chapter 8.

Chapter 2

Experiment

2.1 Outline

The Σ^+p scattering data taking as a part of the J-PARC E40 experiment was performed at the K1.8 beam line in the J-PARC Hadron Experimental Facility with π^+ beams of 1.41 GeV/c. Typical intensity of the π^+ beam was 2.0×10^7 particles per spill of 2.0 s duration every 5.2 s.

A conceptual drawing of the experiment is shown in Figure 2.1. A liquid hydrogen target (LH_2 target) is used both for the incident Σ^+ production and Σ^+p scattering. Σ^+p scattering events can be identified by measuring the Σ^+ momentum, the recoil proton's kinetic energy and the proton's recoil angle. Σ^+ particles are produced via the $\pi^+p \to K^+\Sigma^+$ reaction induced by π^+ beam. The momentum of each Σ^+ can be calculated as the missing momentum of the π^+ beam and outgoing K^+, analyzed using two magnetic spectrometers. The produced Σ^+ particles can induce additional reactions, such as the desired Σ^+p scattering. Using the detector system surrounding the LH_2 target, charged particles involved in these reactions and decay products of Σ^+ are measured. In order to produce many incident Σ^+ particles, a high intensity π^+ beam and large acceptance spectrometer for the outgoing K^+ were used. The surrounding detector system, so-called CATCH system [39] comprises a fiber tracker and calorimeter, which has enough rate tolerance against the high intensity beam condition and a large acceptance for recoil protons from Σ^+p scattering. Owing to these experimental features, a high-statistical hyperon-proton scattering experiment was realized.

2.2 J-PARC and Hadron Experimental Facility

The Japan Proton Accelerator Research Complex (J-PARC) is a multi-purpose accelerator facility located in Tokai village, Japan [42, 43]. Experiments related to not only the basic science of particle and nuclear physics but also the materials and life sciences are performed, using various types of secondary beams of neutrinos, muons, pions, kaons, protons, neutrons, and so on. An aerial photograph of J-PARC is shown in Figure 2.2. J-PARC comprises three proton accelerators, a 400 MeV linac, a 3 GeV rapid cycling synchrotron (RCS), and a 30 GeV main ring synchrotron (MR) and three experimental facilities, the Neutrino Experimental Facility (NU), the Hadron Experimental Facility (HEF), and the Material and Life Science Facility (MLF).

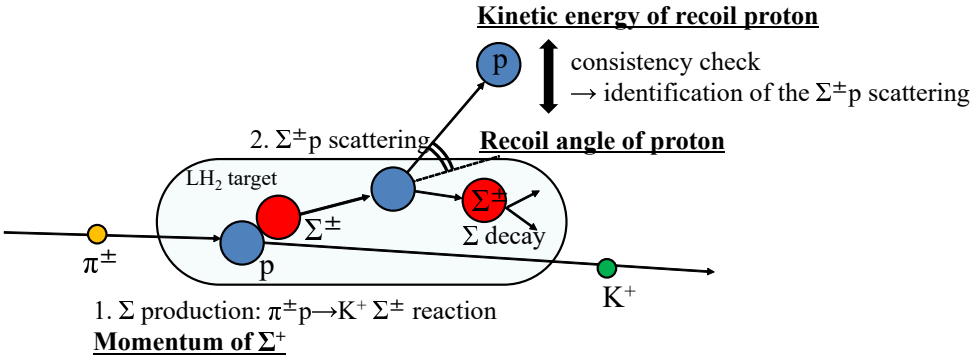

Figure 2.1: Conceptual drawing of the $\Sigma^+ p$ elastic scattering in the J-PARC E40 experiment. The initial Σ^+ is produced by the $\pi^+ p \to K^+\Sigma^+$ reaction. Then, it travels in the LH_2 target and may cause $\Sigma^+ p$ scattering. The $\Sigma^+ p$ elastic scattering can be kinematically identified by measuring the initial Σ^+'s momentum, the recoil proton's kinetic energy, and recoil angle.

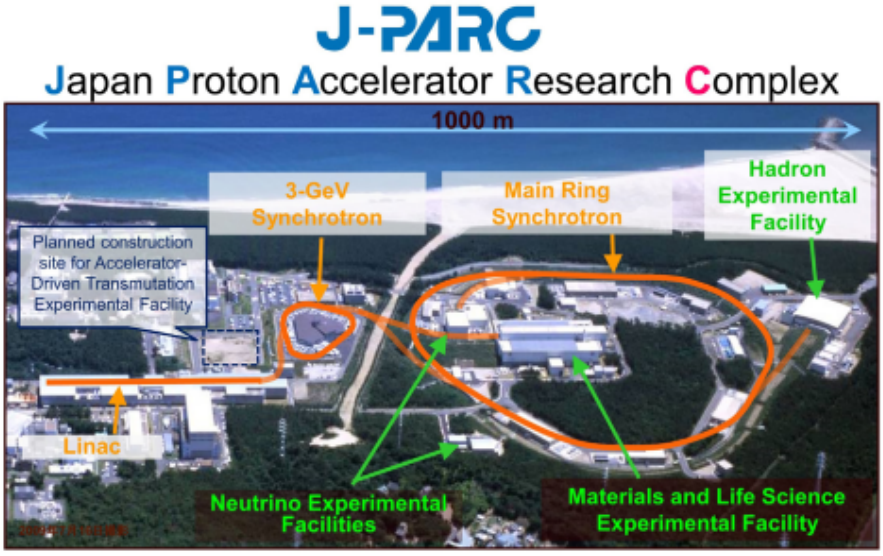

Figure 2.2: Aerial photograph of J-PARC [44]. Three accelerators, linac, RCS, and MR and three experimental facilities, NU, HEF, and MLF are shown. The construction of an accelerator-driven transmutation facility is planned.

At the linac, negative hydrogen ions (H^-) are accelerated up to 400 MeV and they are finally converted to protons with a charge-stripper foil and injected to RCS. RCS has circumferences of 348.3 m and accelerates the injected protons up to 3 GeV at a repetition rate of 25 Hz. Most of the RCS beam pulses are delivered to MLF and the rest of the pulses are injected to MR. In MLF, muon and neutron beams, which are produced by colliding 3 GeV protons with carbon and mercury targets, are available. The protons injected from RCS to MR are accelerated up to 30 GeV and delivered to NU or HEF with different extraction modes, fast extraction and slow extraction, respectively. In the fast

extraction mode, where all beam bunches are extracted to NU within a one-turn time period of approximately 5 μs. Then neutrino and anti-neutrino beams are generated as a decay products of $\pi^{\pm}$, which are produced by colliding the extracted proton beam with graphite target. They are used for the Tokai to Kamioka long-baseline neutrino oscillation experiment, T2K. While in the slow extraction mode, the beam are gradually extracted to HEF over 2s using the resonant extraction method . Beams extracted in one cycle or one-cycle extraction itself are called spill. The spill cycle were 5.2 s, of which 2 seconds were on-beam.

The layout of HEF is shown in Figure 2.3. The extracted proton beam is bombarded to the production target, T1 and secondary particles, such as $p, \pi^{\pm}, K^{\pm}, K_0^L$ were produced. The secondary particles are delivered to experimental areas through the secondary beam lines, K1.8, K1.8 BR, KL and K1.1. In the data-taking period for present experiment, the production target was a golden bar with a size of 15mm (W) $\times$ 6mm (H) $\times$ 66 mm (T). Recently, new beam lines, high-p and COMET, were constructed, where primary proton beams are available.

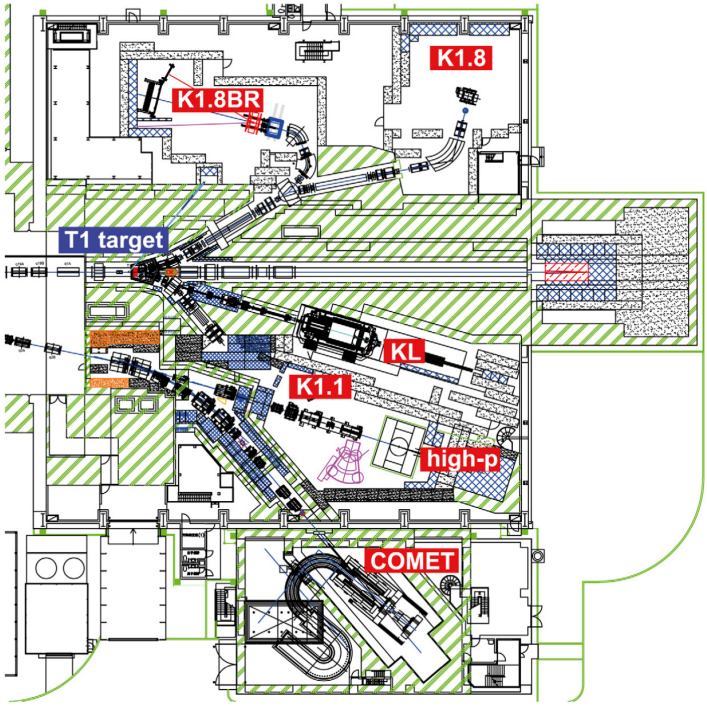

Figure 2.3: Layout of the hadron experimental facility[44]. K1.8, K1.8 BR, KL, and K1.1 are secondary beam lines. In high-p and COMET beam lines, primary proton beam is available for experiments.

2.3 K1.8 beam line

The K1.8 beam line [45] is a multi-purpose beam line, where varyous secondary hadron beams up to 2.0 GeV/c, such as $K^{\pm}, \pi^{\pm}, p$ and $\bar{p}$ are available. In the present experiment, we used the π^{+} beam at 1.41 GeV/c with a beam intensity of 2×10^7 particles per spill. Additionally, proton beams with various momenta between 0.45 and 0.85 GeV/c were

used in order to collect pp scattering data for calibration. Figure 2.4 shows the schematic drawing of the K1.8 beam line. This beam line comprises three sections, the upstream section, mass separation section, and momentum analysis section.

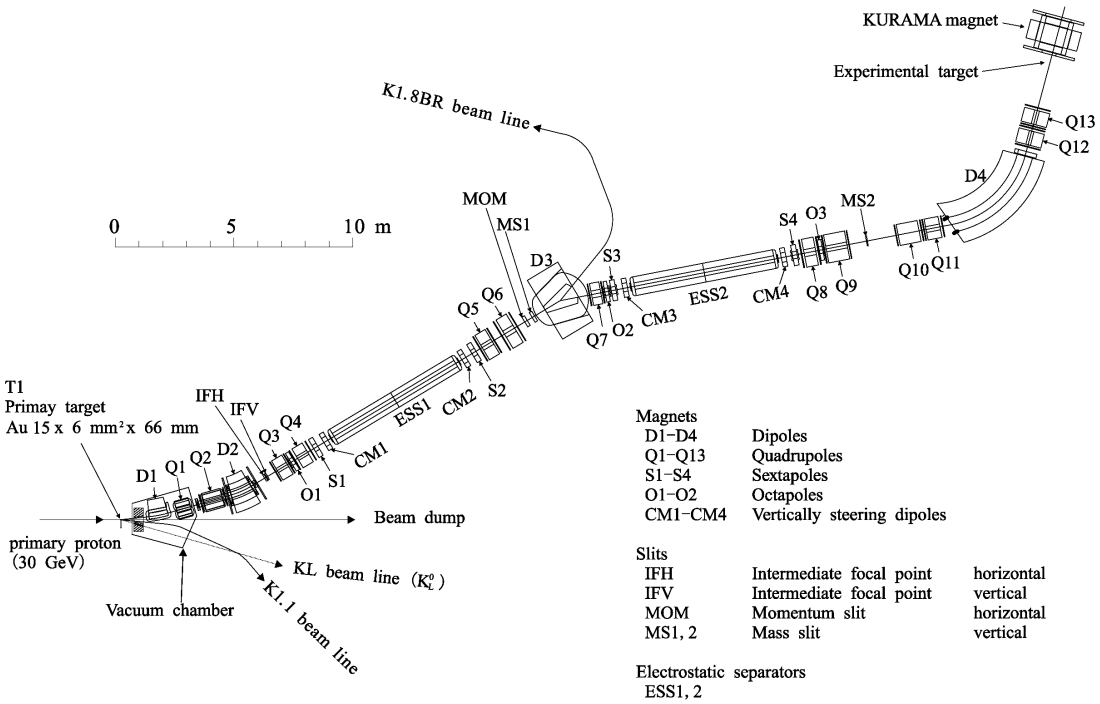

Figure 2.4: Schematic drawing of the K1.8 beam line.

Upstream section

The upstream section is from D1 to IFV in Figure 2.4. Two dipole magnets (D1 and D2) and two quadruple magnets (Q1 and Q2) are equipped. The momentum of the extracted secondary beam particle is determined by the D1 magnet setting and the transported beam is vertically focused at the intermediate focus (IF) point. At the IF point, a horizontal slit (IFH) and a vertical slit (IFV), which are made of a 30-cm thick brass block, are equipped and they shapes beam profiles. Using IFH and IFV, the so-called cloud pions, which are produced by the decay of K_s^0, and the scattered pions from materials in the upstream section are rejected.

Mass separation section

The mass separation section is from Q3 to MS2 in Figure 2.4. This section consists of two-stage mass separation systems, the first stage mass separation system (Q3 to D3) and second stage mass separation system (Q7 to MS2). Electrostatic separators (ESS1 and ESS2) are the key components of this section, which generate transverse electric field along the beam axis to separate particles of the same momentum by their mass differences. Each electrostatic separator generates an electric field with a gap of 10 cm between parallel electrode plates with a size of 30 cm in width and 6 m in length. The cathode and anode plates are made of anodized aluminum and stainless steel, respectively.

In the present experiment, the gradient of the electric fields was set to 30 kV/cm for π^+ beam. For proton beam, only ESS1 was used and the gradient was set to 10 kV/cm.

The displacement of particle orbits due to ESS is corrected using correction magnets (CM1-CM4) equipped at the entrance and exit of the electrostatic separators. After ESS1 and ESS2, the beam is focused in the vertical direction at each mass slit (MS1 and MS2) and momentum dispersion become large horizontally. The mass of beam particles can be selected by tuning the magnetic fields of correction magnets and mass slit positions. For the present pion beam experiment, the settings of them were adjusted to let only pions pass through the slit. A horizontal momentum slit (MOM) determines the momentum bite of the secondary particles.

Momentum analysis section

The momentum analysis section called K1.8 beam-line spectrometer is placed at the end of K1.8 beam line, which is also the entrance of K1.8 experimental area. The section comprises five magnets in a QQDQQ configuration and counters and position detectors. The details of this section are described in the next section.

2.4 K1.8 beam-line spectrometer

Figure 2.5 shows the schematic drawing of the K1.8 beam-line spectrometer. The five analyzer magnets in a QQDQQ configuration form the K1.8 beam-line spectrometer together with detectors upstream and downstream of the magnets. A plastic scintillator hodoscope (BH1) and plastic scintillator fiber detector (BFT) were placed upstream of the magnets. In contrast, the drift chambers (BC3 and BC4) and another plastic scintillator hodoscope (BH2) were placed downstream of these magnets. The π^+ beam was focused on the center of the LH_2 target and its momentum was reconstructed event-by-event using the spatial information at BFT, BC3, and BC4, and the third-order transfer matrix for the spectrometer. Figure 2.6 shows the distribution of the beam π^+ particles at the center of the target.

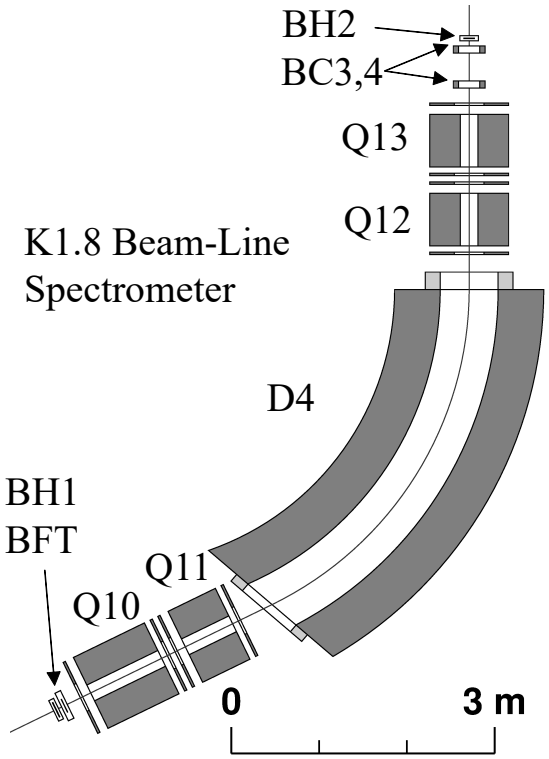

Figure 2.5: Schematic drawing of the K1.8 beam-line spectrometer. The K1.8 beam-line spectrometer comprises five analyzer magnets in a QQDQQ configuration (D4 and Q10-Q13), two hodoscopes (BH1 and BH2), and three tracking detectors (BFT, BC3, and BC4).

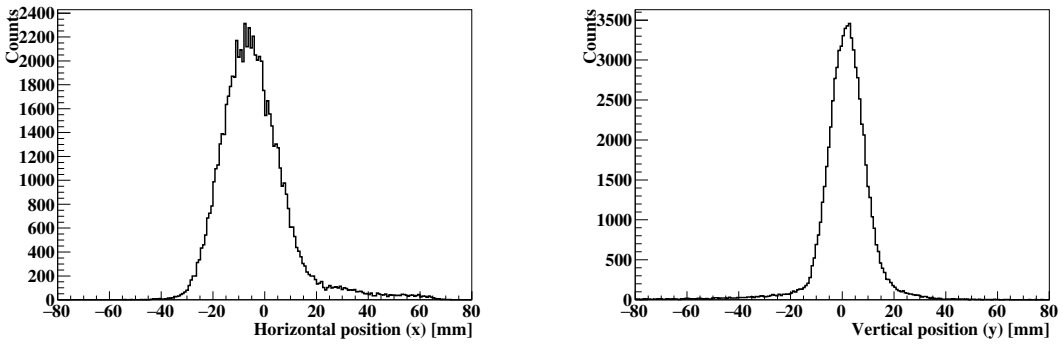

Figure 2.6: (Left) Horizontal and (Right) vertical distributions of the beam π^+ particles at the center of the target.

The effective areas and position resolutions of the detectors are summarized in Table 2.1. More detailed information on detectors is described in the following subsections. The design value of the momentum resolution is $\Delta p/p = 3.3 \times 10^{-4}$ (FWHM) with a position resolution of 200 μm [46]. The central momentum is determined by the magnetic field of the dipole magnet (D4). Using a high precision Hall probe [Digital Teslameter 151

(DTM-151)] installed in the D4 magnet, the magnetic field was monitored. The typical magnetic field for 1.41 GeV/c π^+ beam was 1.1738 T and observed deviation was less than 0.03 %.

Table 2.1: Effective areas and position resolutions of detectors in the K1.8 beam-line spectrometer.

Detector	type	role	effective area H × V [mm^2]	$\sigma_{\rm pos}$ [mm]
BH1	plastic scintillator hodoscope	(BFT hits selection)	170 × 66	–
BFT	plastic scintillator fiber detector	tracker	160 × 80	0.19
BC3,4	drift chambers	tracker	200 × 100	0.20
BH2	plastic scintillator hodoscope	trigger	118 × 60	–

2.4.1 Hodoscopes in the K1.8 beam-line spectrometer

The beam hodoscopes, BH1 and BH2, are usually used for beam particle identification by measuring a time-of-flight for 10.4 m distance. However, in the present experiment, the contaminations of other particle species in the π^+ beam were negligibly small. Thus, BH1 was primarily used for selecting the BFT hits corresponding to the triggered event in multiple-beam events. BH2 was used as the most important trigger counter determining the origin of timing for all detectors.

BH1

BH1 was located upstream of the analyzer magnets. It comprises eleven segments of plastic scintillators (Saint-Goban BC-420) with different width of 8, 12, 16, and 20mm as shown in the left side of Figure 2.7. The width of each segment is adjusted for the single counting rate to be uniform. The total effective area is 170mm (H) × 66mm (V). Scintillation signals are read using PMTs (Hamamatsu H6524MOD) on the top and bottom of scintillator through acrylic light-guides. In order to stand a high-rate beam condition, a three-stage booster was equipped by PMTs.

BH2

BH2 was located most downstream of the K1.8 beam-line spectrometer. As BH1, it comprises eight segments of plastic scintillator (Saint-Goban BC-420) with different width of 7, 10, 35mm as shown in the right side of Figure 2.7. The total effective area is 118 mm (H) × 60 mm (V). Signals are read from both vertical ends using PMTs (HPK R9880U-110MOD) equipping a three-stage booster.

2.4.2 Trackers in the K1.8 beam-line spectrometer

In order to reconstruct the momentum of beam particle using the third-order transfer matrix, an one-dimensional hit position at the entrance of the magnets and position and angle at the exit of the magnets were measured.

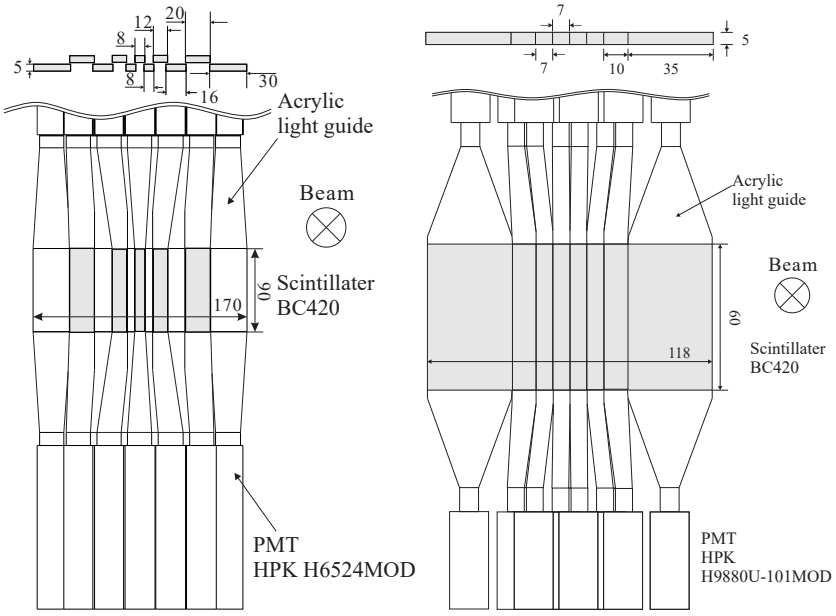

Figure 2.7: Schematic drawings of BH1 (Left) and BH2 (Right).

BFT

BFT was located between BH1 and Q10 to measure the horizontal position of the beam. BFT has a two-layers configuration (XX') made of 320 scintillation fibers (Kuraray SCSF-78MJ) with a diameter of 1mm. Scintillation signals are read by a MPPC (Hamamatsu S10362-11-100P) attached at the end of each fiber. The effective area is 160 mm (H) $\times$ 80mm (V) and the position resolution was estimated to be 190 μm in σ. The pictures of BFT and the MPPC card are shown in Figure 2.8.

BC3 and BC4

Two MWDC were located at the exit of the analyzer magnets to measure the beam trajectory, which means position and angles. Both chambers have a six layers configuration ($xx'uu'vv'$) with 3-mm wire spacing. u and v planes are tilted by $\pm 15^\circ$, respectively. The sense wire is gold-plated tungsten wire with 12.5 μm-diameter and the potential wire is a gold-plated copper beryllium wire with 75 μm-diameter. A set of two layers such as xx', uu', vv' is called as a pair plane. In the pair plane, wire positions are shifted by a half cell size of 1.5mm. Owing to this structure, the left/right ambiguity of each hit can be solved. In the operation, a mixed gas of Ar(76%), iso-C_4H_{10} (20%), and methylal(4%) was filled in BC3 and BC4. Methylal prevents anode wires from sputtering due to beam particles. A raw signal from each wire was read by Amplifier Shaper Discriminator (ASD) card attached on the chamber. A high voltage of -1.19 kV for sense wires and -1.21kV for potential wires were applied.

2.5 KURAMA spectrometer

Outgoing charged particles produced at the LH_2 target by the $\pi^+ p$ reaction were analyzed by the KURAMA spectrometer. Figure 2.9 shows the schematic drawing of the KURAMA

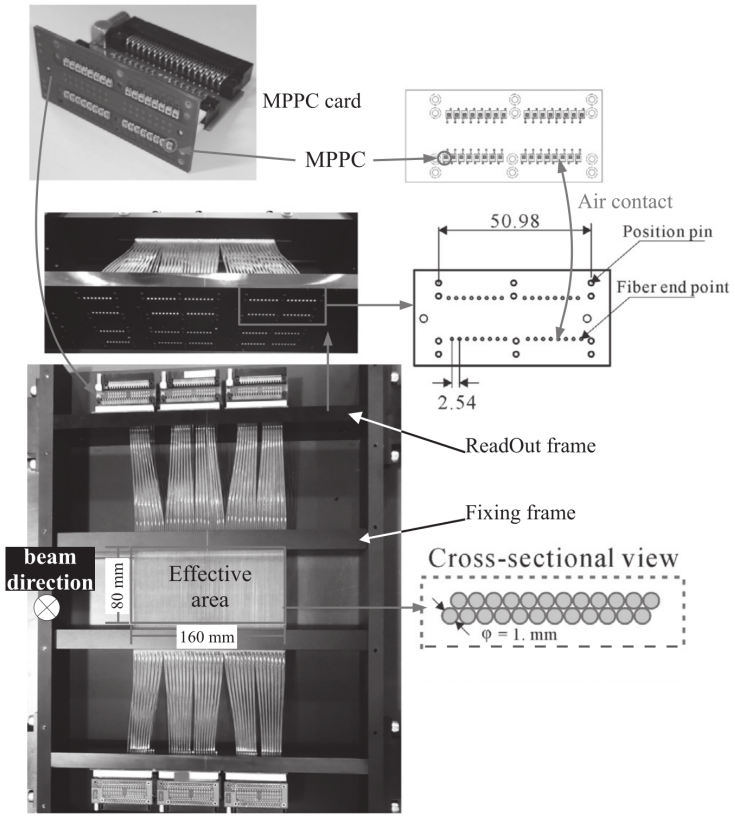

Figure 2.8: Pictures of BFT and the MPPC card for readout [47]. Edges of scintillating fibers were fixed to the ReadOut frame. By attaching the MPPC card to ReadOut frame with screws, MPPCs and scintillating fibers were contacted.

spectrometer. The KURAMA spectrometer comprises a dipole magnet (KURAMA magnet), plastic scintillating fiber tracker (SFT), fine segmented plastic scintillator hodoscopes (SCH, FHT1, and FHT2), an aerogel Cherenkov counter (SAC), three MWDCs (SDC1, SDC2, and SDC3), and a plastic scintillator wall (TOF). The KURAMA magnet was excited to 0.78 T at the central position. The trajectories of the charged particles in the magnetic field were reconstructed using the Runge-Kutta method [48]. Their momenta were obtained as the best momenta to reproduce the hit positions measured at the tracking detectors. The time-of-flight of the outgoing particle along a flight path of approximately 3m distance was measured using TOF. The spectrometer acceptance for K^+ in the $\pi^+ p \to K^+\Sigma^+$ reaction was approximately 6.7%, and the survival ratio of K^+ was 65%. The large acceptance and short flight length are advantages of the KURAMA spectrometer for accumulating many Σ^+ particles.

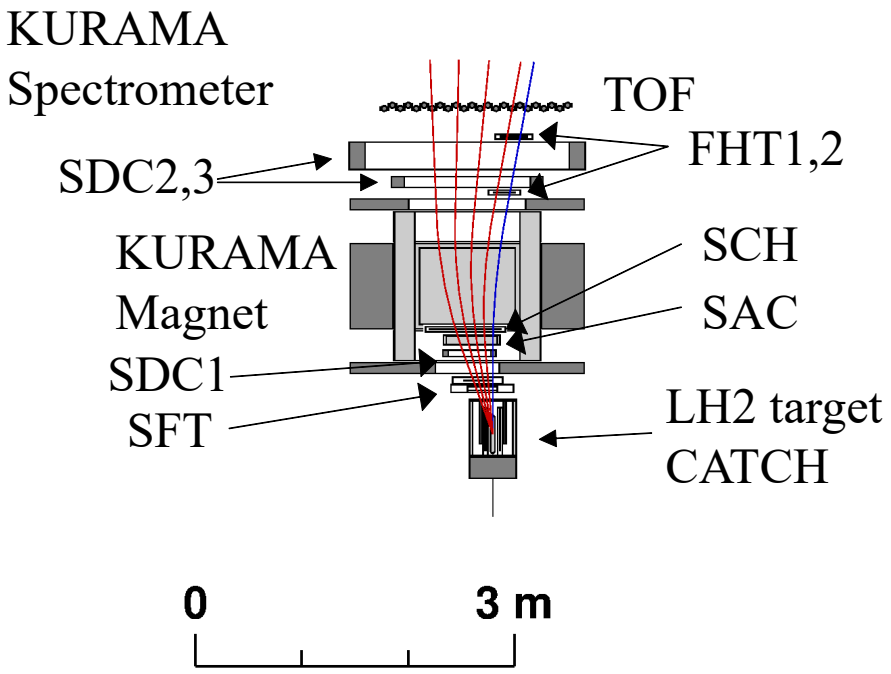

Figure 2.9: Schematic drawing of the KURAMA spectrometer. The KURAMA spectrometer comprised a dipole magnet (KURAMA manget), seven tracking detectors(SFT, SCH, SDC1, SDC2, SDC3, FHT1, and FHT2) and two counters (SAC and TOF). Five curves represent typical trajectory for expected particles. The blue curve corresponds to 1.4 GeV/c π^+ beam and the other four red curves correspond to K^+s following the kinematics of the $\pi^+ p \to K^+\Sigma^+$ reaction.

The effective areas and position resolutions of the detectors are summarized in Table 2.2. More detailed information on detectors is described in the following subsection. As shown the blue curve in Figure 2.9, 1.4 GeV/c π^+ beam particles can pass through the KURAMA spectrometer. Therefore, high-rate π^+ beam particles would hit detectors. To operate the detectors stably and suppress triggers caused by unexpected beam interaction under such an experimental condition, countermeasures were applied to most of the detectors. These countermeasures are also introduced in the following subsection. As for the KURAMA magnet, its horizontal center was shifted from the beam axis and beams passed through at the side region of the KURAMA magnet. K^+s scattered to the left side were detected by the KURAMA spectrometer.

2.5.1 Detectors in the KURAMA spectrometer

SFT

SFT is located most upstream of the KURAMA spectrometer. It comprises two independent frames, x frame and uv frame. As a tracker, it has three planes (xuv) and enough high-rate tolerance. Information on hit positions of SFT is also used 3D-Matrix trigger.

The design of SFT-x frame shown in Figure 2.10 is similar to BFT. It has a two-layers configuration (xx') made of 512 scintillation fibers (Kuraray SCSF-78MJ) with a

Table 2.2: Effective areas and position resolutions of detectors in the KURAMA spectrometer.

Detector	type	role	effective area H × V [mm^2]	$\sigma_{\rm pos}$ [mm]
SFT	fiber tracker	tracker, trigger	280 × 160	0.18
SDC1	drift chamber	tracker	380 × 264	0.30
SAC	aerogel Cherenkov counter	trigger	484 × 402	–
SCH	scintillator hodoscope	trigger, tracker	673 × 450	6.0
FHT1	scintillator hodoscope	tracker	196 × 450	0.58
SDC2	drift chamber	tracker	1185 × 1185	0.40
SDC3	drift chamber	tracker	1920 × 1280	0.40
FHT2	scintillator hodoscope	tracker	256 × 450	0.58
TOF	scintillator wall	trigger, (tracker)	1800 × 1800	40(H), 20(V)

diameter of 1 mm. Scintillation signals are read by a MPPC (Hamamatsu S10362-11-100P) attached at an end of each fiber. The effective area and position resolution of SFT-x plane are 256 mm (H) × 160 mm (V) and 180μm, respectively.

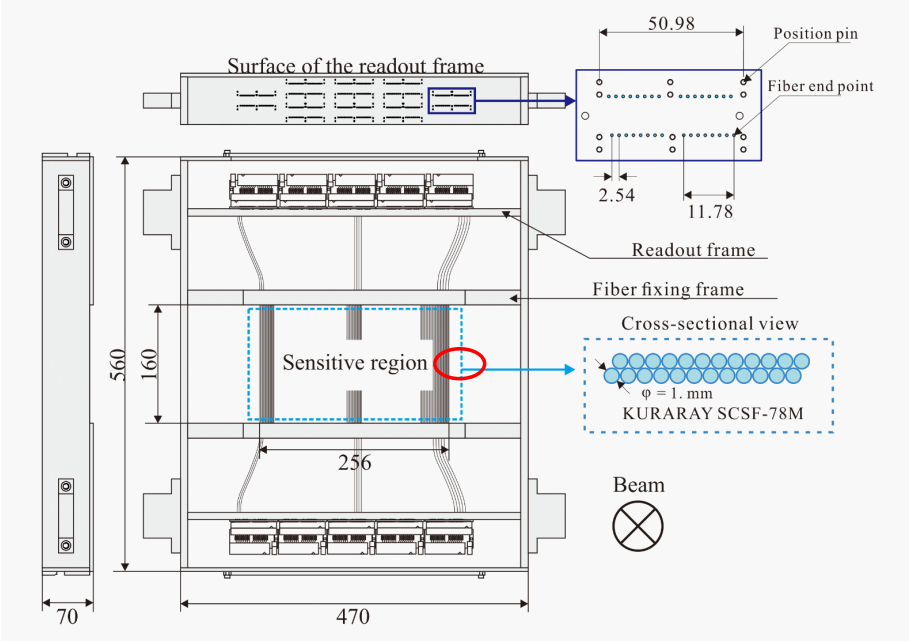

Figure 2.10: Schematic drawings of SFT x frame. The beam spot is roughly indicated as red elipses.

The design of SFT-uv frame is shown in Figure 2.11. The uv layers are made of 960 scintillation fibers (Kuraray SCSF-78MJ) with a diameter of 0.5 mm. u and v planes are tilted ±45°, respectively. Scintillation signals from three fibers are read using one MPPC (Hamamatsu S10362-11-100P) as shown in the right side of Figure 2.11. The effective area and position resolution of uv plane are 280 mm (H) × 160 mm (V) and 260 μm,

respectively.

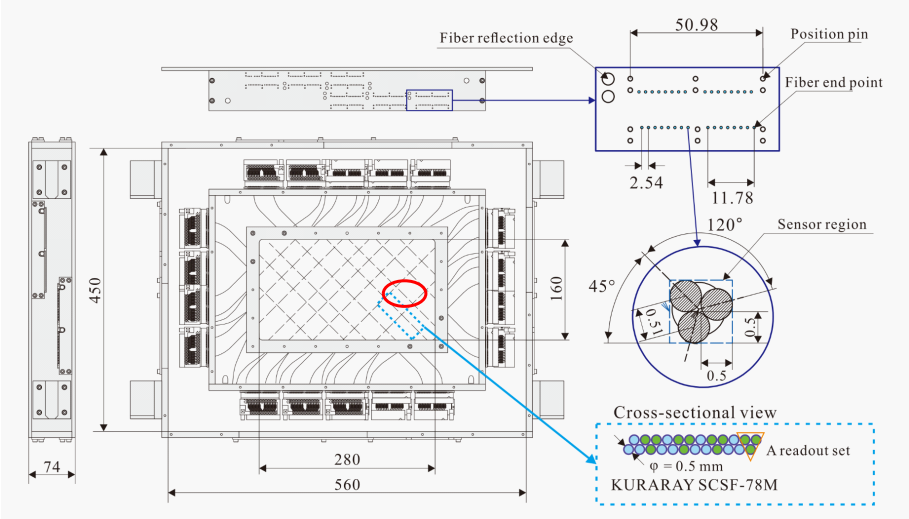

Figure 2.11: Schematic drawings of SFT uv frame. The beam spot is roughly indicated as red elipses.

The beam spot is roughly indicated as red ellipses in Figure 2.10 and Figure 2.11. In SFT-uv, there are aluminum support frame at all sides. Therefore, the position of SFT-uv was determined to cover not only the acceptance for K^+ but also the all beam region. On the other hand, there is no support frame at beam region for SFT-x and its position was determined to cover the acceptance for the scattered particles.

SDC1

SDC1, a MWDC, was located at the entrance of the KURAMA magnet. It has a six layers configuration ($vv'xx'uu'$), where u and v planes are tilted $\pm 15°$, respectively. The configuration of wires is shown in Figure 2.12. Each anode wire is surrounded by six potential wires forming a hexagonal cell structure, called honeycomb structure and anode wire pitch is 6 mm. Anode wires are made of gold-plated tungsten-rhenium (Au-W/Re) wires with a diameter of 20 μm. Potential and shield wires are made of gold-plated aluminum wires with a diameter of 80 μm.

The gas and readout systems were common to BC3,4: A mixed gas of Ar(76%), iso-C_4H_{10} (20%), and methylal(4%) was filled and a raw signal from each wire was read by Amplifier Shaper Discriminator (ASD) card attached on the chamber. In operation, a high voltage of -1.56 kV for potential wires and $-1.6kV$ for shield wires were applied.

In order to avoid the high-rate beam particles, SDC1 was placed apart from the beam center so as to detect only scattering events from 3 to 30 degrees.

SAC

In order to reject scattered π particles at a trigger level, a threshold type Cherenkov counter with a refractive index of 1.1 was placed. The threshold index of Cherenkov radiation as a function of particle momentum is shown in Figure 2.13. Figure 2.14 shows the schematic drawing of SAC. SAC comprises four segments (rooms) with different sizes,

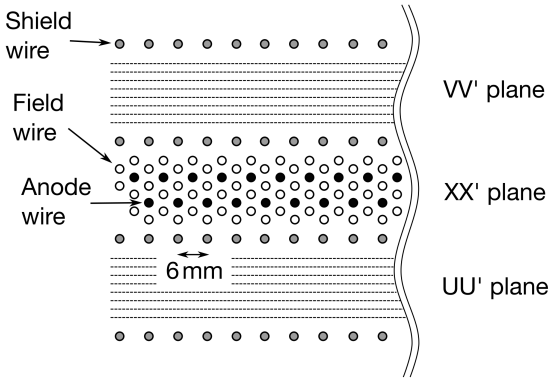

Figure 2.12: Schematic drawings of SDC1 wire configuration.

which was designed taking into account the singles rate. Near the beam spot, SAC has a hole, which prevents SAC from making unwanted veto signals due to beam π^+ particles. Cherenkov lights are detected by the Fine mesh PMTs (Hamamatsu R6682). Although PMTs were in the magnetic fields of approximately 0.3 T, gains were maintained above 90%.

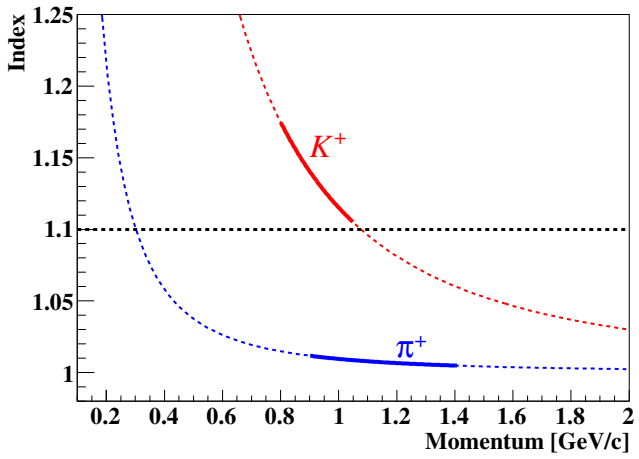

Figure 2.13: Threshold index of Cherenkov radiation as a function of particle momentum. Red and blue lines corresponds to scattered K^+ and π^+, respectively. Expected momentum regions of K^+ and π^+ were drawn with real lines. The refractive index of 1.1 is enough to discriminate π^+ and K^+ in this experiment.

SCH

A hodoscope was located at the entrance of the KURAMA magnet. Figure 2.15 shows the schematic drawing of SCH. SCH consists of 64 segments of plastic scintillators (EJ212) with a size of 11.5 mm (H) $\times$ 450 mm (V) $\times$ 2 mm (T). Each segment is arranged in a staggered relation with an overlap of 1 mm with each other. A wave length shifting fiber

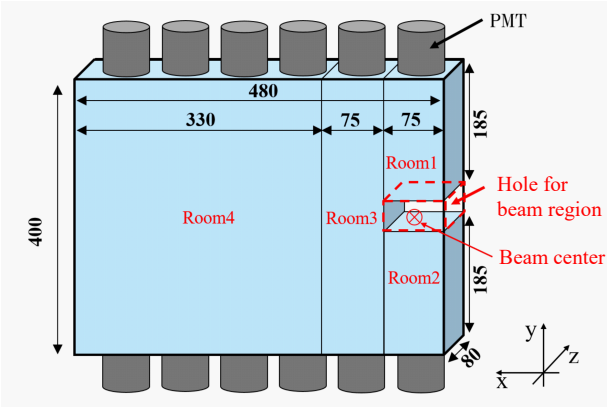

Figure 2.14: Schematic drawings of SAC [49].

(Kuraray PSFY-11J) with a diameter of 1 mm is put in a hole on the scintillator surface. Then the scintillation signals are read using a MPPC connected to an end of the fiber. SCH was primarily a trigger counter used to make Matrix trigger. However, it was also used as a tracker especially for particles near the beam spot, where many other trackers were made insensitive.

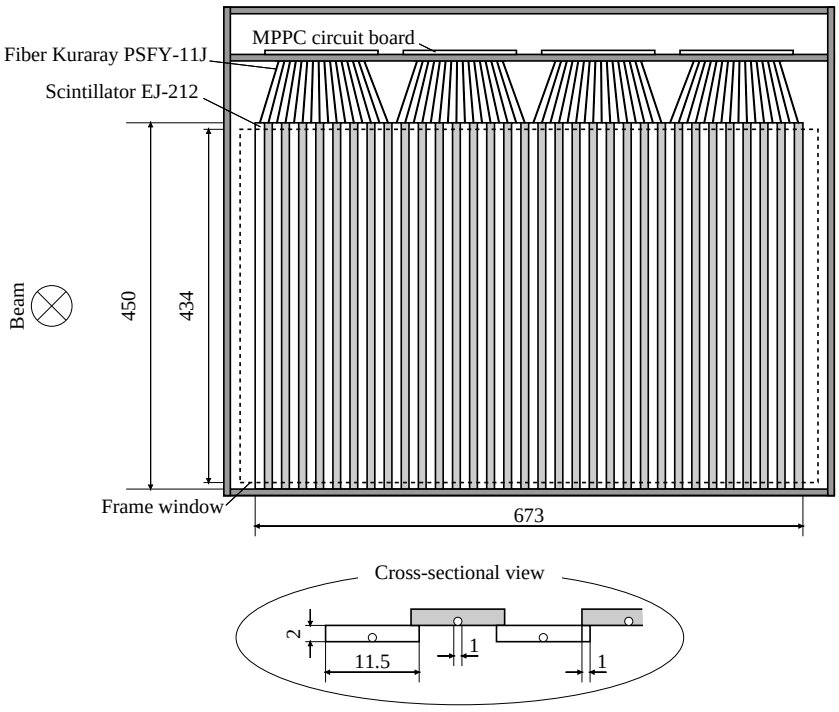

Figure 2.15: Schematic drawings of SCH.

SDC2 and SDC3

Two MWDCs were located dounstream of the KURAMA magnet. Both chambers had a four plane configuration ($xx'yy'$) and honeycomb wire structure as SDC1. Anode wire pitches of SDC2 and SDC3 are 9 mm and 20mm, respectively. The specifications of

SDC2,3 wires are summarized in Table 2.3.

Table 2.3: Specifications of SDC2,3 wires.

Chamber	Anode	Potential	Shield
SDC2	20 μm gold-plated W	100 μm gold-plated Al	100 μm gold-plated Al
SDC3	30 μm gold-plated W	50 μm gold-plated CuBe	50 μm gold-plated CuBe

A mixed gas of Ar (50%) and ethane (50%) was filled in SDC2 and SDC3 and kept flowing. A signal from each wire are processed by pre-amplifier card, which is attached on the chambers, and an amplifier discriminator board. In SDC2 operation, a high voltage of -2.05 kV for potential wires and -1.5 kV for shield wires were applied. For SDC3, a high voltage of -2.6 kV and -1.5 kV were applied to potential and shield wires, respectively.

Because SDC2 and SDC3 doesn't have enough high-rate tolerance for beam particles, the wires of SDC2 and SDC3 near the beam region were made insensitive by not applying the operation voltage to the potential wires. Both SDC2 and SDC3 lost about 10% and 5% of their effective area in the horizontal and vertical directions, respectively.

FHT1 and FHT2

Two sets of hodoscopes, which was used as additional trackers, was located just upstream of SDC2 and downstream of SDC3 to cover horizontal insensitive area of SDC2 and SDC3. Figure 2.16 shows the setup of SDC3 and FHT2. Each of FHT1 and FHT2 comprises two same detectors, upper and downer one. Although the segment size is different, structure of FHT is similar to SCH: Plastic scintillator (EJ212), which have a hole on the scintillator surface, with a size of 6 mm (H) $\times$ 550 mm (V) $\times$ 2mm (T) is arranged in a staggered relation with an overlap of 2mm with each other. A wave length shifting fiber (Kuraray PSFY-11J) with a diameter of 1 mm is put in a hole on the scintillator surface and the scintillation signals are read using a MPPC connected to an end of the fiber. A detector of FHT1 has 96 scintillator segments and the effective area of 196 mm (H) $\times$ 450 mm (V). On the other hand, A detector of FHT2 has 128 scintillator segments and the effective area of 256 mm (H) $\times$ 450 mm (V).

TOF

The plastic scintillator wall was located most downstream of KURAMA spectrometer. Flight length of a scattered particle from the targets to TOF is approximately 3 m. Figure 2.17 shows the schematic drawing of the TOF. TOF consists of 24 segments of plastic scintillators (EJ200) with a size of 80 mm (H) $\times$ 1800 mm (V) $\times$ 30 mm (T). The scintillators are arranged in a staggered relation with an overlap of 5 mm each other. Scintillation signals are read by two PMTs (Hamamatsu H1945) attached on the both vertical ends of the scintillator through light guides. To prevent beam particles from making unwanted triggers, special TOF segments were prepared. In the special TOF segment, the vertical center region of 20-cm length was substituted by an acrylic bar. Owing to this prescription, TOF became insensitive to beam particles, keeping sufficient acceptance for scattered particles.

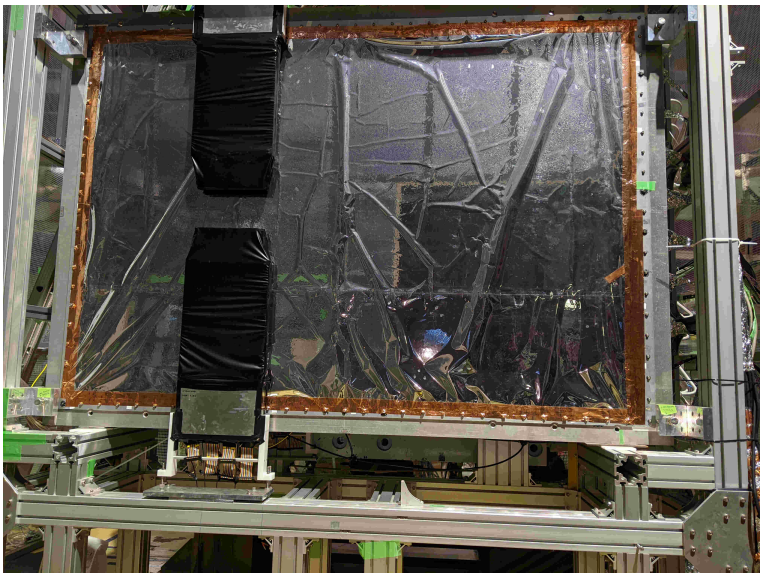

Figure 2.16: Photo of SDC3 and FHT2 setup.

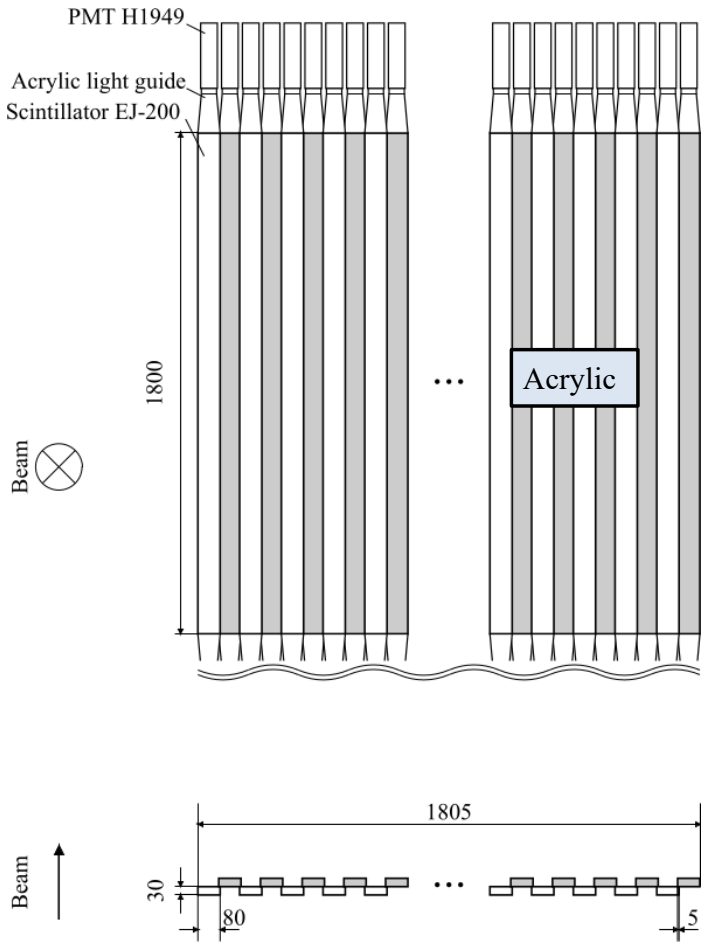

Figure 2.17: Schematic drawings of TOF. Six segments near the π^+ beam spot were changed to the special segments, where the vertical center region of 20-cm length was substituted by an acrylic bar.

2.6 Liquid-hydrogen (LH_2) target

Figure 2.18 shows the schematic drawings of the LH_2 target system. In this system, the hydrogen target is cooled by a heat exchanger using a GM cyrocooler. Figure 2.19 shows the drawings of the LH_2 target container, which is mainly made from a Mylar sheet of 0.25 mm thickness. It is cylindrical container of diameter 40 mm and length 300 mm with half-sphere end-caps at both edges. A vaccum window around the target region is created using a CFRP cylinder of diameter 80 mm and thickness 1 mm. The target density was continuously measured via the monitored gas pressure. It was 0.070743(4) g/cm^3.

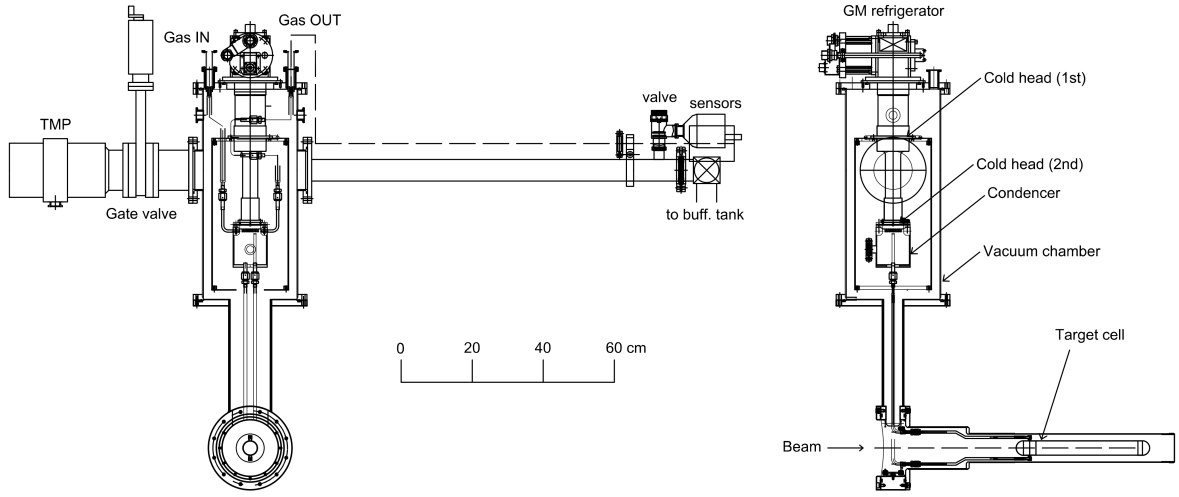

Figure 2.18: Schematic drawings of the LH_2 target system.

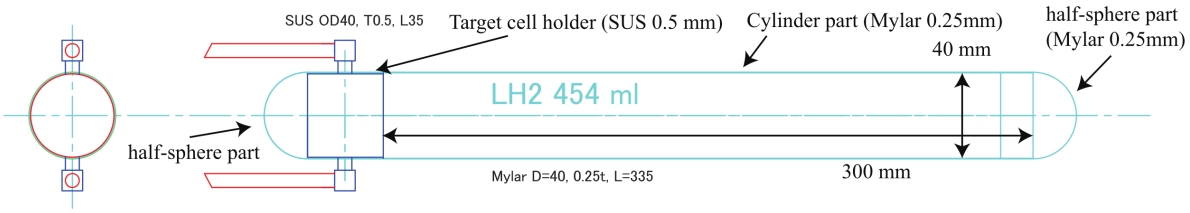

Figure 2.19: Drawings of the LH_2 target container.

2.7 CATCH

Charged particles involved in Σ^+p scattering, such as the recoil proton and decay products of Σ^+, were detected using detector system, CATCH [39]. Figure 2.20 shows the schematic drawings of CATCH. CATCH surrounded the LH_2 target and comprised a cylindrical fiber tracker (CFT), BGO calorimeter (BGO), and plastic scintillator hodoscope (PiID). The trajectory was reconstructed using CFT and the kinetic energy was measured by

summing the energy deposits in CFT and BGO on the reconstructed trajectory. Using the correlation of energy loss in CFT and total energy deposit in CATCH, protons can be distinguished from $\pi^{\pm}$ and $e^{\pm}$.

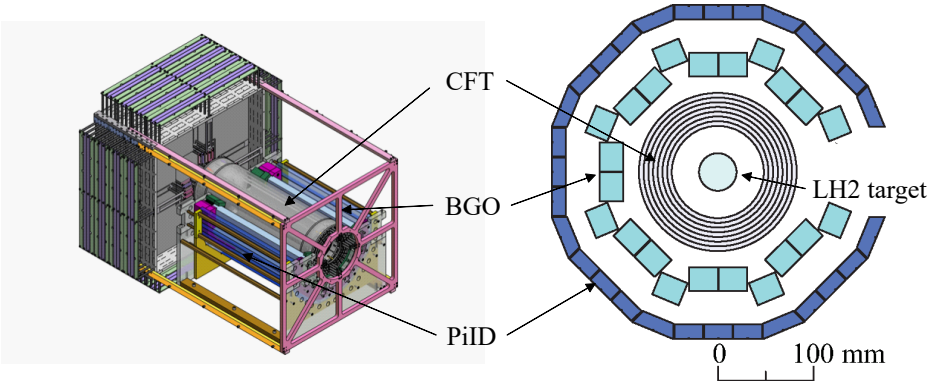

Figure 2.20: Schematic drawings of CATCH, perspective view (Left) and cross-sectional view (Right). The BGO and PiID segments overlapping the K^+ path to the KURAMA spectrometer were removed.

2.7.1 Detectors of CATCH

CFT

A cylindrical fiber tracker with 400-mm length along the beam axis surrounds a LH_2 target and reconstructs tracks of charged particles from the target. CFT comprises eight cylindrical layers of plastic scintillation fibers (Kuraray SCSF-78M) with a diameter of 1 mm. Scintillation signals are read using a MPPC (Hamamatsu S10362-11-050P) contacted at an end of each fiber. Radial distance and number of fibers for each layer are summarized in Table 2.4 and the schematic drawings of the fiber arrangements are shown in Figure 2.21. The fibers are placed parallel to the beam axis in four layers, called ϕ layers. In the other four layers, called uv layers, fibers are arranged in a spiral shape. This configuration enables the reconstruction of trajectories in three dimensions.

Table 2.4: Radial distance and number of fibers for each layer of CFT.

ϕ layer	$\phi 1$	$\phi 2$	$\phi 3$	$\phi 4$
Radial distance [mm]	54	64	74	84
Number of fibers	584	692	800	910
uv layer	$u1$	$v2$	$u3$	$v4$
Radial distance [mm]	49	59	69	79
Number of fibers	426	472	510	538
Tilt angle [degree]	37.6	42.8	47.3	51.1

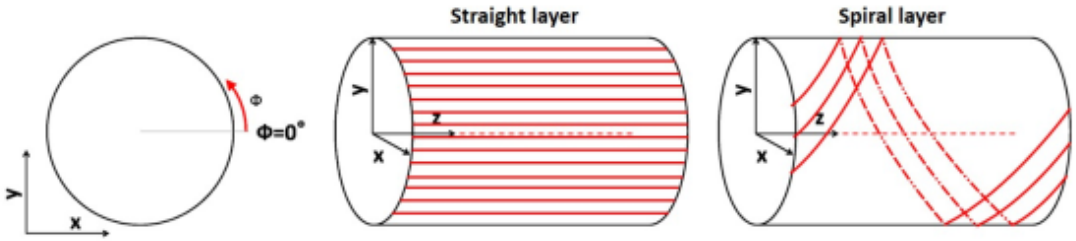

Figure 2.21: Schematic drawings of the CFT fiber arrangements for so-called ϕ and uv layers [39].

BGO

A calorimeter was placed outside around CFT to measure the kinetic energy of protons from $\Sigma^+ p$ scattering by stopping it in the calorimeter. The size of each BGO crystal is 400 mm (l) $\times$ 30 mm (w) $\times$ 25 mm (t). Scintillation signals are read using PMT (Hamamatsu H1 1934-100) attached at an end of each BGO crystals. In the present experiment, the average singles rate of a BGO segment was 80 k/spill and a raw signal from BGO has a relatively long decay time of 300 ns. In order to decompose the pile-up events, the waveform readout is needed. The raw BGO signal is filtered with a integral circuit and shaped to the suitable waveform for the flash ADC readout as shown in Figure 2.22. Then, the waveforms were recorded by a flash ADC module (CAEN V1724) with a sampling frequency of 33 MHz. From the recorded waveform, the pulse height information is reconstructed by fitting the data point with a template waveform.

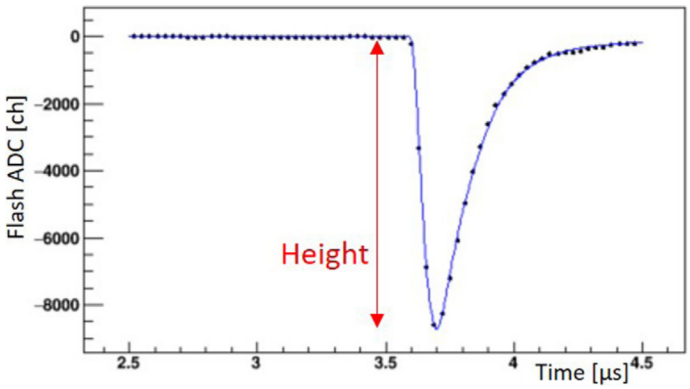

Figure 2.22: Typical waveform of the BGO calorimeter after the shaping circuit [39]. The black points show the flash ADC data with a sampling rate of 33 MHz. The blue line shows the reconstructed pulse shape by fitting the data point with a template waveform.

PiID

A hodoscope was located most outside of CATCH to determine whether the charged particles penetrated BGO or not. PiID comprises 32 plastic scintillators (EJ212) with a size of 400 mm (l) $\times$ 30 mm (w) $\times$ 15 mm (t). As SCH and FHT, each scintillator has a

hole on the scintillator surface to put a wave length shifting fiber (Kuraray Y-11 (200)M) with a diameter of 1 mm. Scintillation signals are read using a MPPC (Hamamatsu S10362-11-100P) attached to an end of the fiber.

2.8 Trigger

In the data taking, the (π^+, K^+) events were selected by the first- and second- level triggers. Figure 2.23 shows the diagram of the trigger system. From the logic signals from the trigger counters, trigger signal was made using three FPGA-based modules, HUL trigger [50], HUL martix trigger, and HUL mass trigger modules.

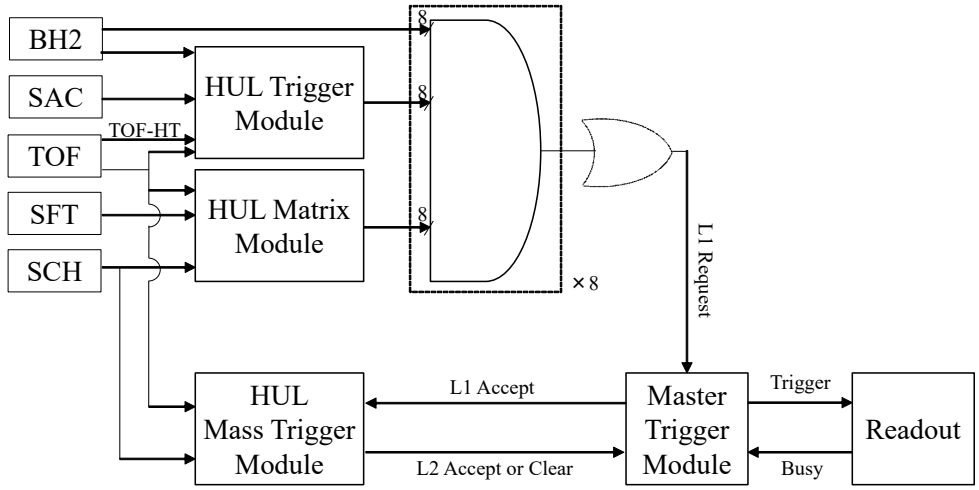

Figure 2.23: Diagram of the trigger system. BH2 × TOF × $\overline{\text{SAC}}$ × $\overline{\text{TOF}_{\text{large}dE}}$ logical signal were generated in the HUL trigger module. 2D- and 3D- matrix trigger signals were generated by the HUL Matrix trigger module. The 2nd-level trigger is decided by the HUL mass trigger module.

The first-level πK trigger is defined as

$$\text{BH2} \times \text{TOF} \times \overline{\text{SAC}} \times \overline{\text{TOF}_{\text{large}dE}} \times \overline{\text{2DMtx}} \times \text{3DMtx}, \tag{2.1}$$

where $\text{TOF}_{\text{large}dE}$ is a veto signal using the pulse height of TOF. It could reject particles with small β, that is, mainly protons with low momenta. 2DMtx and 3DMtx represent two types of matrix triggers, in which combinations of hit segments of SCH, TOF, and SFT x plane were used to decide the trigger. Figure 2.24 shows the correlations of the SCH and TOF hit segments. In the left figure of Figure 2.24, we can see the vertical-stripe like event concentration around SCH segment 10. It corresponds to events from interaction due to beam particles or beam particles themselves. Therefore, 2DMtx veto region was determined to reject these events. On the other hand, the 3DMtx accepted region was determined based on the result of the K^+ identification analysis. Because the momenta of the scattered K^+ were strongly correlated with the hit segment combinations, the matrix trigger was quite effective to suppress the trigger rate. The trigger timing was determined as the BH2 timing, by taking the coincidence of the BH2 and first-level trigger

signals. The coincidence logical signals were created for each segment of BH2 and then summed in order to prevent saturation of the OR signal due to the high intensity beam.

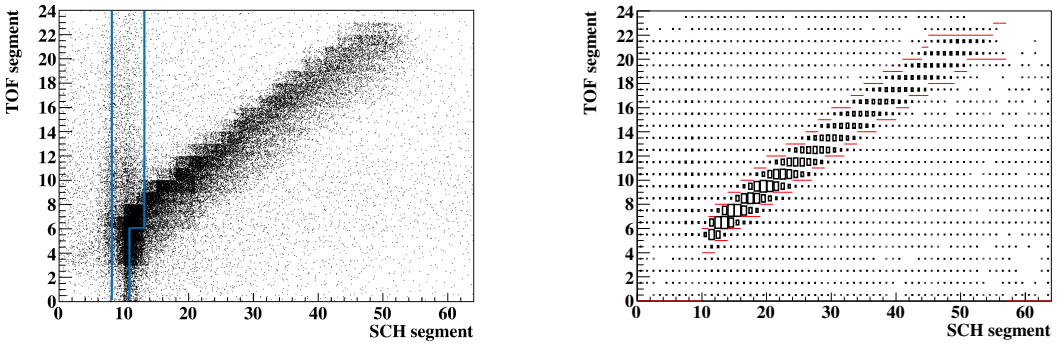

Figure 2.24: Correlations of the SCH and TOF hit segments for all events without matrix triggers (Left) and K^+ events (Right). The region within blue lines in the left figure indicates 2DMtx veto region. The 3DMtx accepted region is inside of the red lines in the right figure.

In addition to momentum information from the hit segment combinations, selecting the time-of-flight of the scattered particle enables us to identify K^+ more correctly. This is a principle of the second-level trigger called "mass trigger." TOF timings, which correspond to the time-of-flight between BH2 and TOF, were recorded by a high-resolution TDC in the HUL mass trigger module and the second-level trigger was decided. The gate of the mass trigger was optimized for each combination of SCH and TOF, which was accepted by 3DMtx. A typical gate width was 4 ns. Figure 2.25 shows the TOF timing distribution by particle species. Owing to the mass trigger, many background protons and pions were prevented from making triggers.

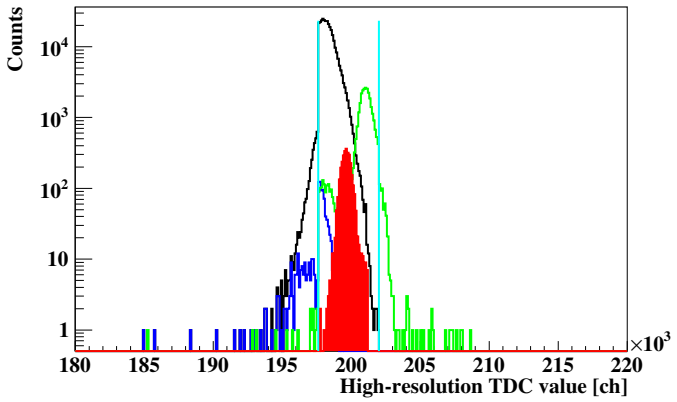

Figure 2.25: TOF timing distribution, which corresponds to the time-of-flight between BH2 and TOF, for a combination of TOF and SCH hit segment. The red filled histogram corresponds to K^+ event. The green, black, blue lines corresponds to π^+, proton, and relatively low momentum (<0.9 GeV/c) proton, respectively. The light blue vertical lines represents the time-of-flight gate to decide the mass trigger.

2.9 DAQ

A network controlled system was adopted to the data acquisition (DAQ) system of K1.8 beam line. Figure 2.26 shows a diagram of the DAQ system in the K1.8 beam line. Data from each detector was read out through each subsystem. In order to synchronize the event between different subsystems, a trigger managing system using a master trigger module (MTM) and a receiver module (RM) were adopted. The trigger managing system distributed an event tag, which comprises spill number and event number, to each subsystem.

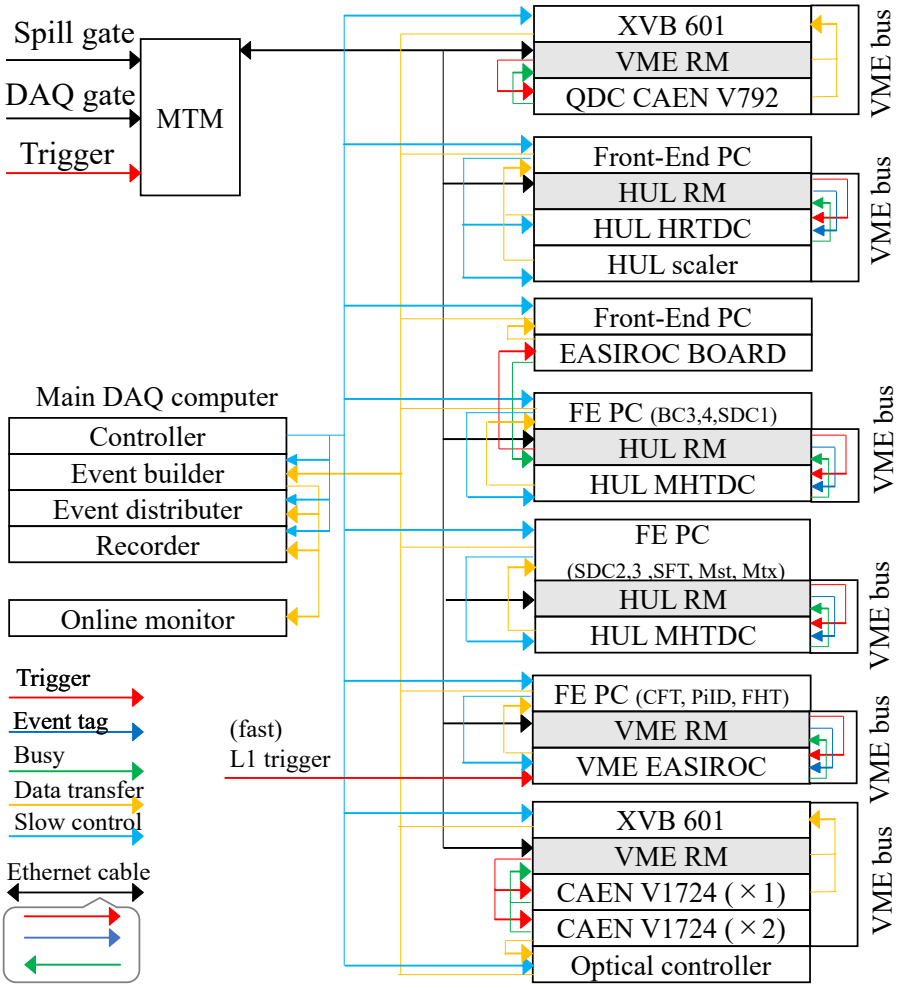

Figure 2.26: Schematic diagram of the DAQ system in the K1.8 beam line.

Regarding the readout modules, Hadron Universal Logic (HUL) modules [51] has been developed recently. This FPGA-based modules has good extensibility by changing the mezzanine cards. In the present experiment, HUL RM, HUL Multihit TDC (MHTDC), and HUL High-resolution TDC (HRTDC) were extensively used. Pulse height information on BH1, BH2, TOF, and SAC were recorded using CAEN V792 modules, which were controlled by VME-CPU module (XVB 601). Timing information on BH1, BH2, TOF were recorded using HUL HRTDC. MPPC signals were read by the two types of EASIROC modules: EASIROC test board and VME-EASIROC module. Details of these EASIROC

modules are explained in Ref. [52] and [39], respectively. Timing information on BFT and SCH were recorded by EASIROC test boards. Although signals from SFT were amplified, shaped, and discriminated in EASIROC test boards, discriminated timing signals were recorded by the HUL MHTDC modules. Both timing and pulse height information on CFT, FHT, PiID were recorded using VME-EASIROC modules. The waveforms of signals from BGO calorimeter were recorded using three flash ADC modules, CAEN V1724, controlled by VME-CPU module. In order to reduce the data transfer time, one module was read by the VME-CPU module and the other two module were read by so-called optical controller computer. Signals of all drift chambers were recorded using the HUL MHTDC modules.

Digitized signals from each sub system were collected to the host computer. A part of data were distributed to the online monitor system to check the detector performances.

Typical DAQ performances and trigger rates in the data taking are summarized in Table 2.5.

Table 2.5: Typical DAQ performances and trigger rates in the data taking. For the events rejected by the Level 2 trigger, the Level 2 decision time was the effective DAQ dead time.

DAQ busy	30 μs
Level 2 decision time	4 μs
DAQ efficiency	82%
Data size	20.6 kB/event
Level 1 request	2.6×10^4 /spill
Level 1 accept	2.2×10^4 /spill
Level 2 clear	1.3×10^4 /spill
Level 2 accept	9×10^3/spill
Level 2 efficiency	41%

2.10 Data Summary

The Σ^+p scattering data taking of J-PARC E40 experiment was performed in April 2019 and May-June 2020 with the same experimental setup. In each period, we collected Σ^+p scattering data for approximately 240 hours of beam time. Pion On Target (POT) in 2019 and 2020 run were 3.89×10^{12} and 3.65×10^{12}, respectively. Additionally, pp scattering data using proton beams with various momenta between 0.45 and 0.85 GeV/c were collected. The pp scattering data were used for energy calibration and estimation of CATCH detection efficiency.

Chapter 3

Analysis flow and Monte Carlo simulation

3.1 Analysis flow

A conceptual drawing of the present experiment is shown again in Figure 3.1. Σ^+p scattering events can be identified by measuring the Σ^+ momentum, the recoil proton's kinetic energy and the proton's recoil angle.

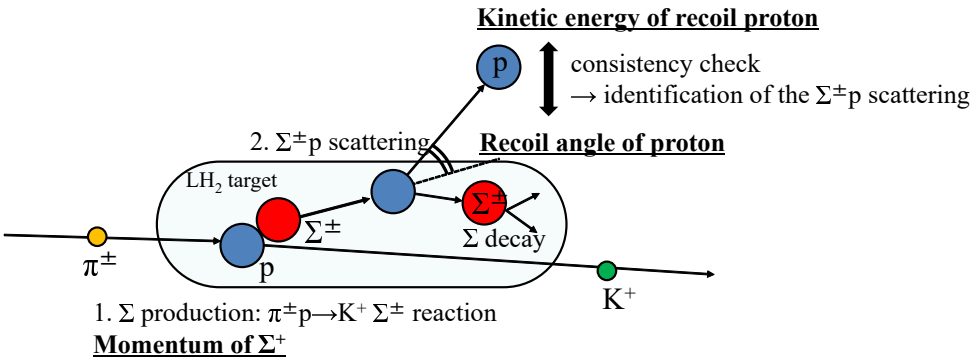

Figure 3.1: Conceptual drawing of the Σ^+p elastic scattering in the J-PARC E40 experiment same as Figure 2.1. The initial Σ^+ is produced by the $\pi^+p \to K^+\Sigma^+$ reaction. Then, it travels in the LH_2 target and may cause Σ^+p scattering. The Σ^+p elastic scattering can be kinematically identified by measuring the initial Σ^+'s momentum, the recoil proton's kinetic energy, and recoil angle.

The whole analysis flow to deriving the differential cross sections is summarized in Figure 3.2. The analysis of the Σ^+p scattering events comprises three stages. In the first stage analysis, the spectrometer systems, K1.8 beam-line and KURAMA spectrometers, and CATCH were analyzed independently. From the analysis of spectrometer systems, Σ^+ production events were identified and the momentum of each Σ^+ was tagged. The trajectories of charged particles involved in Σ^+p scattering were reconstructed and kinetic energy of protons were measured using CATCH. In the second stage analysis, these informations were combined and Σ^+p scattering events were identified by requiring the

kinematical consistency for the recoil proton. In the third stage, factors to derive the differential cross sections, such as the Σ^+ total track length and efficiencies were evaluated. Finally, differential scattering cross sections were obtained. The each stage of analysis is described in Chapter 4, 5, and 6, respectively. The obtained differential cross sections were shown in Chapter 7.

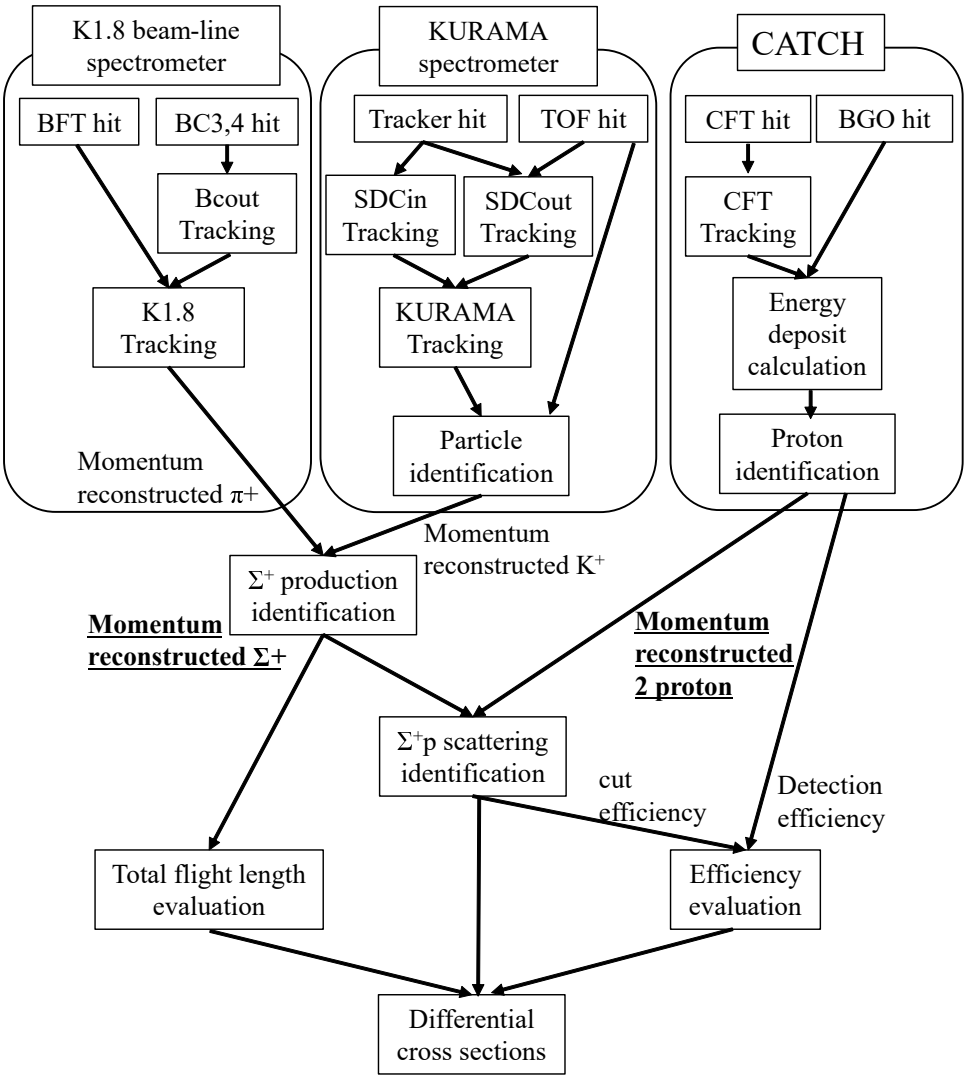

Figure 3.2: Analysis flow of differential cross section derivation for Σ^+p scattering.

3.2 Monte Carlo simulations

In the following analysis, a Monte Carlo simulation was performed for many purposes. In the simulation, the dedicated event generator was implemented. By selecting the mode of the event generator, the corresponding events were generated among several implemented reactions. The purposes and the implemented reactions are as follows.

1. Energy calibration of CATCH: The pp and π^+p elastic scatterings were generated to obtain the relation between the proton's scattering angles and energy deposits

in CFT and BGO for protons with a wide momentum range. This relation was compared to the real data for the CATCH energy calibration. The detail is described in Subsection 4.4.3.

2. The flight length evaluation of the Σ^+ beam: The flight length of Σ^+ in the LH_2 target was estimated by generating Σ^+ particles with the realistic momentum and position distribution. As the inputs of the Σ^+ momentum and position, the analysis results of the spectrometers were used. The detail is described in Section 6.2.

3. Evaluation of CATCH detection efficiency for protons: Protons with arbitrary angle and energy were generated for evaluating the detection efficiency with CATCH. The detail is described in Subsection 6.3.1.

4. $\Sigma^+ p$ scattering events simulation for background estimation and the overall efficiency evaluation of CATCH: The $\pi^+ p \to K^+ \Sigma^+$ reaction and the sequential secondary reactions in the LH_2 target were generated. Figure 3.3 shows the flow chart of the event generation. As the secondary reactions, not only the $\Sigma^+ p$ scattering but also background reactions that were the reactions between the Σ^+ decay products and proton, such as the pp scattering following the $\Sigma^+ \to p\pi^0$ decay, were implemented to reproduce the background structure. In this simulation, the differential cross section of the $\Sigma^+ p$ scattering was assumed to be 2.4 mb/sr with an isotropic angular distribution. Moreover, the secondary backgrounds were generated based on their cross sections. Further, accidental coincidence events were generated based on their measured probabilities described in Subsection 4.5.3.

The information about the generated particles by the event generator was transferred to the passage simulator based on Geant4 package [53]. In this simulator, the LH_2 target, all detectors and most materials of the KURAMA spectrometer and CATCH (the KURAMA magnet, the frames of CFT, and so on) were implemented. The interactions between the generated particles and experimental materials were simulated, and the information about the energy deposit and hit position in the virtual detectors was recorded considering the energy and position resolutions of the real detectors. The simulated records were analyzed in the same analysis program as the real data to compare between them.

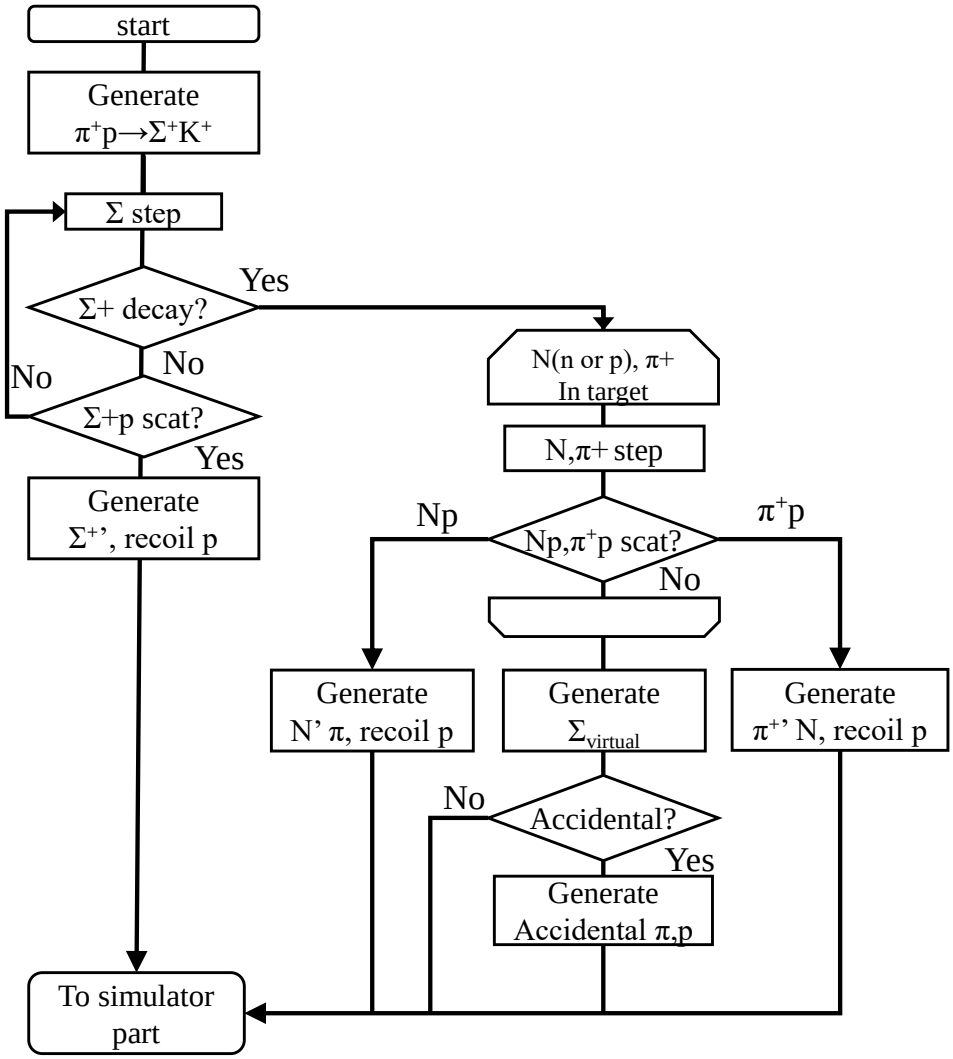

Figure 3.3: Flow chart of $\Sigma^+ p$ scattering and background generation in the event generator. The "step" means a series of procedure: Moving a particle to small displacement $\boldsymbol{x} + d\boldsymbol{x}$, the occurrences of decay or scattering were probabilistically judged and the energy loss in the displacement was calculated to iterate the particle momentum. When secondary Np and $\pi^+ p$ scattering does not occur, a virtual Σ^+ particle with a lifetime of 0 is generated at the decay point in order to reproduce mere Σ^+ decay events.

Chapter 4

Analysis-I:Analysis of spectrometers and CATCH

In this chapter, independent analyses of the spectrometer systems for Σ^+ production identification and CATCH for proton detection are described. The Σ^+ particles were identified from the missing mass spectrum of the $\pi^+ p \to K^+ X$ reaction. The particle identification and momentum reconstruction for both the π^+ beam and outgoing K^+ were performed with the K1.8 beam-line spectrometer and the KURAMA spectrometer, respectively. The momenta of the produced Σ^+ particles were obtained from the momenta of π^+ and K^+. The trajectories of the charged particles involved in $\Sigma^+ p$ scattering, such as the recoil proton from $\Sigma^+ p$ scattering and $\Sigma^+ \to p\pi^0$ decay were reconstructed and kinetic energy of protons were measured using CATCH.

4.1 π^+ analysis using the K1.8 beam-line spectrometer

The momenta of the π^+ beam particles were analyzed by the K1.8 beam-line spectrometer with the 3rd-order transfer matrix method. The x position at the entrance of the spectrometer was measured with BFT. The position and direction at the exit of it was reconstructed with two MWDCs (BC3, 4).

The contaminations of other particle species were negligibly small due to setup of ESS ,CM magnets and MS slits, which can be confirmed from the time-of flight spectrum between BH1 and BH2 shown in Figure 4.1. The time offset of time-of-flight was adjusted to π^+ for each BH1 segment. The typical time-of-flight resolution was 300 ps in σ. Because the slewing correction using the correlation between the pulse height and the timing could not be completely performed due to the signal pile-up under the high counting rate, this time-of-flight resolution was not the best value, while this resolution was enough to identify the time difference of $\sim$ 1.9 ns between 1.41 GeV/c π^+ and K^+.

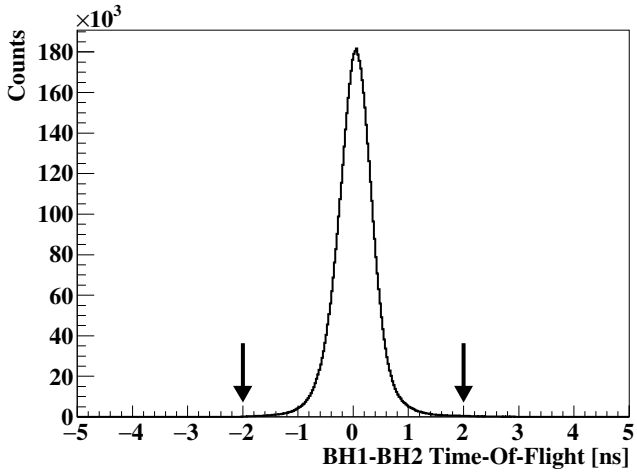

Figure 4.1: Time-of flight distribution between BH1 and BH2; These had a flight distance of 10.4 m.

4.1.1 BFT analysis

BFT measured the x position of beam particles upstream of the QQDQQ analyzer magnets. Because BFT had two layers configuration (xx') with an overlap, neighbor hits were clustered. A typical time resolution of BFT was about 900 ps in σ under the 20M/spill beam intensity and the time gate of $\pm$6 ns was applied to select the triggered event. 96.8% of the triggered events had at least one clustered hit. In about 40% of the triggered events, BFT had multi clustered hits including accidental hits. In order to reject accidental BFT hits, the correlation between the BH1 hit segment and BFT hit position, which is shown in Figure 4.2, was used. Applying this selection rule, the effective BFT multi clustered events were reduced to 9.6%.

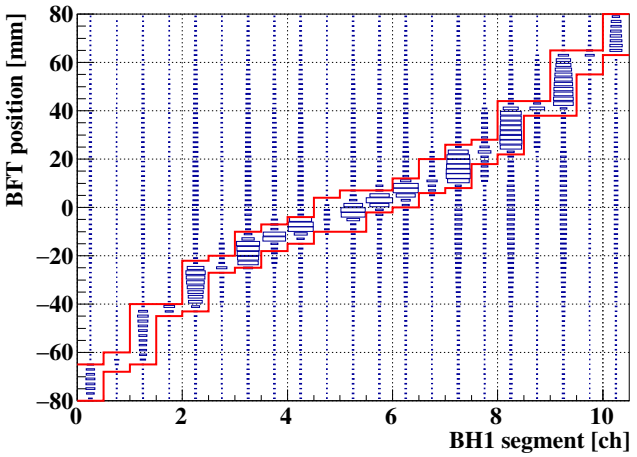

Figure 4.2: Correlation between BH1 hit segment and BFT hit position. When BFT had multi clustered hits, Only BFT hits lying within red lines were accepted.

4.1.2 Local Tracking for BCout (BCout Tracking)

The position and direction at the exit of the QQDQQ analyzer magnets were reconstructed using two MWDCs (BC3 and BC4). Both chambers had a six layers configuration ($xx'uu'vv'$) with 3-mm wire spacing. For a track candidate, which is the sets of hit information, the straight line fitting was performed to minimize the reduced chi-square as follows;

$$
\begin{aligned}
\chi^2/\mathrm{ndf} &= \frac{1}{N_{\mathrm{hit}}-4}\sum_{i=1}^{12} H_i\Big(\frac{X_i - f(z_i)}{\sigma_i}\Big)^2, \qquad (4.1)\\
X_i &= wp \pm dl_i(t),\\
f(z_i) &= x(z_i)\cos\alpha_i + y(z_i)\sin\alpha_i,\\
x(z_i) &= x_0 + u_0 z_i,\\
y(z_i) &= y_0 + v_0 z_i,\\
H_i &= \begin{cases} 1 & \text{(If a hit of } i\text{-th layer is included in the track candidate)} \\ 0 & \text{(otherwise)} \end{cases}\\
N_{\mathrm{hit}} &= \sum_{i=1}^{12} H_i \geq 8,
\end{aligned}
$$

where, x_0, y_0, u_0 and v_0 are the parameters representing the horizontal and vertical positions and angles of the track. The tilt angle and z position of i-th hit plane is denoted as α_i and z_i, respectively. The tilt angles α_i of xx', uu', and vv' planes were $0°$, $+15°$, and $-15°$, respectively. The local hit position in each layer, X_i was calculated by the position of hit wire (wp) and drift length(dl) which was calculated from the drift time (t) and the drift function. σ_i is the intrinsic resolution of each plane, typically 200 μm. When the layers had multiple hit wires, all possible track candidates were fitted in order to find the most probable track by sorting them according to the χ^2/ndf. In order to prevent combinatorial explosion, a correlation between the hit wires and hit segment of BH2 was used. The typical reduced chi-square distribution is shown in Figure 4.3. The threshold was set to 10 in order to select good events.

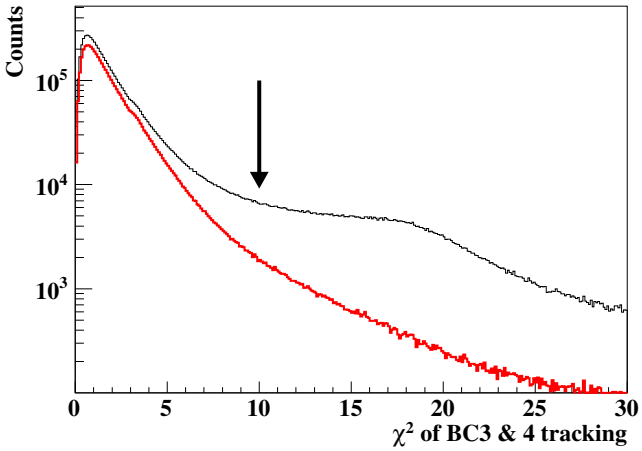

Figure 4.3: Distribution of the reduced chi-square of BCout tracking. The black and red lines show the total and single-track events, respectively.

4.1.3 K1.8 Tracking

The π^+ beam momentum was reconstructed by connecting the upstream horizontal position and downstream trajectory using the 3rd-order transfer matrix. The transfer matrix of the K1.8 beam-line spectrometer with QQDQQ analyzer magnets configuration was calculated using ORBIT code [54]. Horizontal position at the entrance $x_{\rm in}$ was measured using BFT and positions and angles at the exit, $x_{\rm out}, y_{\rm out}, u_{\rm out}$, and $v_{\rm out}$ were analyzed by BCout tracking. Using inverse transfer matrix M (for i-th order, denoted as $M^{(i)}$) , $x_{\rm in}$ can be written with $x_{\rm out}, y_{\rm out}, u_{\rm out}, v_{\rm out}$, and the momentum deviation from the central momentum δ as

$$x_{\rm in} = \sum_{i=1}^{5} M^{(1)}_{1i}\xi_i + \sum_{i,j} M^{(2)}_{1ij}\xi_i\xi_j + \sum_{i,j,k} M^{(3)}_{1ijk}\xi_i\xi_j\xi_k, \tag{4.2}$$
$$\boldsymbol{\xi} = (x_{\rm out}, u_{\rm out}, y_{\rm out}, v_{\rm out}, \delta).$$

The equation (4.2) can be regarded as a cubic equation for δ and the beam momentum is obtained as a general solution of the equation. The momentum resolution of the K1.8 beam-line spectrometer σ_p/p in designed value is better than 1×10^{-3} [46]. The reconstructed momentum distribution of π^+ beam is shown in Figure 4.4. The spread of momentum distribution is mainly determined by the setting of the momentum slit in the beam line.

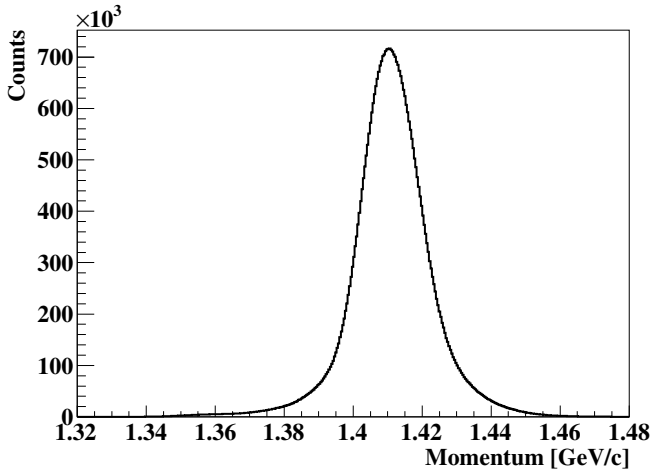

Figure 4.4: Momentum distribution of the π^+ beam analyzed by the K1.8 beam-line spectrometer.

4.2 K^+ analysis using the KURAMA spectrometer

The outgoing tracks produced from the LH_2 target by the $\pi^+ p$ reaction were analyzed by the KURAMA spectrometer. The trajectories of the outgoing particles in the magnetic field were traced with Runge-Kutta method [48], based on equation of motion defined by the initial parameters, namely, the momentum vector and the position at TOF. The parameters were optimized in order to reproduce a set of hit positions measured by the tracking detectors. This procedure is called "KURAMA Tracking". In order to determine the set of the hit information used by KURAMA Tracking, local straight line trackings upstream and downstream of the KURAMA spectrometer were performed. These local tracking are called "SDCin Tracking" and "SDCout Tracking", respectively.

The setup of the KURAMA spectrometer is shown again in Figure 4.5. Not only scattered particles but also π^+ beam particles pass through the KURAMA spectrometer. Because the drift chambers cannot be operated stably under the high intensity beam of 2.0×10^7/spill, three MWDCs (SDC1-3) were made insensitive to beam particles. SDC1 was apart from the beam center and insensitive to particles near the beam spot. SDC2 and SDC3 had cross-shaped insensitive areas as shown in Figure 4.6. The horizontal insensitive areas were covered by FHT1 and FHT2. However, the vertical insensitive were not recovered. Therefore, vertical positions of particles near the beam height were not measured by the SDC2 and SDC3.

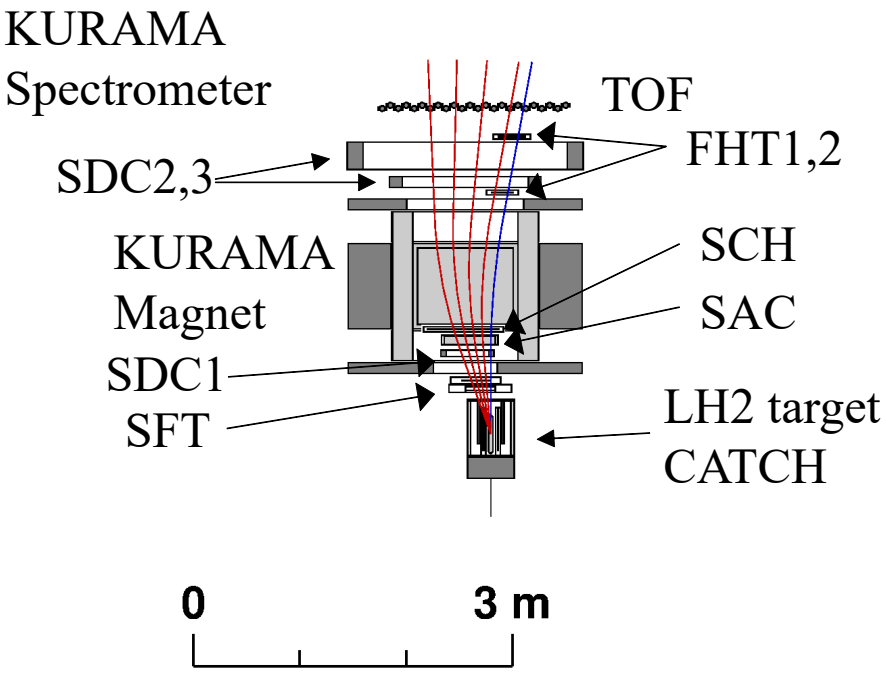

Figure 4.5: Schematic drawing of the KURAMA spectrometer same as Figure 2.9. Five curves represent typical trajectory for expected particles. The blue curve corresponds to 1.4 GeV/c π^+ beam and the other four red curves correspond to K^+s following the kinematics of the $\pi^+ p \to K^+\Sigma^+$ reaction. "SDCin Tracking" was performed using hits of SFT, SDC1, and SCH. "SDCout tracking" use hit information on SDC2, SDC3, FHT1, FHT2 and TOF.

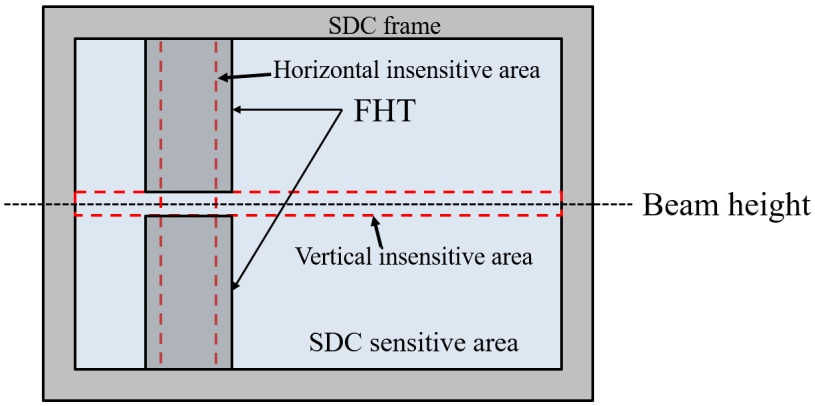

Figure 4.6: Rough sketch of insensitive region in SDC2 or SDC3. The area surrounded by red dotted lines indicates insensitive region of SDC and the beam particles passed through around the center of cross-shape, where SDCs were completely insensitive. Although the horizontal insensitive areas were covered by FHT, the vertical insensitive areas could not be recovered.

Because K^+ with small scattering angles had a similar trajectory to beam particles,

particles near the beam spot (in SDCin Tracking) and near the beam height (in SDCout Tracking) should be analyzed as many as possible. For this purpose, looser tracking scheme is applied to particles near the beam spot and height. The flow of SDCin and SDCout tracking were shown in Figure 4.7.

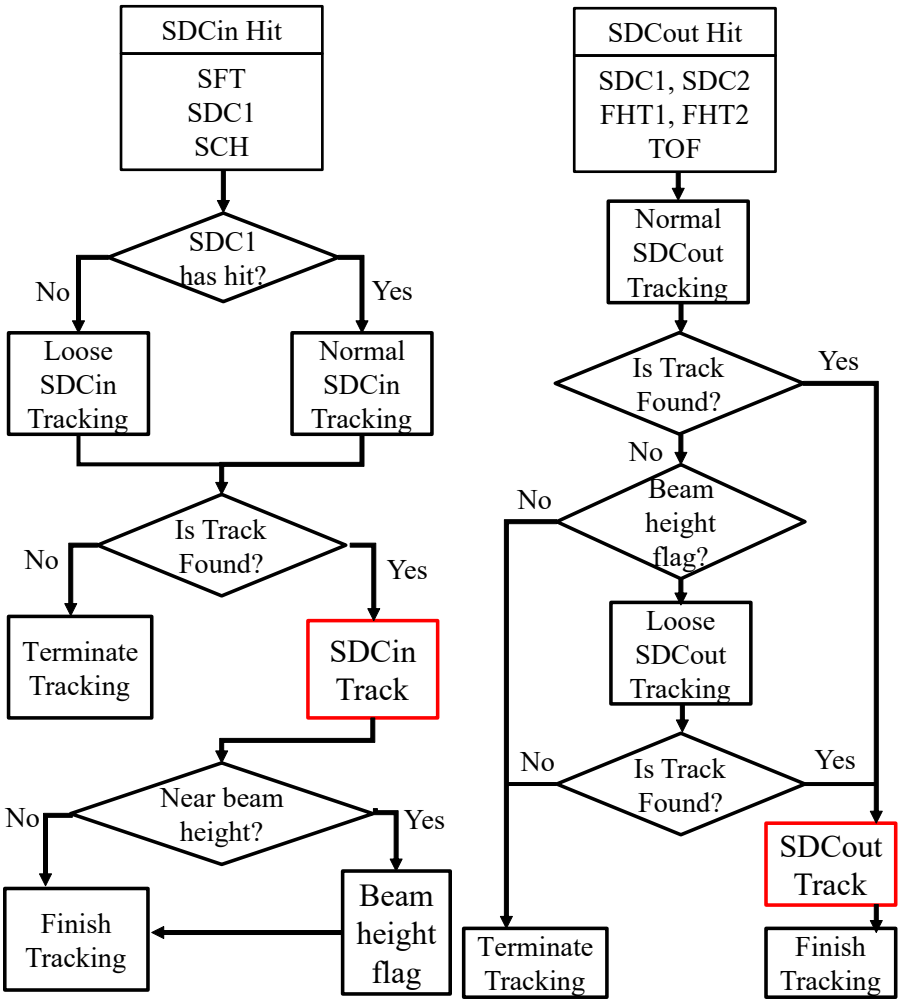

Figure 4.7: Flow of SDCin and SDCout tracking.

4.2.1 SDCin Tracking

SDCin local tracking was performed using hits of SFT, SDC1, and SCH. The specifications of each layer were summarized in Table 4.1. SDC1 was placed apart from the beam axis and insensitive to particles near the beam spot. In addition to "normal tracking" similar to BCout Tracking, "loose tracking" without straight line fitting was additionally performed.

Normal SDCin Tracking

When particles hit SDC1, the straight line fitting like BCout tracking can be performed. Because SDC1 wires had honeycomb configuration, electric field around an anode wire had a circular shape. Then, the hit position calculation from drift length needed the track

Table 4.1: Specifications of each layer used for SDCin Tracking.

i	detector	plane	resolution σ_i [mm]	tilt angle α_i [degree]	note
1	SFT	u	0.26	45	
2	SFT	v	0.26	-45	
3	SFT	x	0.18	0	xx' clustered
4-5	SDC1	vv'	0.30	15	
6-7	SDC1	xx'	0.30	0	
8-9	SDC1	uu'	0.30	-15	
10	SCH	x	6	0	scintillator

angle with respect to perpendicular direction to the chamber plane, which was determined by iteration. The reduced chi-square in l-th iteration is described as follows,

$$(\chi^2/\mathrm{ndf})^l = \frac{1}{N_{\mathrm{hit}}-4}\Big(\underbrace{\sum_{i=1,2,3,10} H_i\Big(\frac{X_i - f^l(z_i)}{\sigma_i}\Big)^2}_{\text{for SFT, SCH}} + \underbrace{\sum_{i=4}^{9} H_i\Big(\frac{\cos\theta_i^l(X_i^l - f^l(z_i^l))}{\sigma_i^l}\Big)^2}_{\text{for SDC1}}\Big), \quad (4.3)$$

$$\begin{aligned}
X_i &= sp, \\
f^l(z_i) &= x^l(z_i)\cos\alpha_i + y^l(z_i)\sin\alpha_i, \\
x^l(z_i) &= x_0^l + u_0^l z_i, \\
y^l(z_i) &= y_0^l + v_0^l z_i \\
\theta_i^l &= \arctan\Big(\frac{df_i^l}{dz_i^l}\Big) = \arctan(u_0^l\cos\alpha_i + v_0^l\sin\alpha_i) \\
X_i^l &= \begin{cases} wp_i + dl_i(t_i)\cos\theta_i^{l-1} & (f_i^{l-1} > wp_i) \\ wp_i - dl_i(t_i)\cos\theta_i^{l-1} & (f_i^{l-1} < wp_i) \end{cases} \\
z_i^l &= \begin{cases} wz_i - dl_i(t_i)\sin\theta_i^{l-1} & (f_i^{l-1} > wp_i) \\ wz_i + dl_i(t_i)\sin\theta_i^{l-1} & (f_i^{l-1} < wp_i) \end{cases} \\
H_i &= \begin{cases} 1 & \text{(If a hit of } i\text{-th layer is included in the track candidate)} \\ 0 & \text{(otherwise)} \end{cases} \\
N_{\mathrm{hit}} &= \sum_{i=1}^{10} H_i \geq 5,
\end{aligned}$$

where, parameters to be determined are x_0, y_0, u_0, v_0. θ and wz indicate the track angle and the z position of a hit wire, respectively. sp represents the position of the SFT and SCH hit segment. σ_i is the intrinsic resolution of each plane, which is summarized in Table 4.1. In the first iteration, the θ was set to 0. Iteration was carried out several times until the reduced chi-square value converge, where the difference from the last iteration became less than 1×10^{-3}. The typical reduced chi-square distribution is shown in the left side of Figure 4.8 and the threshold was set to 50.

For the particles near the beam height at SDC2 and SDC3 position, loose SDCout

tracking scheme should be applied. By extending the found track to SDC2 and SDC3 position, whether the particles were near the beam height or not were judged.

Loose SDCin Tracking

SCH and SFT-uv planes were sensitive to both beam and scattered particles whereas beam particles did not hit SDC1 and SFT-x plane. However, scattered particles with small scattering angles could hit SFT-x. Therefore, particles hitting all SFT planes and SCH should be analyzed as a scattered particle. Since the straight line fitting cannot be applied to events with only four layer hits, the mere combination of SCH and SFT hit information was treated as SDCin track. Because of small scattering angles, these particles would be near the beam height at SDC2 and SDC3 position.

4.2.2 SDCout Tracking

SDCout tracking was performed using hits in SDC2, SDC3, FHT1, FHT2 and TOF. The specifications of each layer were summarized in Table 4.2. TOF was regarded as tracking detecter having 2 layers configuration (xy). Because SDC2 and SDC3 had the vertical insensitive areas as explained in Figure 4.6, vertical position information (y) for particles near the beam height could not be measured. Therefore, loose tracking scheme, tracking in a zx-plane, was applied to events where normal tracking could not reconstruct any track and a particle near the beam height was predicted by the SDCin Tracking result.

Table 4.2: Specifications of each layer used for SDCout Tracking.

i	detector	plane	resolution σ_i [mm]	tilt angle α_i [degree]	note
1-2	SDC2	xx'	0.40	0	
3-4	SDC2	yy'	0.40	90	
5-6	SDC3	yy'	0.40	90	
7-8	SDC3	xx'	0.40	0	
9	TOF	x	40.0	0	scintillator
10	TOF	y	20.0	90	scintillator
11-18	FHT1,2	xx'	0.58	0	

Normal SDCout tracking

Firstly, the local straight tracking similar to SDCin normal tracking was performed. Because both of SDC2 and SDC3 had honeycomb-type wire configuration, the tracking was performed according to minimize the chi-square almost same as Equation (4.3).

The typical reduced chi-square distribution is shown in the right side of Figure 4.8. The χ^2/ndf threshold was set to 50 in order to select good tracking events.

Loose SDCout Tracking (straight line tracking in the ZX plane)

When a SDCout normal tracking cannot find any track and a particle near the beam height was predicted by the SDCin Tracking result, the local straight tracking in the ZX plane was performed. ZX plane fit is equivalent to the $y_0 = v_0 = 0$ and $ndf = N_{\rm hit} - 2$ case in equation (4.3). The χ^2/ndf threshold was also set to 50.

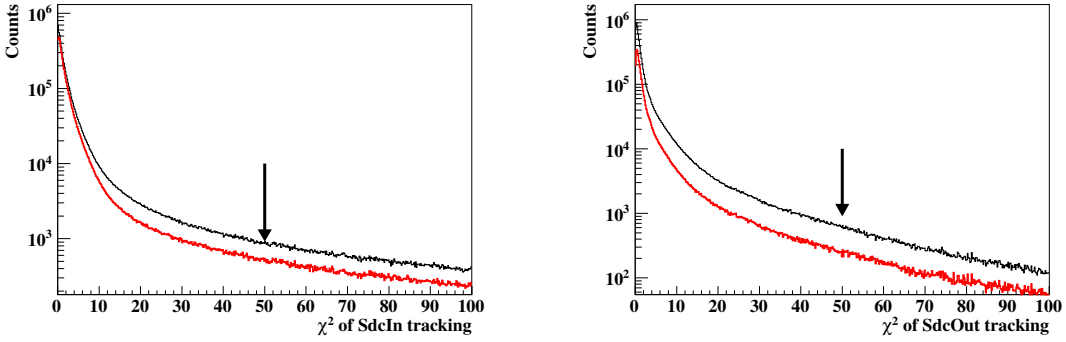

Figure 4.8: Reduced chi-square distribution of SDCin tracking (Left) and SDCout tracking (Right). The black and red lines show the total and single-track events, respectively.

4.2.3 KURAMA Tracking

In order to analyze the momentum of the scattered particle, the trajectories of the outgoing particles in the magnetic field are traced with Runge-Kutta method based on equation of motion. The magnetic field was calculated with ANSYS code [55]. The optimal momentum and trajectory of the outgoing particle were obtained by iterating five parameters (x, y, u, v, p), which represent the momentum vector and the position at TOF. The optimization is performed to reduce the following reduced chi-square as,

$$\chi^2_{\rm KURAMA}/ndf = \frac{1}{N_{\rm hit} - 5} \sum_i H_i \left(\frac{X_i^{\rm hit} - X_i^{\rm track}}{\sigma_i} \right)^2, \tag{4.4}$$

$$H_i = \begin{cases} 1 & \text{(If a hit of } i\text{-th layer is included in the SDCin/SDCout track).} \\ 0 & \text{(otherwise)} \end{cases},$$

$$N_{\rm hit} = \sum_{i=1} H_i,$$

where $X_i^{\rm hit}$ and $X_i^{\rm track}$ are the hit position at a detector and the predicted position of the reconstructed track. The convergence of the iteration was judged by the following criterion, $(\chi^2_{l+1} - \chi^2_l)/\chi^2_l < 10^{-3}$, where χ^2_l represents the result of the l-th iteration. The typical reduced chi-square distribution is shown in the Figure 4.9. The χ^2/ndf threshold was set to 50. About 75 % of triggered events had at least one KURAMA track.

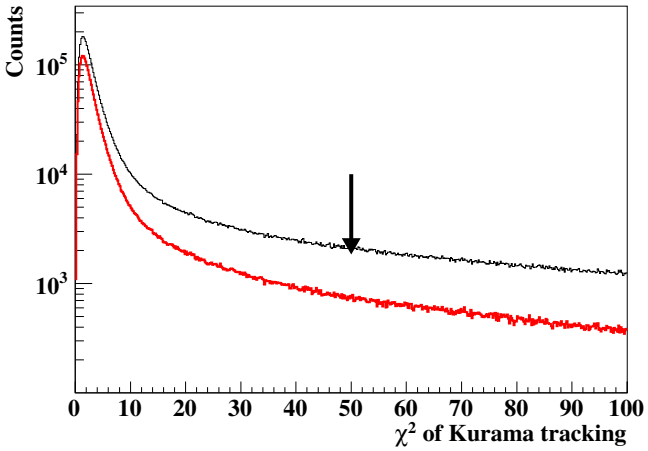

Figure 4.9: Reduced chi-square distribution of KURAMA tracking. The black and red lines show the total and single-track events, respectively.

The momentum resolution of the KURAMA spectrometer was evaluated by the combined analysis of KURAMA and CATCH for the $\pi^+ p$ elastic scattering as describe in Subsection 4.5.2.

4.2.4 K^+ identification

The mass of an outgoing particles was calculated using the KURAMA tracking result and the measured time-of-flight. From the mass, scattered K^+ can be identified. The velocity β of the particle can be calculated using the path length $L_{\rm track}$ of the reconstructed trajectory and the time-of-flight between the target and TOF, t. The mass squared m^2 for each outgoing particle was calculated as;

$$m^2 = \left(\frac{p}{\beta c}\right)^2 (1-\beta^2), \tag{4.5}$$
$$\beta = \frac{L_{\rm track}}{ct}.$$

Figure 4.10 shows the correlation between m^2 and the reconstruct momentum of scattered particles. Basically, K^+ from the $\pi^+ p \to K^+\Sigma^+$ reaction were identified by the m^2 gate as $0.15 < m^2[\mathrm{GeV}^2/c^4] < 0.40$ and the momentum gate as $0.65 < p[\mathrm{GeV}/c] < 1.05$. In the following analysis, the contributions of other reactions with K^+, such as the $\pi^+ p \to K^+\Lambda\pi^+$ reaction, were negligible because momenta of K^+ from these reactions were enough small to be rejected by the matrix trigger (at a trigger level) and the momentum gate. However, there are backgrounds due to the accidental coincidence. In order to reject them, an additional event selection was applied.

Figure 4.11 shows the distributions of m^2 by the different number of BFT clustered hits, which is related to a probability of accidental coincidence. A constant background structure in the m^2 spectrum can be seen between the π^+ and the proton peaks. These background events were caused by the high-intensity π^+ beam. When multiple beam particles including accidental coincidence hit the same segment of BH2 within a shorter

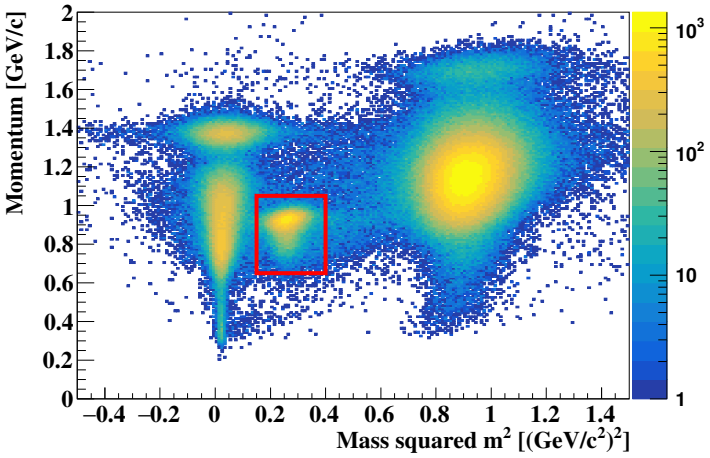

Figure 4.10: Correlation between the squared mass m^2 and the reconstructed momentum of scattered particles. K^+ from the $\pi^+ p \to K^+\Sigma^+$ reaction were identified in the red surrounded region.

time interval than its pulse shape, BH2 sometimes recorded the timing of the accidental particle instead of reacted particle. These fake BH2 timings irrelevant to the reaction results in the miscalculation of time-of-flight and therefore m^2. As shown in the center figure in Figure 4.11, The background can be suppressed for the event with single BFT clustered hit because such a event had low probability to have multiple beam particles. On the other hand, it was enhanced for the BFT multi-cluster events as shown in the right figure in Figure 4.11.

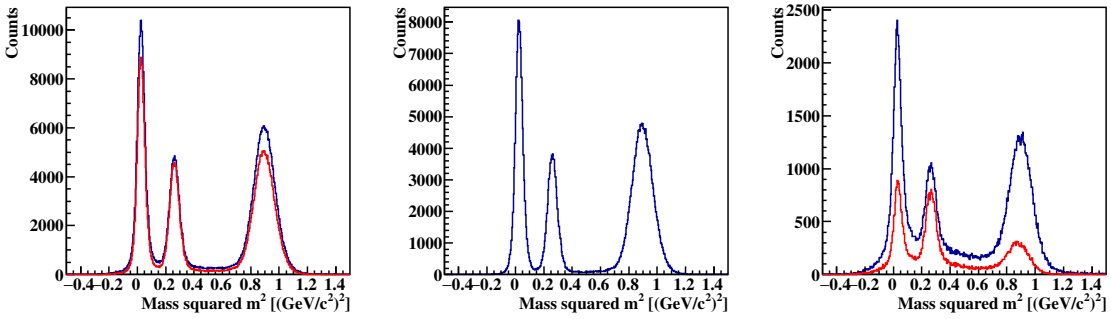

Figure 4.11: Reconstructed mass squared distribution for all events (Left), BFT single cluster events (Center) and BFT multi cluster event(Right). The momentum selection of $0.65 < p[\mathrm{GeV}/c] < 1.05$ was already applied. Blue and red lines represent distributions without and with TOF dE/dx cut, respectively.

The energy loss in TOF was used to select K^+-like events and suppress the constant background. The left side of Figure 4.12 shows the correlation between the momentum and the dE/dx in TOF. The loci corresponding to π^+, K^+ and proton could be seen depending on the difference of the energy deposit in each momentum. Because they

are not completely separate, this TOF dE/dx selection was not applied for BFT single cluster events, where the background contamination was already small. In right side of Figure 4.12, the correlation in the case of BFT multi cluster event with m^2 gate of $0.15 < m^2 < 0.40$, a target of the TOF dE/dx selection, is displayed. There are some events corresponding to proton and π^+ in spite of m^2 gate. These background events were rejected by the TOF dE/dx selection.

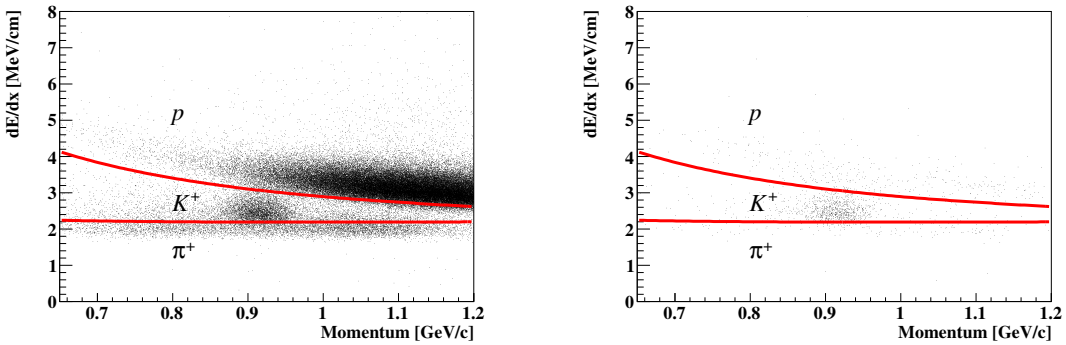

Figure 4.12: Correlation between the momentum and the energy loss in TOF (Left) for all events and (Right) for BFT multi cluster event with m^2 gate of $0.15 < m^2 < 0.40$. The region between two red lines was selected as the K^+ region for the BFT multi cluster event.

The m^2 spectrum after applying the event selection is shown in Figure 4.13. Finally, K^+ was selected from the m^2 gate of $0.15 < m^2[\mathrm{GeV}^2/c^4] < 0.40$, as indicated by the red solid lines in Figure 4.13 with an additional momentum gate of $0.65 < p[\mathrm{GeV}/c] < 1.05$. The background structure was estimated as the shaded spectrum in Figure 4.13 by selecting the non-K^+ region in the TOF dE/dx analysis for multi-beam events. The contamination fraction of the miscalculated events was estimated to be 10.0% for the selected K^+ events.

4.3 Σ^+ identification with (π^+, K^+) analysis

Σ^+ particles were identified from the missing mass spectrum in the $\pi^+ p \to K^+ X$ reaction using the reconstructed momentum of the π^+ beam and the outgoing K^+. Information regarding the vertex of the $\pi^+ p \to K^+ X$ reaction, which was determined as the closest point between the π^+ and K^+ tracks, was additionally used to select the reactions occurring in the LH_2 target.

The left side of Figure 4.14 shows the z-vertex distribution. The LH_2 target can be identified from -200 mm to 150 mm from the vertex image. For the $\Sigma^+ p$ scattering analysis, the $-150 < z[\mathrm{mm}] < 150$ region shown with the red dotted lines in the left side of Figure 4.14 was selected, considering CATCH acceptance. The right side of Figure 4.14 shows the correlation between the x- and y-vertices. In this plot, the detection of two protons with CATCH was required to enhance the background events, owing to interactions between the π^+ beam and the target vessel. A horizontally wider beam caused such background events. x- and y-vertices are required within the red line in the right

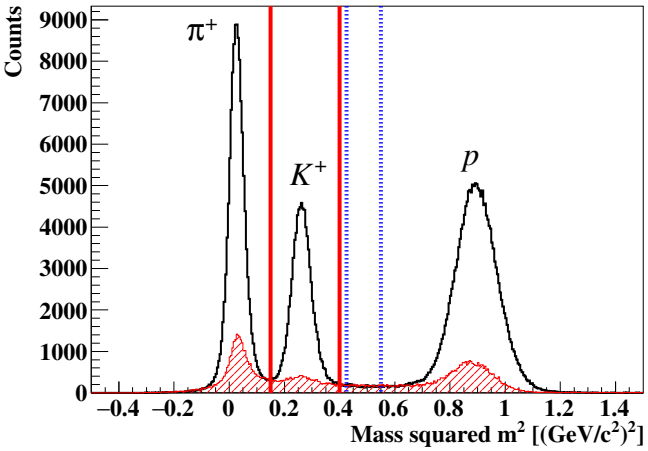

Figure 4.13: Reconstructed m^2 distribution after applying the event selection to reject background contamination. The red shaded spectrum shows the estimated background due to the miscalculated time-of-flight for multi-beam events. The K^+ and side-band regions are indicated by the red solid and blue dashed lines, respectively. The side-band region was used to estimate the contribution of the miscalculated events in further analyses.

side of Figure 4.14 to suppress the backgrounds. The vertex resolution of the spectrometers was evaluated using multi-particle events, such as the $\pi^+ p \to \pi^+\pi^+\pi^- p$ reaction, by comparing the vertex obtained from the spectrometer analysis with that obtained from the two other tracks measured by CATCH from the same reaction vertex, as described in Subsection 4.5.1. The z-vertex resolution depends on the scattering angle θ_{K^+}, and typical resolutions are $\sigma_z = 16$ mm and 10 mm for $\theta_{K^+} = 10°$ and 20°, respectively. The x- and y-vertex resolutions were evaluated as $\sigma_x = 2.6$ mm and $\sigma_y = 3.5$ mm, respectively, with a negligibly small angular dependence. These vertex resolutions were considered in the simulation study to estimate the analysis cut efficiency.

The missing mass and missing momentum of the $\pi^+ p \to K^+ X$ reaction were calculated as

$$M_X = \sqrt{(E_\pi^{\rm tot} + m_p - E_K^{\rm tot})^2 - (\boldsymbol{p}_\pi - \boldsymbol{p}_K)^2}, \tag{4.6}$$

$$\boldsymbol{p}_X = \boldsymbol{p}_\pi - \boldsymbol{p}_K, \tag{4.7}$$

where $E_\pi^{\rm tot} = \sqrt{m_\pi^2 + p_\pi^2}$ and $E_K^{\rm tot} = \sqrt{m_K^2 + p_K^2}$ are total energies of π^+ and K^+, respectively. The missing mass spectrum of the $\pi^+ p \to K^+ X$ reaction is shown in Figure 4.15. A clear peak corresponding to Σ^+ was identified. As mentioned in the previous subsection, there were misidentification backgrounds in the K^+ selection owing to multiple beam events. Their contribution was examined by selecting the sideband region of K^+, as shown by the blue dashed lines in Figure 4.13 with a momentum gate of $0.65 < p[\mathrm{GeV}/c] < 1.05$. The red shaded histogram in Figure 4.15 shows the missing mass spectrum for the side-band contribution. We selected Σ^+ particles from 1.15 to 1.25 GeV/c^2, as shown by the arrows in Figure 4.15. Contamination was estimated to be 8.6% for Σ^+ selection. In total, 4.9 $\times 10^7$ Σ^+ particles were accumulated after subtracting the contamination.

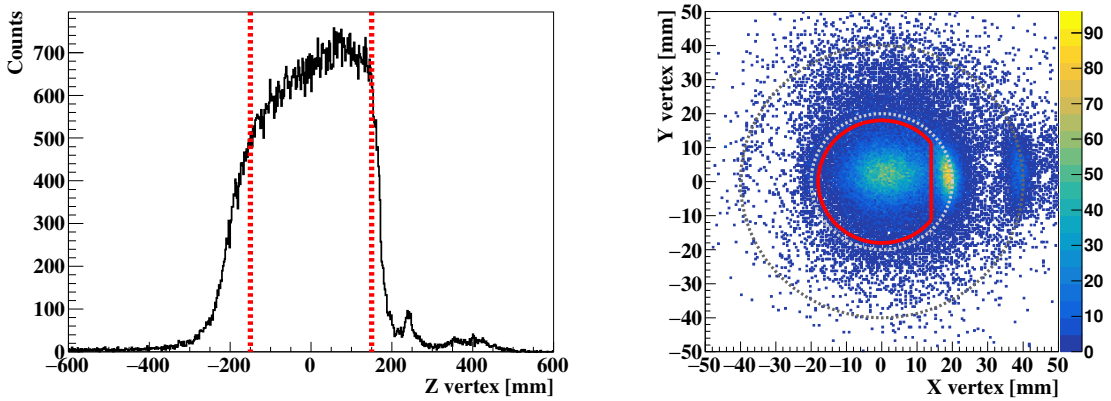

Figure 4.14: Vertex distributions of the (π^+, K^+) reaction. (Left) z-vertex distribution. (Right) Correlation between the x- and y-vertices for events in which two protons were detected with CATCH. The gray dotted lines show the envelopes of the target container and vacuum window. The events inside the red-line region were selected to suppress the contamination of the reaction at the target container.

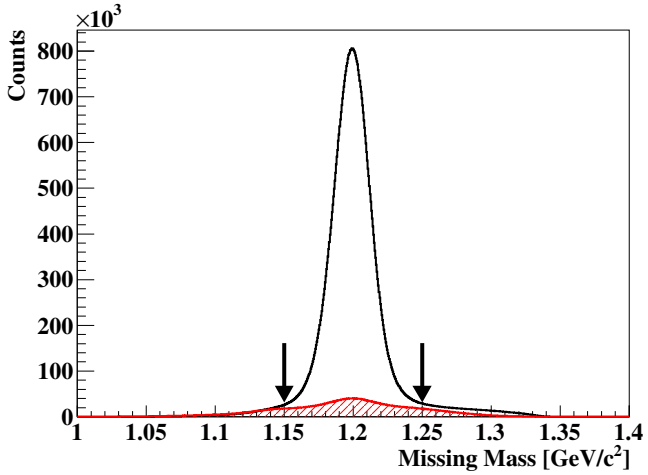

Figure 4.15: Missing mass spectrum of the $\pi^+ p \to K^+ X$ reaction for the K^+ events (black open histogram) and side-band events of K^+ (red shaded histogram) to estimate the effect of the contamination of the miscalculated events under the K^+ region in the m^2 spectrum. Σ^+ events were selected by the $1.15 < M_X[\mathrm{GeV}/c^2] < 1.25$ gate, represented by the arrows.

The reconstructed Σ^+ momentum, as the missing momentum of the $\pi^+ p \to K^+ X$ reaction, is shown in Figure 4.16. This ranges from 0.44 to 0.85 GeV/c. In the $\Sigma^+ p$ scattering analysis, the Σ^+ events were categorized into three momentum ranges: the low- ($0.44 < p_\Sigma[\mathrm{GeV}/c] < 0.55$), middle- ($0.55 < p_\Sigma[\mathrm{GeV}/c] < 0.65$), and high-momentum ($0.65 < p_\Sigma[\mathrm{GeV}/c] < 0.80$) regions. The resolution of the Σ^+ momentum was 6×10^{-3} GeV/c in σ, which was determined predominantly by the momentum resolution of the KURAMA

spectrometer.

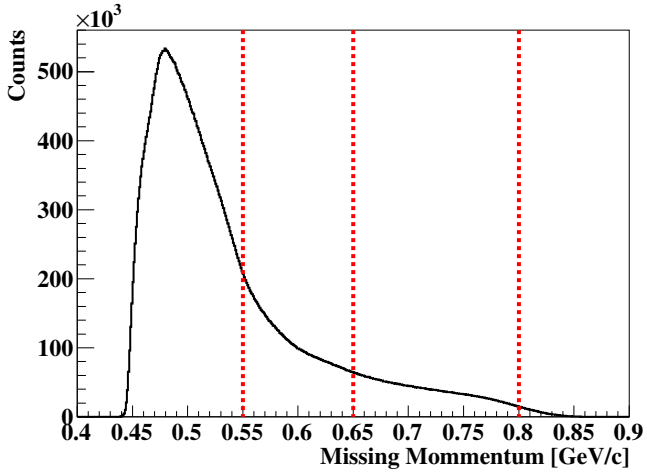

Figure 4.16: Σ^+ momentum reconstructed as the missing momentum of the $\pi^+ p \to K^+\Sigma^+$ reaction. The red dotted lines show the boundaries of the three momentum regions: low- ($0.44 < p_\Sigma[\mathrm{GeV}/c] < 0.55$), middle- ($0.55 < p_\Sigma[\mathrm{GeV}/c] < 0.65$), and high-momentum ($0.65 < p_\Sigma[\mathrm{GeV}/c] < 0.80$) regions.

4.4 CATCH for the recoil/decay protons

4.4.1 Outline

The charged particles involved in the $\Sigma^+ p$ scattering, that is, the recoil proton and decay product of Σ^+, were detected using CATCH. The trajectory was reconstructed using CFT. The kinetic energy was measured by summing the energy deposits in CFT (dE_{CFT}) and BGO (E_{BGO}) along the trajectory. The measured energy is denoted as E_{meas}. Particle identification in CATCH was performed using the so-called dE-E method between dE_{CFT}, corrected by the path length in CFT (dE/dx), and E_{meas} for each track. In this way, four momentum vectors for protons were determined.

4.4.2 CFT Tracking

First of all, trajectories of charged particles were reconstructed using CFT. CFT has the four ϕ layers in which fibers are arranged parallel to the beam axis (described as Z axis) and the four uv layers in which the fibers are set in a spiral shape, as shown in Figure 4.17. In the following, the coordinate axes are defined as Figure 4.17 for the cylindrical shape of CFT. In order to reconstruct three-dimensional trajectories with CFT, two stages of tracking were performed. The first and second stages are called "ϕ tracking" and "uv tracking", respectively.

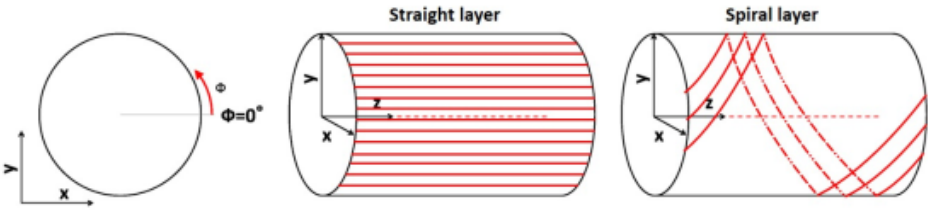

Figure 4.17: Structures of fiber arrangement for the straight and spiral layers of CFT and the definition of the coordinates[39].

ϕ tracking

From the hit segment of i-th ϕ plane, the x and y coordinate of the hit position (X_i, Y_i) can be calculated as,

$$X_i = r_i \cos\phi_i, \quad Y_i = r_i \sin\phi_i,$$

where r_i is the designed radius of the i-th plane and ϕ_i is determined from the hit segment of i-th layer. Using these information, the straight line tracking in the xy plane was performed with hit positions of ϕ layers to minimize the reduced chi-square as follows,

$$\chi^2/\mathrm{ndf} = \frac{1}{N_{\mathrm{hit}} - 2} \sum_{i=1}^{4} H_i \Big(\frac{Y_i(r_i, \phi_i) - (AX_i(r_i, \phi_i) + B)}{\sigma_i} \Big)^2, \tag{4.8}$$

$$H_i = \begin{cases} 1 & \text{(If a hit of } i\text{-th } \phi \text{ layers is included in the track candidate)} \\ 0 & \text{(otherwise)} \end{cases},$$

$$N_{\mathrm{hit}} = \sum_{i=1}^{4} H_i \geq 3,$$

where, A and B are the parameters to optimize the straight line in xy plane. If the hit positions are close to y axis, X_i and Y_i in the equation (4.8) are inverted. Although similar inversion is actually considered in the uv tracking, treatment of only one configuration, $y = Ax + B$ and $x = u_0 z + x_0$ case, is simply described in the following. σ_i is the intrinsic resolution of each plane, typically 260 μm. Using the result of ϕ tracking, the ϕ-coordinate of the hit position of the j-th uv plane, ϕ_j can be calculated from the coordinate of intersection point (X_j, Y_j) between the circle $x^2 + y^2 = r_j^2$ and half straight line $y = Ax + B$.

uv tracking

A given segment of the j-th layer of the uv layers was on a straight line in the side plane of a cylinder, $z\phi$-plane as shown in Figure 4.18.

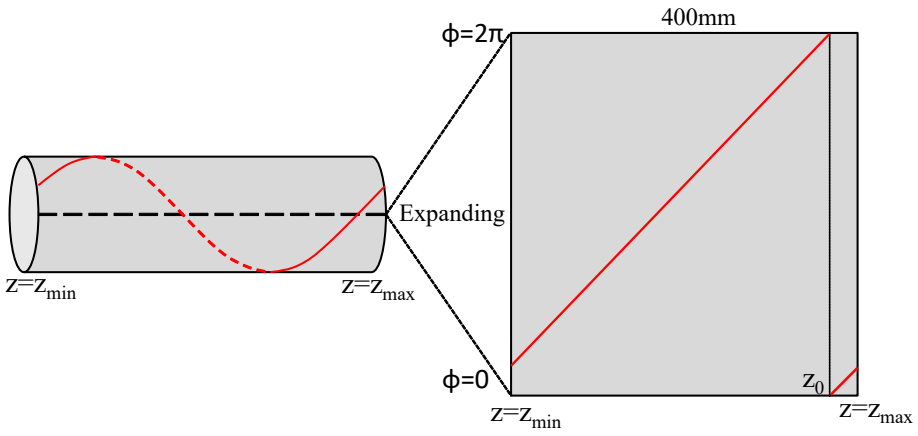

Figure 4.18: Schematic drawing of a fiber in the CFT uv layer. It is on a straight line in the $z\phi$-plane, which is sideplane of a cylinder.

For example, in the case of u plane, the z position is expressed as follows;

$$z_{j,\mathrm{seg}}(\phi) = \begin{cases} \frac{400}{2\pi}\phi + z_{0,j,\mathrm{seg}} & \left(0 \leq \phi < 2\pi \cdot \frac{z_{\max} - z_{0,j,\mathrm{seg}}}{400}\right) \\ \frac{400}{2\pi}(\phi - 2\pi) + z_{0,j,\mathrm{seg}} & \left(2\pi \cdot \frac{z_{\max} - z_{0,j,\mathrm{seg}}}{400} \leq \phi < 2\pi\right), \end{cases}$$

where $z_{\max}$ represents the z-coordinate of the far end point of CFT and $z_{0,j,\mathrm{seg}}$ is the ϕ-intersect of the straight line. The straight line tracking in xz plane was performed with hit positions of uv layers and ϕ_j calculated using the result of the ϕ tracking to minimize the reduced chi-square as follows,

$$\chi^2/\mathrm{ndf} = \frac{1}{N_{\mathrm{hit}} - 2} \sum_{j=1}^{4} H_j \left(\frac{X_j(r_j) - (u_0 z_j(\phi_j) + x_0)}{\sigma_j} \right)^2, \tag{4.9}$$

$$H_j = \begin{cases} 1 & (\text{If a hit of } j\text{-th } uv \text{ layers is included in the track candidate}) \\ 0 & (\text{otherwise}) \end{cases},$$

$$N_{\mathrm{hit}} = \sum_{j=1}^{4} H_j \geq 3,$$

where, x_0 and u_0 are the parameters. The vertical position at $z = 0$, y_0, and angle, v_0, of the track can be expressed as $y_0 = Ax_0 + B, v_0 = Au_0$. In this way, the straight line in the three-dimensional space

$$\frac{x - x_0}{u_0} = \frac{y - y_0}{v_0} = z$$

was reconstructed.

Correction of fiber positions

The positions of CFT fibers were slightly deviated from the design positions due to the working accuracy of fabrication. The deviations of fibers, $d\phi(z), dr(z)$ for ϕ layer and $dz(\phi)$ and $dr(\phi)$ for uv layer, were estimated from the cosmic ray data by comparing the

designed position with the reconstructed position from the tracking. Because a cosmic ray crossed CFT and hit $8 \times 2 = 16$ layers, the accuracy of the position estimation at each layer was improved from the normal tracking with eight layers. The typical distributions of $d\phi(z)$ and $dz(\phi)$ are shown in Figure 4.19. Figure 4.20 show those of $dr(z)$ and $dr(\phi)$.

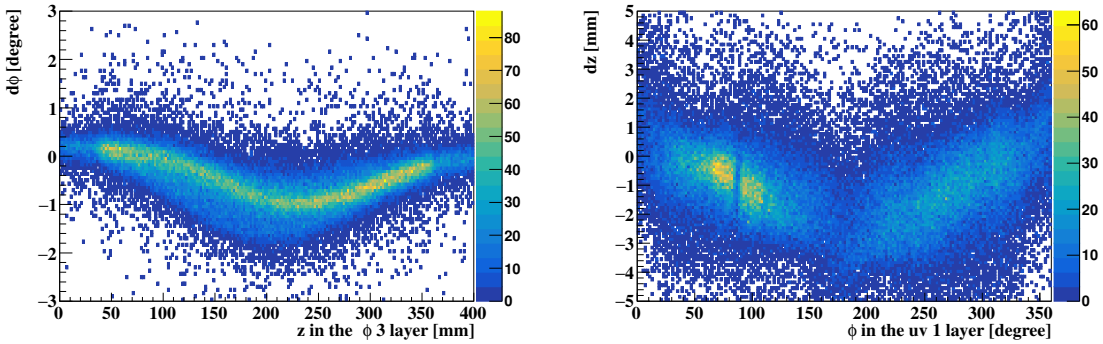

Figure 4.19: Distributions of the fiber position deviation $d\phi(z)$ in the CFT $\phi 3$ layer (Left) and $dz(\phi)$ in the CFT $uv1$ layer (Right). $d\phi(z)$ were corrected by 5th-order polynomial of z and $dz(\phi)$ were corrected by 1st-order polynomial of ϕ. The parameters of $dz(\phi)$ correction were determined for each of $\phi = 10°$ section.

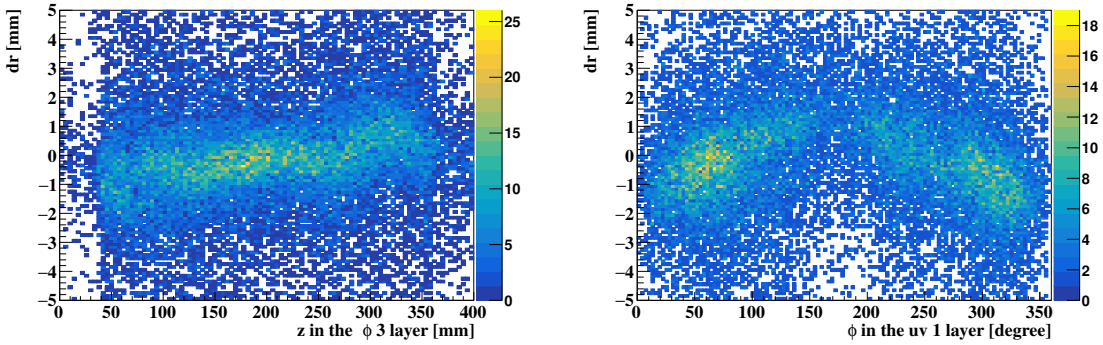

Figure 4.20: Distributions of the fiber position deviation $dr(z)$ in the CFT $\phi 3$ layer (Left) and $dr(\phi)$ in the CFT $uv3$ layer (Right). $dr(z)$ were corrected by 5th-order polynomial of z and $dr(\phi)$ were corrected by 1st-order polynomial of ϕ. The parameters of $dr(\phi)$ correction were determined for each of $\phi = 10°$ section.

Tracking with position correction was performed following "1st tracking", tracking without correction, by replacing $r_i \mapsto r_i + dr_i(z_{i,1\mathrm{st}})$ and $\phi_i \mapsto \phi_i + d\phi_i(z_{i,1\mathrm{st}})$ in the equation (4.8), where $z_{i,1\mathrm{st}}$ means the z position of i-th ϕ layer hit calculated from the result of the 1st tracking. Using the result of 2nd ϕ tracking, 2nd uv tracking was performed by replacing $X_j(r_j) \mapsto X_{j,2\mathrm{nd}}(r_j + dr_j(\phi_{j,2\mathrm{nd}}))$ and $z_j(\phi_j) \mapsto z_j(\phi_{j,2\mathrm{nd}}) + dz_j(\phi_{j,2\mathrm{nd}})$ in the equation (4.9). The typical reduced chi-square distributions of ϕ tracking and uv tracking are shown in Figure 4.21. The distribution became closer to natural χ^2 distribution after the position correction.

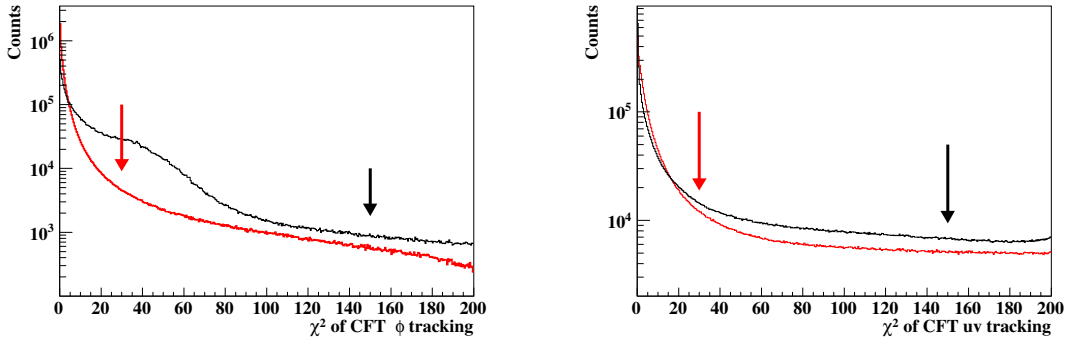

Figure 4.21: Reduced chi-square distribution of CFT-ϕ tracking (Left) and CFT-uv tracking (Right). The black and red lines show the result of the 1st and 2nd tracking, respectively. The thresholds were set to 150 for the 1st tracking and 30 for the 2nd tracking.

Angular resolution of CFT tracking

The angular resolution of CFT tracking was evaluated using the pp elastic scattering data with proton beam. In the pp elastic scattering, opening angle of two proton $\theta_{\rm lab}$ is 90° in the non-relativistic limit. The actual $\theta_{\rm lab}$ is slightly smaller than 90° owing to relativistic effect. Figure 4.22 shows the opening angle between two protons for pp scattering with the beam momentum of 0.6 GeV/c. Because the spread of $\theta_1 + \theta_2$ ($\sigma_{\theta_1+\theta_2}$) was expressed as $\sigma_{\theta_1+\theta_2} = \sqrt{2}\sigma_\theta$, angular resolution of CFT tracking σ_θ was estimated to be 1.5 degrees. This angular resolution of CFT was taken into account in the simulation for $\Sigma^+ p$ scattering.

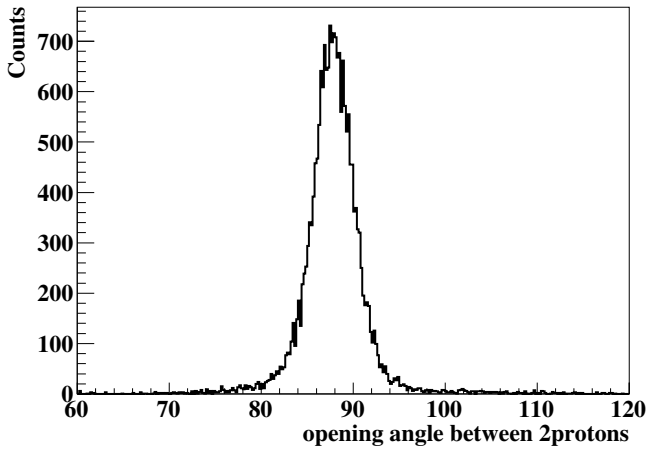

Figure 4.22: Opening angle between two protons for pp scattering with the beam momentum of 0.6 GeV/c.

The vertex resolutions of the CFT tracking were also studied by reconstructing the target container image from the crossing point between two tracks measured by CATCH. The x and z distributions of the crossing point are shown in Figure 4.23. The z vertex

resolution was evaluated to be 2.7 mm and the x and y vertex resolutions were assumed to be same with the detector structure and evaluated to be 2.1 mm.

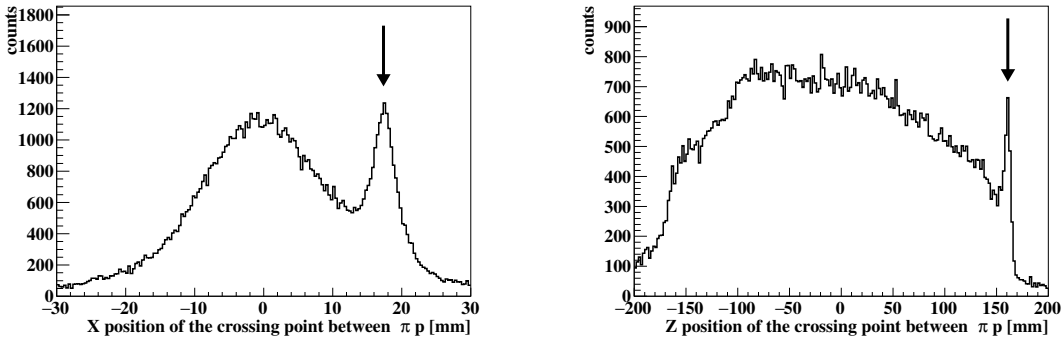

Figure 4.23: x (Left) and z (Right) position distributions of the crossing point between two tracks detected with CATCH. The arrow in left figure indicates the target vessel and the one in right figure indicates the edge of the target.

4.4.3 Energy measurement with CFT and BGO

For each reconstructed CFT track, the information on fiber hits included in the track was recorded. Measured energies with BGO segments near the CFT track were also added to the CFT track. By summing up the energy deposits measured in the fibers and BGO segments along the track, the measured energy deposits of the charged particle was calculated.

Energy calibration of BGO

Each BGO crystal equipped with a PMT. The waveform data of the shaped signal with an integral circuit were recorded using a flash ADC with a sampling frequency of 33 MHz. The pulse height and the timing of each waveform were obtained through the template fitting method.

BGO energy calibration was performed with the pp elastic scattering data using 0.6 GeV/c proton beam. The energy of scattered protons has a one-to-one correlation with the scattering angle θ because the pp elastic scatterings are two-body reactions. However, there were the target vessel and CFT before the BGO calorimeter. This effect was considered by the passage simulator based on Geant4 package [53] described in Section 3.2. The relation between the BGO pulse height and the energy deposit in BGO was obtained by comparing the measured pulse height to the simulated energy deposit for the same scattering angle θ, shown in Figure 4.24. The obtained correlation was fitted with a phenomenological relation [56] between the photon yield and the energy deposit expressed by the following equation

$$PH_{\mathrm{BGO}} = a \times E - b \times \log\Big(\frac{E+b}{b}\Big), \tag{4.10}$$

where a and b are the parameters and PH and E correspond to the pulse height and the energy deposit in the BGO calorimeter, respectively. The fitted calibration curve is

shown in Figure 4.25. The BGO energy calibration was performed for all BGO segments using this method.

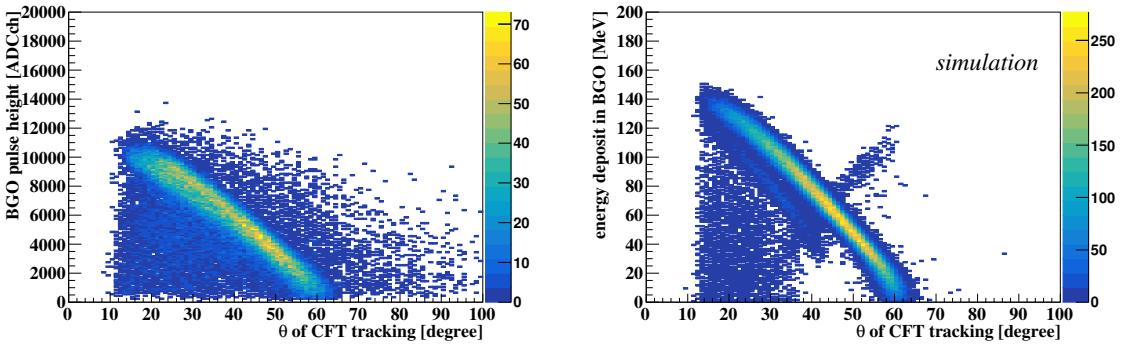

Figure 4.24: Angular dependences of the pulse height in the data (Left) and the simulated energy deposit (Right) in the BGO calorimeter for the *pp* scattering events caused by 0.6 GeV/c proton beam.

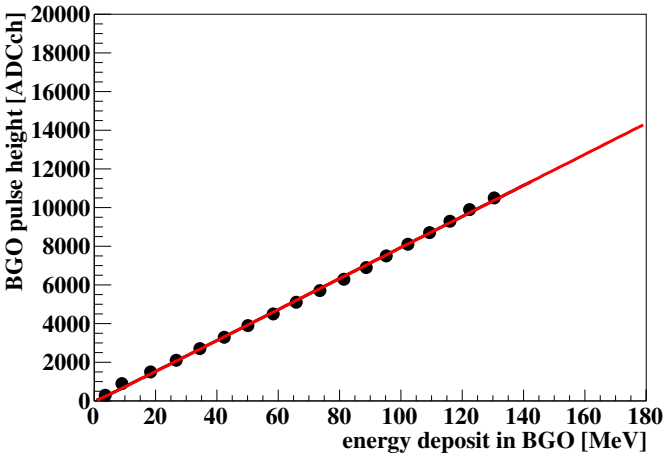

Figure 4.25: Energy calibration curve for BGO calorimeter.

Energy calibration of CFT

For each MPPC attached to a scintillating fiber in CFT, the information on the pulse height was recorded by peak-hold ADC in VME-EASIROC modules. These ADC values were normalized layer by layer using *pp* scattering data. The CFT energy calibration from the normalized ADC values to the energy deposit was performed using the recoil proton from the $\pi^+ p$ elastic scattering with 1.41 GeV/c π^+ beam. Owing to the higher beam momentum, the energy range of the recoil proton from the $\pi^+ p$ elastic scattering was wider than that from the *pp* elastic scattering data. The energy calibration procedure for CFT was similar to one for BGO. The relation between the normalized CFT ADC value and the energy deposit in CFT fiber was obtained by comparing the ADC value to

the simulated energy deposit for the same BGO energy loss shown in Figure 4.26. The obtained correlation was fitted with a function as;

$$\mathrm{PH_{CFT}} = a\Big\{1 - \exp\Big(\frac{-b \times dE}{a}\Big)\Big\}, \tag{4.11}$$

where , a and b are the parameters corresponding to the effective pixel numbers of MPPC and photon numbers per energy deposit. By this parametrization, the saturation effect of the MPPC is taken into account. The fitted calibration curve is shown in Figure 4.27.

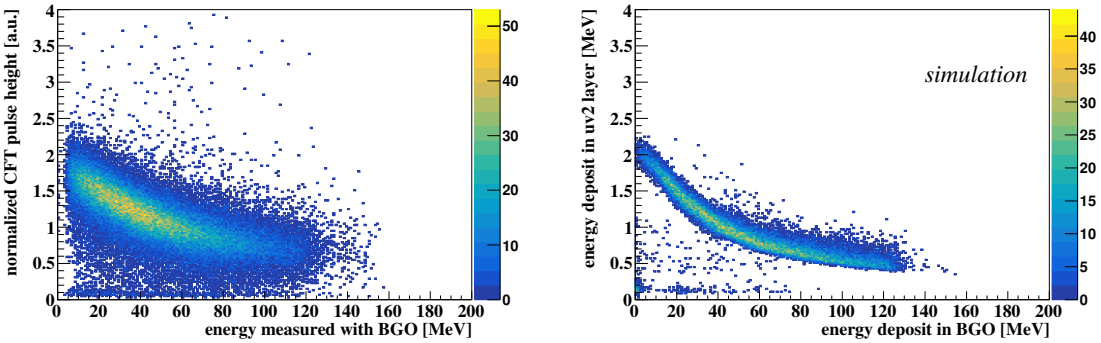

Figure 4.26: BGO energy dependences of the pulse height (Left) and the simulated energy deposit in the CFT fiber (Right) for the $\pi^+ p$ elastic scattering events caused by 1.41 GeV/c π^+ beam. The protons with the moderate kinetic energy were selected by $55 < \theta < 80$ gate.

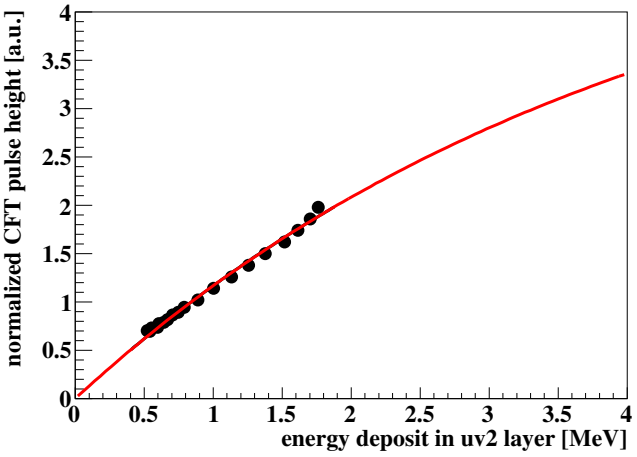

Figure 4.27: Energy calibration function of CFT fiber for the 2nd uv layer

Energy resolution of CATCH

The energy resolution of the summed energy deposit in CFT and BGO, was evaluated from the pp elastic scattering data. For each proton track, the energy of the recoil proton can

be calculated from the scattering angle θ obtained by CFT tracking. In this calculation, the effect of the energy loss in the LH_2 target is considered by Bethe-Bloch's formula. The calculated kinetic energy of the recoil proton is defined as $E_{\rm cal}(\theta)$. The kinematical consistency ΔE for the pp scattering is defined as

$$\Delta E(pp \text{ scattering with } p \text{ beam}) = E_{\rm meas} - E_{\rm cal}(\theta), \tag{4.12}$$

$$E_{\rm cal}(\theta) = \frac{2m_p p_p^2 \cos^2\theta}{(E_p^{\rm tot} + m_p)^2 - p_p^2 \cos^2\theta}, \tag{4.13}$$

where $E_{\rm meas}$ is the measured energy deposit with CFT and BGO. p_p and $E_p^{\rm tot} = \sqrt{m_p^2 + p_p^2}$ is the momentum and total energy of the beam proton. The spread of ΔE was the energy resolution of CATCH including the energy resolutions of CFT and BGO, the angular resolution of CFT tracking, and the fluctuation of the energy loss in the target. Figure 4.28 shows the ΔE distribution at $E_{\rm cal} = 100$ MeV. At this point, $\sigma_E \sim 6$ MeV and energy dependence of the energy resolution was small. This energy resolution of CATCH was taken into account in the simulation for the $\Sigma^+ p$ scattering.

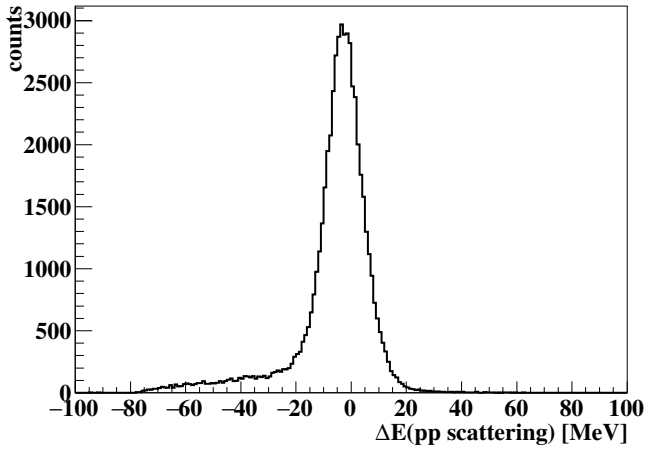

Figure 4.28: ΔE distribution of the pp scattering at $E_{\rm cal}(\theta) = 100$ MeV.

4.4.4 Particle identification

Particle identification in CATCH was performed by using the so-called dE-E method between $dE_{\rm CFT}$, corrected by the path length in CFT (dE/dx), and $E_{\rm meas}$ for each track. Figure 4.29 shows the dE-E plot for the Σ^+ production events. The locus defined by the two lines corresponds to the protons. The typical purity of a proton was 90% for the selection gate. The other locus shows an approximately constant dE/dx distribution with a branch toward the higher dE/dx value mainly corresponding to π^+s. Most of π^+s penetrated BGO by losing only a part of the kinetic energy. Therefore, the only available information for π^+ is the tracking information.

Low-energy protons, which stopped in CFT before reaching to BGO, were also identified by setting a dE/dx value larger than 2.7 MeV/mm in CFT. These protons were also used for the $\Sigma^+ p$ scattering analysis.

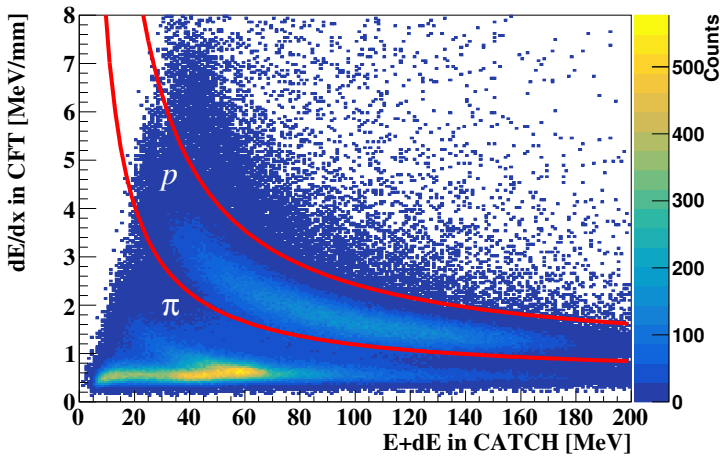

Figure 4.29: *dE-E* correlation between the energy loss in CFT and summed energy deposit in CATCH. The two red lines show the selection region for protons.

4.5 Evaluations of the system specification by combined analysis

The combination of the spectrometer system and CATCH enables detailed analysis of complex reactions. These reactions can be used for evaluations for the position and momentum resolution of the spectrometers. Additionally, a detection probability for an accidental proton was estimated.

4.5.1 The vertex resolution evaluation of the spectrometer system using the $\pi^+ p \to \pi^+\pi^+\pi^- p$ reaction

An event display of the $\pi^+ p \to \pi^+\pi^+\pi^- p$ reaction is shown in Figure 4.30. For such a reaction, the multi track can be reconstructed with CATCH in addition to the incident π^+ beam and the outgoing $\pi^\pm$ or proton analyzed with the spectrometers.

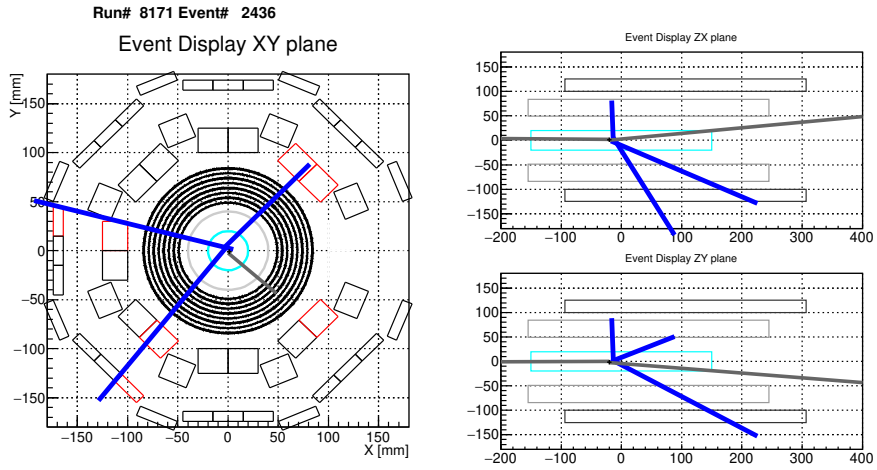

Figure 4.30: Event display of the $\pi^+ p \to \pi^+\pi^+\pi^- p$ reaction, which is reconstructed using track information from the spectrometers and CATCH. The pion-like tracks reconstructed with CATCH are indicated by the blue lines and the incident π^+ and the outgoing proton are indicated by the gray lines.

The $\pi^+ p \to \pi^+\pi^+\pi^- p$ reaction events were selected by the cut condition requiring detections of both a proton with the KURAMA spectrometer and two pions with CATCH or one pion with the KURAMA spectrometer and one proton and pion with CATCH. The vertex resolutions of the spectrometer system can be evaluated by comparing the reaction vertices reconstructed with the spectrometer system and CATCH because the vertex resolutions of CATCH were comparable to or better than one of the spectrometer system. The z vertex resolution depended on the scattering angle as shown in Figure 4.31. The x and y vertex resolutions were evaluated as $\sigma_x = 2.6$ mm and $\sigma_y = 3.5$ mm and the angular dependences were negligible.

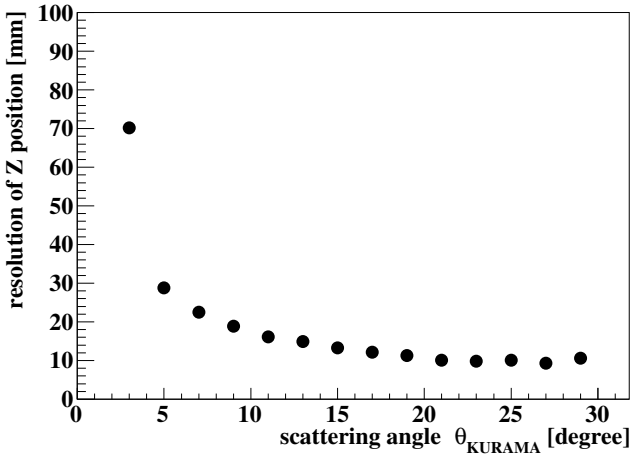

Figure 4.31: z position resolution of the spectrometer system as a function of scattering angle.

4.5.2 The momentum resolution evaluation of KURAMA using the π^+p elastic scattering

In the past experiments at the J-PARC K1.8 beam line, the momentum resolution evaluations of the spectrometers for scattered particle, the KURAMA and previous SKS spectrometer, were performed with empty target data. However, the LH_2 target and CATCH used in the J-PARC E40 experiment cannot be moved easily. Therefore, the evaluation of the momentum resolution of KURAMA was performed using the π^+p elastic scattering kinematics. In this analysis, detection of the recoil proton with CATCH and the scattered π^+ with the KURAMA spectrometer was required. From the scattering angle of the proton measured with CFT, the momentum of scattered π^+, $p_{\pi\mathrm{cal}}$, can be calculated. The kinematical consistency Δp for the π^+p scattering is defined as

$$\Delta p = p_{\mathrm{KURAMA}} - p_{\pi\mathrm{cal}}, \tag{4.14}$$

where p_{KURAMA} is the momentum obtained by KURAMA tracking. The $\Delta p/p$ distribution is shown in Figure 4.32. The spread of blue histogram corresponds to the momentum resolution of the KURAMA tracking. It was evaluated as $\sigma_p/p = 2.5 \times 10^{-2}$ for 1.37 GeV/c π^+.

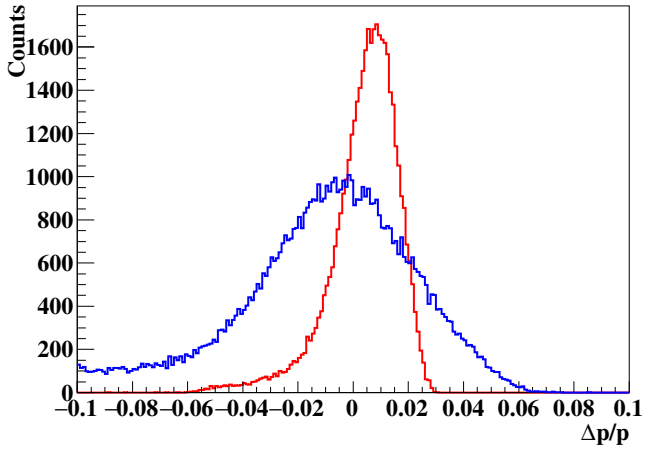

Figure 4.32: $\Delta p/p$ distribution for the momentum resolution evaluation for 1.37 GeV/c π^+. The spread of blue histogram corresponds to the momentum resolution of the KURAMA tracking. In the red histogram, p_{KURAMA} was calculated from the scattering angle θ_{KURAMA} and the momentum resolution was improved, although the angular resolution of approximately 1° deteriorates the momentum resolution.

Once particle identification for the outgoing particle was performed and the two body reaction was determined, the momentum of the outgoing particle can be calculated from the scattering angle θ_{KURAMA}. By applying this analysis method, the momentum resolution was improved as shown by the red histogram in Figure 4.32. After the contribution of the angular resolution of approximately 1° was subtracted, the momentum resolution was evaluated to be $\sigma_p/p = 6.5 \times 10^{-3}$ for 1.37 GeV/c π^+ . In the analysis of the $\pi^+p \to K^+\Sigma^+$ reaction, the momentum of K^+ was calculated from the scattering angle θ_{K^+}.

4.5.3 The detection probability estimation for accidental proton by CATCH

In the $\pi^+ + p$ reactions induced by 1.41 GeV/c π^+ beam, the inelastic scattering with $p\bar{p}$ production are not allowed in terms of energy. If the outgoing proton was detected with the KURAMA spectrometer, ideally CATCH could not detect the protons. Thus, the detection probability of an accidental proton with CATCH can be estimated by events in which detection of both a proton from π^+p scattering with KURAMA and another proton with CATCH were required. It was about 2% and the distributions of energy and the angle of such protons shown in Figure 4.33 were also obtained. The energy and the scattering angle of about 40 % the accidental protons were consistent with the kinematics of the π^+p elastic scattering. These protons were derived from the π^+p elastic scattering caused by the accidental π^+ beam. The rest of accidental proton were from the reaction between the target vessel and the accidental π^+ beam. The probability of accidental coincidence and the energy and angle distributions of accidental proton were taken into account in the simulation study to estimate the background of the Σ^+p scattering events.

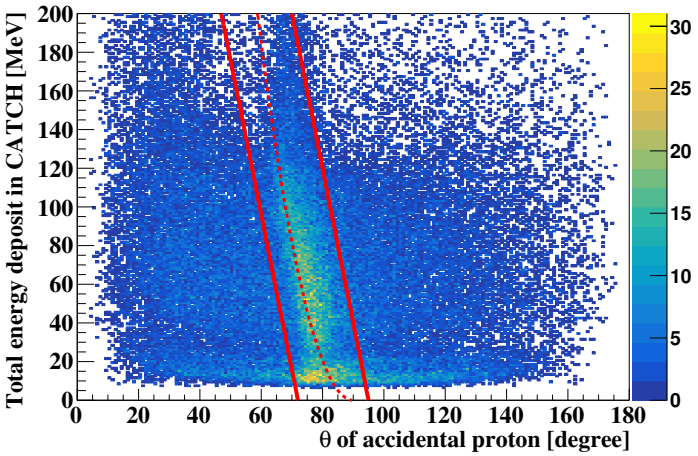

Figure 4.33: Correlation of the accidental proton's energy and scattering angle. The red dotted curve corresponds to the kinematics of the π^+p elastic scattering. Protons in the region inside red lines were derived from the π^+p elastic scattering caused by the accidental π^+ beam.

Chapter 5

Analysis-II:Identification of the $\Sigma^+ p$ scattering events

5.1 Outline

As explained in Section 4, the momentum vector of the incident Σ^+ is reconstructed from the spectrometer information. In addition, the momentum vector of the recoil proton was measured using CATCH. Combining these momentum vectors enables us to identify the $\Sigma^+ p$ scattering events by checking the kinematical consistency of the recoil proton between the measured energy $E_{\rm meas}$ and the calculated energy $E_{\rm cal}$ from the recoil angle. This section describes the analysis of the event identification method by kinematical consistency check, especially for $\Sigma^+ p$ identification, and background suppression and derivation of the numbers of scattering events.

5.2 Kinematical consistency check method

A particular reaction involving Σ^+ was identified by kinematical consistency check method. In this procedure, a reaction to be analyzed was assumed. Under assumption that the reaction occurred, the kinetic energy $E_{\rm cal}$, or momentum $p_{\rm cal}$ of a proton was calculated from initial Σ^+ momentum vector analyzed with the spectrometers and the angle of the proton reconstructed by CATCH. By comparing $E_{\rm cal}$ or $p_{\rm cal}$ with the measured proton energy $E_{\rm meas}$ or momentum $p_{\rm meas}$ using CATCH , the events for the reaction were identified as a peak in the kinematical consistency spectra. Kinematical consistency is defined as $\Delta E = E_{\rm meas} - E_{\rm cal}$ or $\Delta p = p_{\rm meas} - p_{\rm cal}$.

5.2.1 Kinematical consistency check for the decay proton from $\Sigma^+ \to p\pi^0$ decay

The most simple example of a kinematical consistency check is the $\Sigma^+ \to p\pi^0$ decay case. This is also the easiest reaction to analyze because Σ^+ decays into $p\pi^0$ with a probability of 51 %. The schematic drawing of $\Sigma^+ \to p\pi^0$ decay is shown in Figure 5.1.

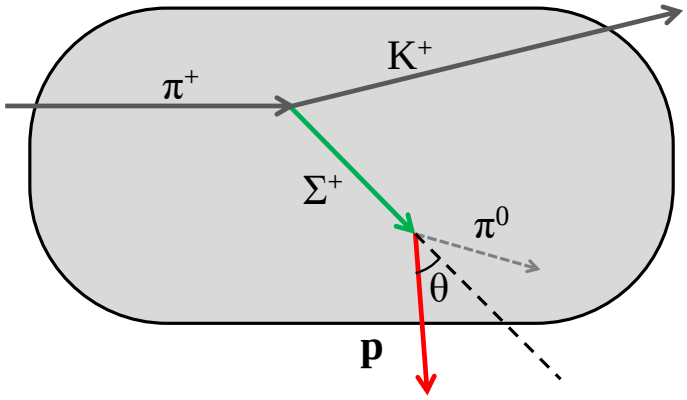

Figure 5.1: Schematic drawing of the $\Sigma^+ \to p\pi^0$ decay. θ indicates the opening angle between the Σ^+ track reconstructed with the spectrometers and the proton track reconstructed with CATCH.

The kinematical consistency check for this reaction can be performed for events, in which at least one proton was detected with CATCH. The kinetic energy of the decay proton can be calculated from the momentum of the Σ^+, p_Σ, and the opening angle between the Σ^+ and proton track θ as

$$E_{\mathrm{decay}p,\mathrm{cal}} = \sqrt{p^2_{\mathrm{decay}p,\mathrm{cal}} + m_p^2} - m_p, \tag{5.1}$$

$$p_{\mathrm{decay}p,\mathrm{cal}} = \frac{Ap_\Sigma \cos\theta + \sqrt{D}}{E_\Sigma^{\mathrm{tot}\,2} - p_\Sigma^2 \cos^2\theta}, \tag{5.2}$$

$$A = \frac{m_\Sigma^2 + m_p^2 - m_{\pi^0}^2}{2},$$

$$D = (Ap_\Sigma \cos\theta)^2 - (E_\Sigma^{\mathrm{tot}\,2} - p_\Sigma^2 \cos^2\theta)(m_p^2 E_\Sigma^{\mathrm{tot}\,2} - A^2),$$

where m_Σ, m_p, and m_{π^0} are the mass of Σ^+, p, and π^0, respectively. $E_\Sigma^{\mathrm{tot}} = \sqrt{m_\Sigma^2 + p_\Sigma^2}$ is the total energy of the incident Σ^+. The obtained ΔE spectrum is shown in Figure 5.2. The clear peak can be seen around $\Delta E = 0$. In this way, kinematical consistency check for a given reaction was performed.

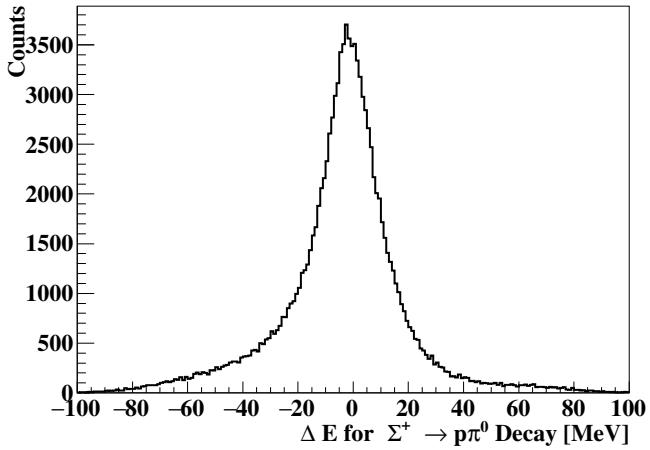

Figure 5.2: ΔE spectrum for the $\Sigma^+ \to p\pi^0$ decay.

5.2.2 Kinematical consistency check for the decay proton of pp scattering following the $\Sigma^+ \to p\pi^0$ decay

The pp scattering following the $\Sigma^+ \to p\pi^0$ decay shown in Figure 5.3 is the main background reaction in analyzing events with two proton in final state. This reaction can be identified by the kinematical consistency check for the decay proton.

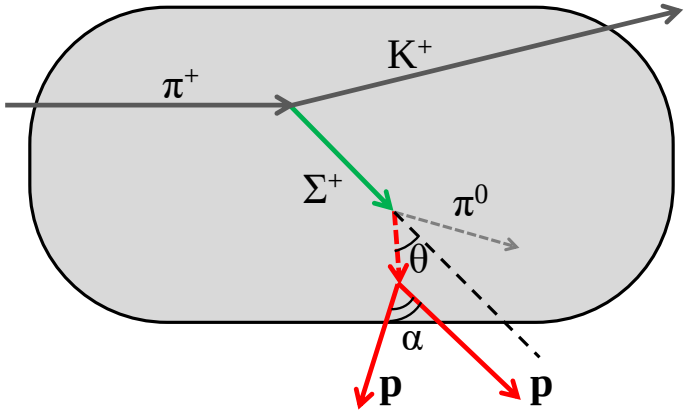

Figure 5.3: Schematic of the pp scattering following the $\Sigma^+ \to p\pi^0$ decay. θ indicates the opening angle between the Σ^+ track reconstructed with spectrometers and the decay proton track. The momentum of the decay proton was reconstructed from the momenta of the two protons detected with CATCH.

The analysis for this reaction required the detection of two protons with CATCH. Assuming the two protons were derived from this reaction, the momentum of the decay

proton $\boldsymbol{p}$ can be reconstructed from the momenta of the two detected protons, $\boldsymbol{p_1}$ and $\boldsymbol{p_2}$, as $\boldsymbol{p} = \boldsymbol{p_1} + \boldsymbol{p_2}$. The reconstructed momentum amplitude was regarded as p_{meas}. Because the incident proton in this pp scattering is also the decay proton from the $\Sigma^+ \to p\pi^0$ decay, the reconstructed momentum should satisfy the Σ^+ decay kinematics for a real pp scattering event. This kinematical consistency check was performed by evaluating the consistency between p_{meas} and the calculated momentum p_{cal}, which is calculated from equation (5.2) using the emission angle of the decay proton from the initial Σ^+. The opening angle of the two protons, α, was also verified because α is kinematically constrained to be approximately 90° for the pp scattering event. The correlation between Δp and α is illustrated in the left side of Figure 5.4, where a clear event concentration owing to pp scattering can be confirmed. The right side of Figure 5.4 shows the Δp spectrum with the opening angle gate.

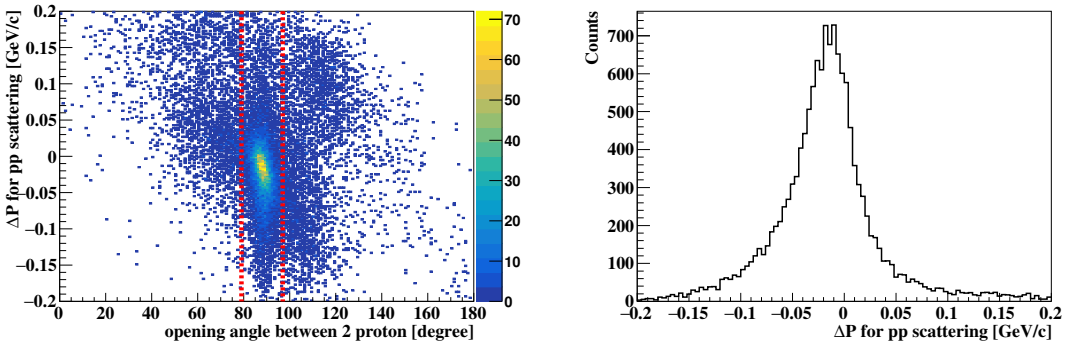

Figure 5.4: (Left) Correlation of the Δp and the opening angle between two detected proton α and (Right) Δp spectra for the pp scattering following $\Sigma^+ \to p\pi^0$ decay. In the Δp spectrum, $79° < \alpha < 97°$ gate was applied.

5.2.3 Kinematical consistency check for the recoil proton from the $\Sigma^+ p$ scattering

A schematic drawing of $\Sigma^+ p$ scattering in the LH_2 target is shown in Figure 5.5. The $\Sigma^+ p$ scattering event identification was performed by a kinematical consistency check for the recoil proton indicated by the red arrow in Figure 5.5. The kinetic energy of the recoil proton E_{cal} can be calculated from the momentum of the incident Σ^+ and the recoil angle of the recoil proton θ as

$$E_{\mathrm{cal}} = \frac{2m_p p_\Sigma^2 \cos^2\theta}{(E_\Sigma^{\mathrm{tot}} + m_p)^2 - p_\Sigma^2 \cos^2\theta}. \tag{5.3}$$

After $\Sigma^+ p$ scattering, the scattered Σ^+ decays mainly into $n\pi^+$ or $p\pi^0$. For $\Sigma^+ p$ scattering followed by $\Sigma^+ \to n\pi^+$ decay, one proton of the recoil proton is in the final state. Figure 5.6 shows the ΔE spectra for the events with one proton in the final state. The left side of Figure 5.6 is the spectrum without event selection to emphasize the $\Sigma^+ p$ scattering events and the right is the one with it. Even after applying the event selection, there were substantial backgrounds. Like this, this recoil proton is severely contaminated by

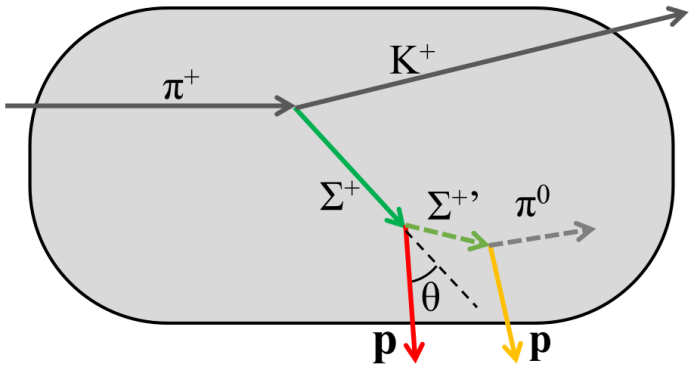

Figure 5.5: Schematic drawing of the $\Sigma^+ p$ scattering followed by the $\Sigma^+ \to p\pi^0$ decay. θ indicates the opening angle between the Σ^+ track, which is reconstructed from the incoming π^+ and outroing K^+ using the spectrometers, and the recoil proton track measured with CATCH.

the mere $\Sigma^+ \to p\pi^0$ decay and other secondary background events. Therefore, we focus on $\Sigma^+ p$ scattering followed by $\Sigma^+ \to p\pi^0$ decay, in which two protons can be observed with CATCH.

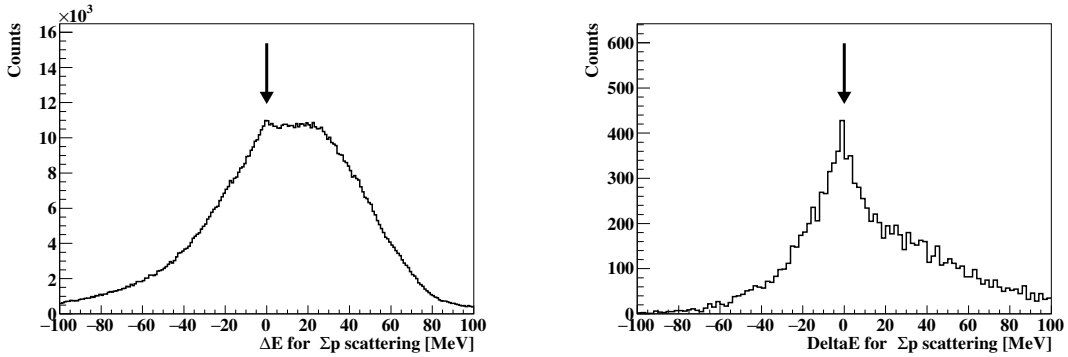

Figure 5.6: ΔE spectra for the $\Sigma^+ p$ scattering followed by the $\Sigma^+ \to n\pi^+$ decay. In the left figure, the event selection to emphasize $\Sigma^+ p$ scattering events are not applied. The substantial backgrounds are seen even in the right figure after applying the event selection.

In the following analysis, the detection of two protons with CATCH is required and these events are called "two-proton events". The ΔE spectrum for two-proton events is shown in the left side of Figure 5.7. In the analysis of two-proton events, the proton with the smaller $|\Delta E|$ value was regarded as the recoil proton. In the left side of Figure 5.7, a peak structure can be identified around $\Delta E = 0$ without any further selection of the $\Sigma^+ p$

scattering.

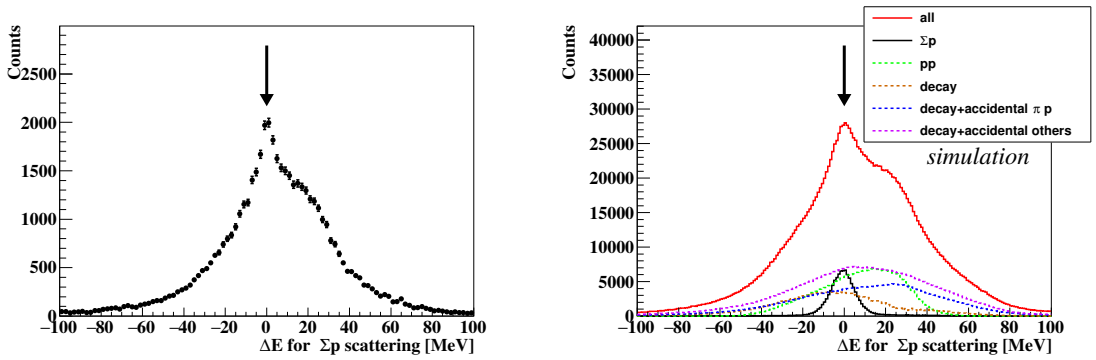

Figure 5.7: ΔE spectra for the two-proton events without cuts to select the $\Sigma^+ p$ scattering events for data (Left) and simulation (Right). As shown by the arrows, a peak structure was identified around $\Delta E = 0$. In the simulation (right), the contributions of the assumed reactions are additionally shown, reaction-by-reaction.

The ΔE spectrum was compared with that of a Monte Carlo simulation. As the background contamination in the two-proton events, the four cases shown in Figure 5.8 were considered in the simulation. Figure 5.8 (a) shows the pp scattering following $\Sigma^+ \to p\pi^0$ decay. In the case shown in Figure 5.8 (b), the $\Sigma^+ \to p\pi^0$ decay finally produces a proton and e^+e^- pair, where the e^+ or e^- are misidentified as a proton by CATCH. The misidentification is caused by $e^\pm$ with a large energy deposit in CFT as mentioned in Subsection 4.4.4. Because the misidentification was reproduced in the simulation, we can estimate this background contribution by generating mere Σ^+ decay events in the simulation. The two other reactions are accidental coincidences of Σ^+ production and different reactions of the LH_2 target or target vessel, shown in Figure 5.8 (c) and (d), respectively, induced by the accidental π^+ beam. To reproduce accidental backgrounds, the probability of accidental coincidence and the distributions of the energy and angle of the accidental protons were estimated as described in Subsection 4.5.3. From this analysis, the probabilities for types (c) and (d) were obtained as approximately 0.8% and 1.2% for the number of Σ^+ production events, respectively. These probabilities are considered in the simulations. The right side of Figure 5.7 shows the ΔE spectrum obtained by analyzing the simulation, considering these backgrounds. The simulated spectrum consistently reproduced that of the real data.

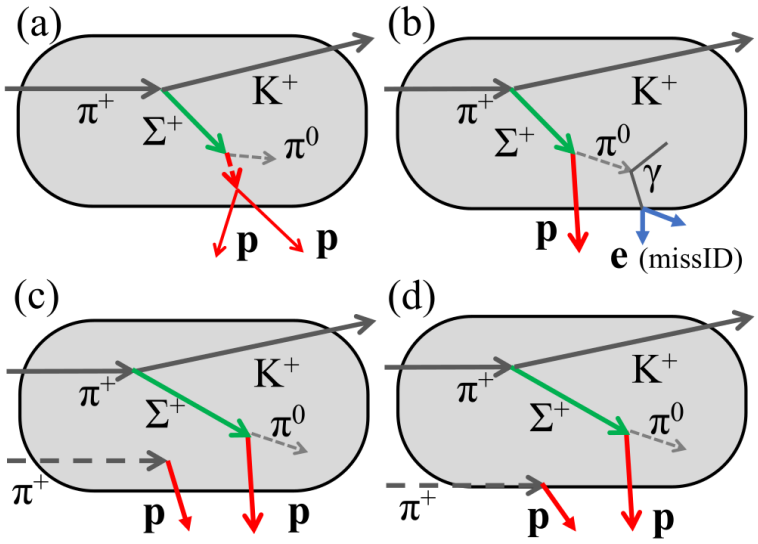

Figure 5.8: Schematics of four types of backgrounds in the two-proton events, (a) the pp scattering following the $\Sigma^+ \to p\pi^0$ decay, (b) the combination of a proton from the $\Sigma^+ \to p\pi^0$ decay and misidentified $e^{\pm}$, (c) the combination of a proton from the $\Sigma^+ \to p\pi^0$ decay and a proton from the elastic $\pi^+ p$ scattering in the LH_2 target caused by the accidental π^+, and (d) the combination of a proton from the $\Sigma^+ \to p\pi^0$ decay and a proton from the scattering between the accidental π^+ and the target vessel.

5.3 Cut conditions to select the $\Sigma^+ p$ scattering events

To reduce backgrounds from the ΔE spectrum, shown in Figure 5.7, additional cuts regarding the spatial and kinematical information obtained from the two detected protons were applied. The detailed procedure is described in the following subsections. Table 5.1 summarizes the survival ratios for $\Sigma^+ p$ scattering events and the considered four types of background events. Finally, more than 90% of the background events were eliminated, while maintaining approximately half of the $\Sigma^+ p$ scattering events.

Table 5.1: Survival ratios of the $\Sigma^+ p$ scattering and background events after applying cuts as described in each subsection. (a)-(d) types correspond to the background types in Figure 5.8.

	$\Sigma^+ p$	(a) type	(b) type	(c) type	(d) type
Cuts in 5.3.1	89.9%	69.3%	74.8%	55.7%	53.5%
Cuts in 5.3.2	86.7%	68.2%	8.3%	13.0%	5.7%
Cuts in 5.3.3	69.8%	12.8%	7.6%	11.3%	4.7%
Cuts in 5.3.4 (All cuts)	54.5%	7.1%	5.5%	0.4%	1.6%

5.3.1 Vertex cut and closest distance cut

The spatial consistency between two proton tracks can be used to select Σ^+p scattering events. The vertex of Σ^+p scattering, which was calculated as the closest point between the incident Σ^+ and recoil proton tracks, should be inside the target. Accordingly, the scattering vertex $(x_{\rm scat}, y_{\rm scat}, z_{\rm scat})$ must be $x_{\rm scat}^2 + y_{\rm scat}^2 < 25^2$ mm^2, and $|z_{\rm scat}| < 170$ mm as shown in the Figure 5.9.

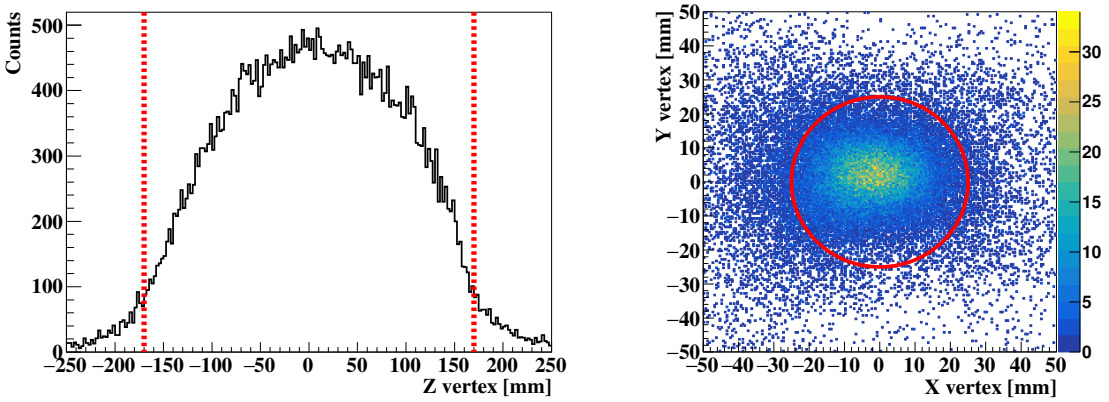

Figure 5.9: Reconstructed Σ^+p scattering vertex distribution of two-proton events in the analysis. The region inside the red lines are accepted.

Similarly, the decay vertex $(x_{\rm decay}, y_{\rm decay}, z_{\rm decay})$, which was obtained from the decay proton and scattered Σ^+, was required to be $-30 < x_{\rm decay} < 25$ mm, $|y_{\rm decay}| < 30$ mm, and $|z_{\rm decay}| < 180$ mm as shown in Figure 5.10. The momentum vector of the scattered Σ^+, denoted as $\Sigma^{+\prime}$, can be kinematically calculated from the recoil angle of the proton. The trajectory of $\Sigma^{+\prime}$ is reconstructed from the momentum vector and the scattering vertex.

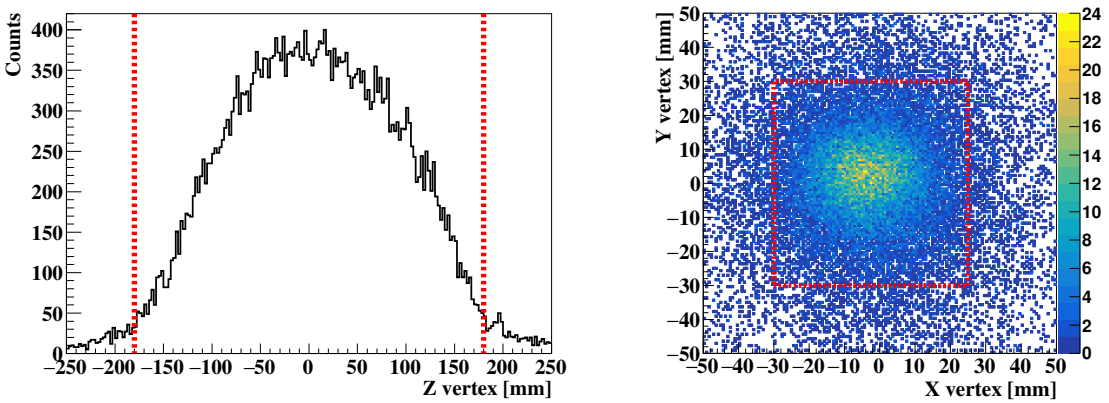

Figure 5.10: Reconstructed $\Sigma^+ \to p\pi^0$ decay vertex distribution of two-proton events in the analysis. The region inside the red lines are accepted.

The closest distances between Σ^+ and the proton tracks at the scattering and decay points also reflect spatial consistency. The simulated distributions of the closest distances at the two vertices are shown in Figure 5.11. The closest distances at the scattering and decay points were required to be less than 20 mm and 25 mm, respectively. These cuts can reduce the background events by 30–50% while maintaining approximately 90% of the Σ^+p scattering events, as shown in the second row of Table 5.1.

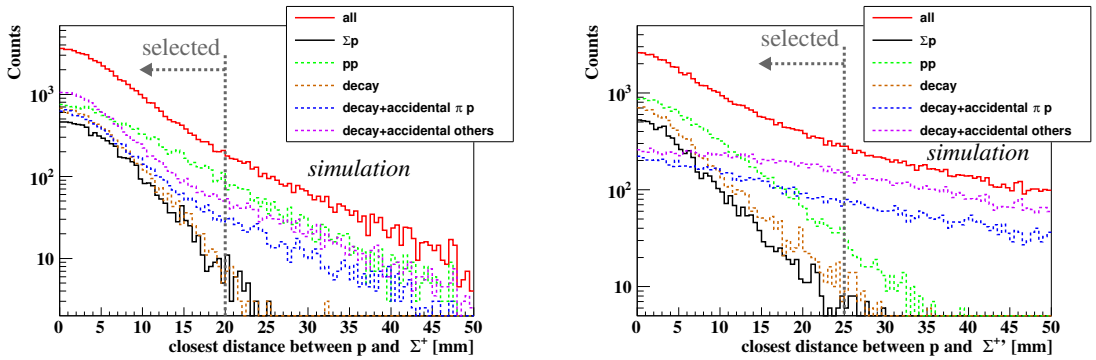

Figure 5.11: Simulated distributions of the closest distances at the scattering (left) and decay points (right). The dotted lines indicate the boundaries of selected regions: 20 and 25 mm at the scattering and decay points, respectively..

5.3.2 Missing mass cut to select the scattered Σ^+ decay

Assuming that Σ^+p scattering is followed by $\Sigma^{+\prime} \to p\pi^0$ decay, the missing mass of the $\Sigma^{+\prime} \to pX$ reaction, M_X, should be the mass of π^0. The squared missing mass (M_X^2) distribution shows a π^0 peak and a broad distribution toward the negative region, as shown in Figure 5.12. The broad distribution in the negative region was mainly attributed to accidental backgrounds. The event forming the π^0 peak comes not only from Σ^+p scattering, but also from pp scattering following the $\Sigma^+ \to p\pi^0$ decay, because both reactions have the same final state of $pp\pi^0$, originating from the initial Σ^+. The green shaded spectrum in Figure 5.12 shows the M_X^2 distribution for pp scattering, selected Δp and α gate described in the next subsection. The cut condition $M_X^2 > 0$, shown by the dotted line in Figure 5.12, was determined to include the green spectrum. The survival ratios estimated from the Monte Carlo simulation are listed in the third row of Table 5.1.

5.3.3 Kinematical cut for secondary pp scattering

The pp scattering following the $\Sigma^+ \to p\pi^0$ decay, shown in Figure 5.8 (a), can be identified by the kinematical consistency check for the decay proton as described in Subsection 5.2.2. Events from this reaction were rejected using the correlation between Δp and α, shown in Figure 5.13. To reject the identified pp scattering events, the cut region defined as the $\pm 2\sigma$ areas for Δp and α was defined, as shown by the red box in Figure 5.13. Although this cut condition rejected approximately 20% of the Σ^+p scattering events, the signal-to-noise (S/N) ratio was improved by cutting approximately 80% of the secondary pp scattering events.

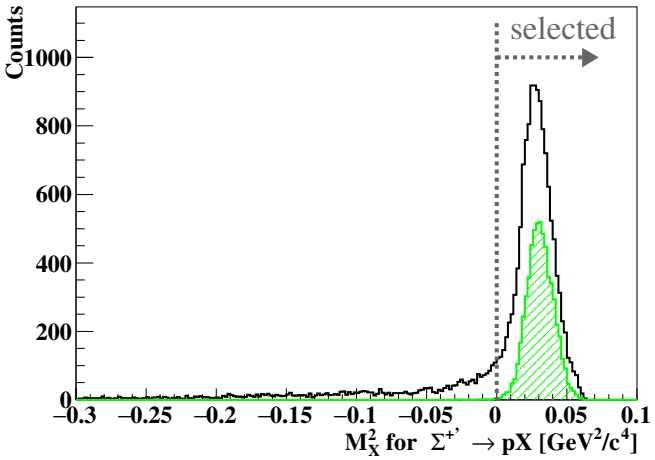

Figure 5.12: Squared missing mass distribution of the $\Sigma^{+'} \to pX$ reaction. The green shaded spectrum shows the pp scattering following the $\Sigma^+ \to p\pi^0$ decay, which can be selected using the kinematical consistency and opening angle of the two detected protons, as explained in the Subsection 5.3.3. Here, $M_X^2 > 0$ is selected.

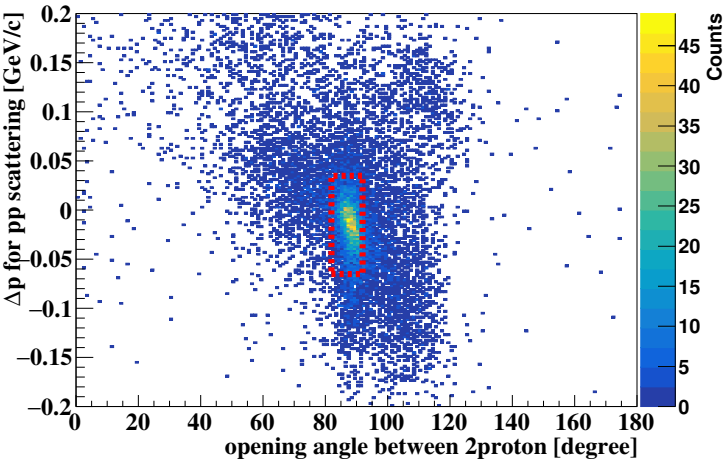

Figure 5.13: Correlation between Δp and the opening angle α of two detected protons from real data. The events inside the red-line region were rejected as the secondary pp scattering background.

5.3.4 Kinematical cut for $\pi^+ p$ elastic scattering

Finally, the rejection of the accidental coincidence of $\pi^+ p$ elastic scattering is described. The recoil proton by $\pi^+ p$ elastic scattering has a kinematical correlation between the recoil angle and energy. Figure 5.14 shows the correlation between the angle of protons with respect to the central axis of CFT and the energy. The locus corresponding to the $\pi^+ p$ kinematics, indicated by the red dotted line, can be confirmed. The events inside the red-line region in Figure 5.14 were rejected as the protons from elastic $\pi^+ p$ scattering.

This cut reduced almost all of the type (c) background in Figure 5.8.

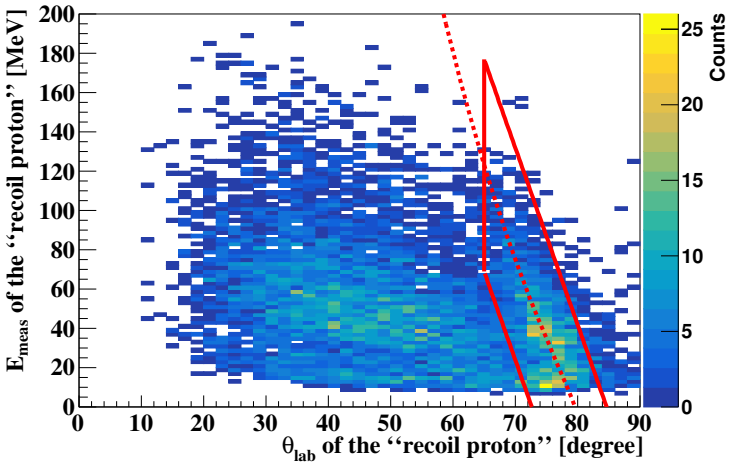

Figure 5.14: Correlation between the angle of protons with respect to the central axis of CFT, $\theta_{\rm lab}$, and E_{meas} of the recoil proton. The red dotted line indicates the kinematics of π^+p elastic scattering induced by the 1.41-GeV/c π^+ beam. When calculating the kinematics, the energy loss in the LH_2 target was considered. The events inside the red-line region were rejected as the protons from elastic π^+p scattering in response to the accidental π^+.

5.3.5 Σ^+p scattering identification after all cuts

The ΔE spectrum for two-proton events after applying all cuts is shown in the left side of the Figure 5.15. The S/N ratio in the peak region of $-20 < \Delta E[\mathrm{MeV}] < 20$ was 1.78, significantly improved from that of Figure 5.7. The evaluation of the S/N ratio is based on the fitting results of the ΔE spectra explained in the next section. The simulated spectrum after the same cuts, which is shown in the right side of Figure 5.15, agreed with the data. The analysis efficiency for the Σ^+p scattering events was estimated to be 54.5%, and the rejection factors of the four background sources were higher than 90%, as summarized in Table 5.1.

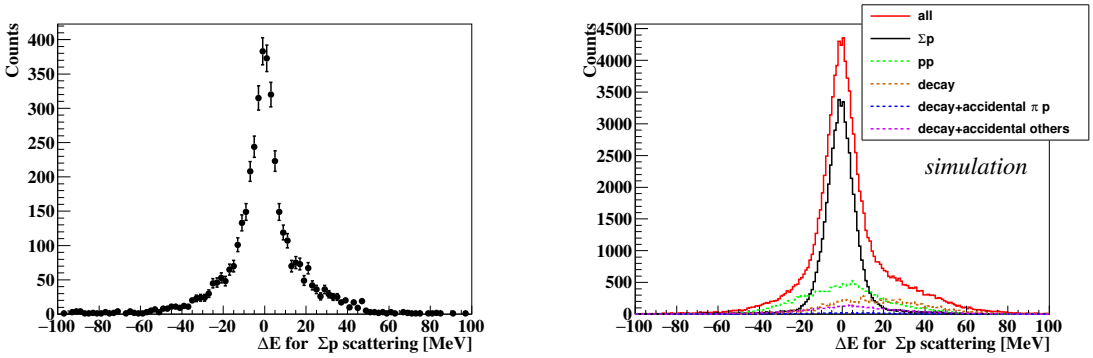

Figure 5.15: ΔE spectra for the two-proton events with cuts to select the $\Sigma^+ p$ scattering events for (left) data and (right) simulation. In the simulation (right), the contributions of the assumed reactions are shown reaction-by-reaction.

5.4 Estimation of the number of $\Sigma^+ p$ scattering events

To estimate the number of $\Sigma^+ p$ scattering events and survival background events, the ΔE spectrum for the $\Sigma^+ p$ scattering was fitted with the sum of the simulated spectra for both the $\Sigma^+ p$ scattering and background reactions. Fitting was performed for the ΔE spectrum at each scattering angle independently to correctly reproduce the angular dependence of the background contribution. In order to constrain the contribution of the pp scattering events in this fitting, the Δp spectrum for the pp scattering kinematics was simultaneously fitted. The fitting method was the maximum log-likelihood method, in which parameters were optimized to minimize the negative log likelihood described as

$$-\log \mathcal{L}_p = -\log \mathcal{L}_{p,\Delta E} - \log \mathcal{L}_{p,\Delta p}, \tag{5.4}$$

$$-\log \mathcal{L}_{p,\Delta E} = \sum_{i=1}^{N_{\rm bin}} \left(f_{i,\Delta E} - N^{\rm data}_{i,\Delta E} \cdot \log f_{i,\Delta E} \right), \tag{5.5}$$

$$f_{i,\Delta E} = C_{\Sigma^+ p} N^{{\rm sim},\Sigma p}_{i,\Delta E} + C_a N^{{\rm sim},a}_{i,\Delta E} + C_b N^{{\rm sim},b}_{i,\Delta E} + C_c N^{{\rm sim},c}_{i,\Delta E} + C_d N^{{\rm sim},d}_{i,\Delta E}, \tag{5.6}$$

$$-\log \mathcal{L}_{p,\Delta p} = \sum_{i=1}^{N_{\rm bin}} \left(f_{i,\Delta p} - N^{\rm data}_{i,\Delta p} \cdot \log f_{i,\Delta p} \right),$$

$$f_{i,\Delta p} = C_{\Sigma^+ p} N^{{\rm sim},\Sigma p}_{i,\Delta p} + C_a N^{{\rm sim},a}_{i,\Delta p} + C_b N^{{\rm sim},b}_{i,\Delta p} + C_c N^{{\rm sim},c}_{i,\Delta p} + C_d N^{{\rm sim},d}_{i,\Delta p},$$

where $C_{\Sigma^+ p}, C_a, C_b, C_c, C_d$ were the parameters corresponding to the scale factors of simulated distributions. $N_{i,\Delta E}$ and $N_{i,\Delta p}$ are counts of the i-th bin of the histograms and the subscripts $a - d$ correspond to the type of backgrounds in Figure 5.8.

The cut condition for the Δp spectrum, where the pp scattering rejection cut described in subsection 5.3.3 was not applied, was different from that for the ΔE spectrum in order to emphasize the contribution of the pp scattering events. The fitting for only the ΔE spectra was also examined in order to study the systematic differences due to the background estimation and fitting procedure. The uncertainty due to the bin size of the spectra was also estimated by iterating the same procedure for the spectra with different sets of bin sizes. The difference in the estimated $\Sigma^+ p$ scattering events in these fittings is considered as the systematic uncertainty.

The fitting results of ΔE for all measurements within detector acceptance are shown in Figure 5.16, 5.17, and 5.18. A fitting result of Δp spectra for the low momentum region is also shown in Figure 5.19.

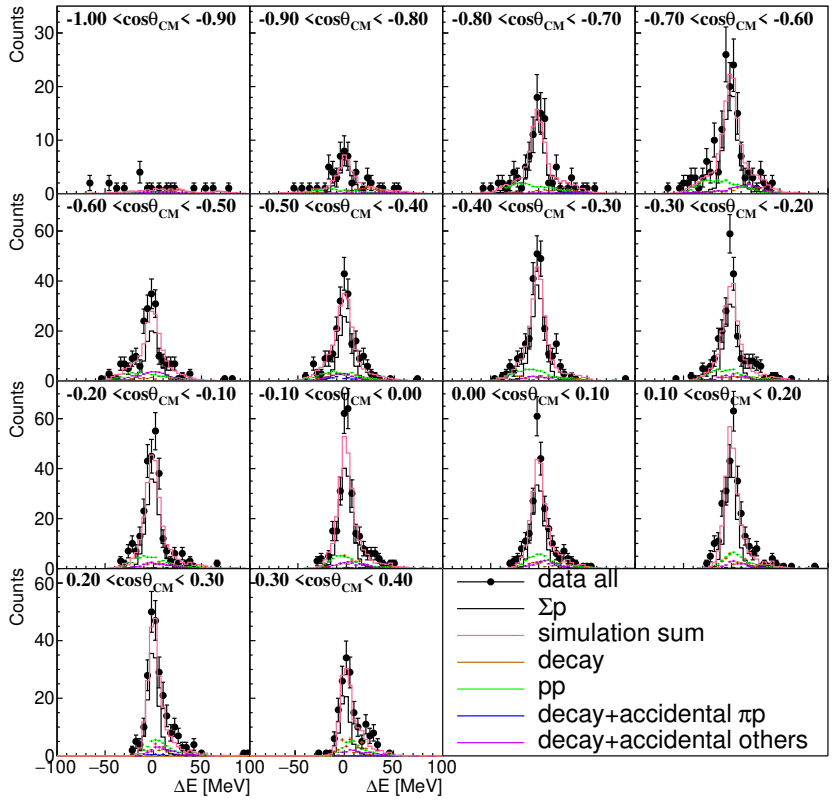

Figure 5.16: ΔE spectra at each scattering angle of Σ^+ in the low-momentum region ($0.44 < p_\Sigma[\mathrm{GeV}/c] < 0.55$). The data points with error bars show the experimental data. Simulated spectra for the assumed reactions are also shown and the red histogram showing the sum of these spectra.

As shown in these spectra, the S/N ratio of the ΔE spectra worsened in the forward angular region because of the limited acceptance of the low-energy recoil proton. Therefore, we set the maximum scattering angle for each incident Σ^+ momentum region: $\cos\theta_{\mathrm{CM}} = 0.4$ for the low momentum region, $\cos\theta_{\mathrm{CM}} = 0.5$ for the middle momentum region, and $\cos\theta_{\mathrm{CM}} = 0.6$ for the high momentum region. The estimated numbers of Σ^+p scattering events for each incident Σ^+ momentum region are shown in Figure 5.20 as a function of $\cos\theta_{\mathrm{CM}}$. The error bars and boxes represent statistical and systematic errors, respectively. The systematic error derived from the uncertainty in the background estimation, as previously discussed. A total of approximately 2400 Σ^+p scattering events were identified.

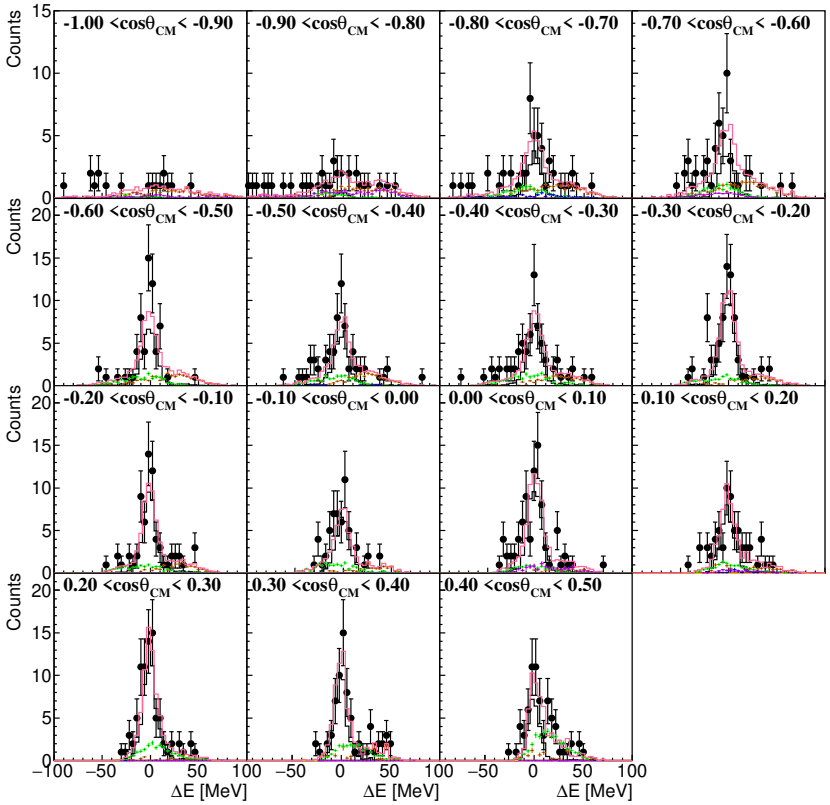

Figure 5.17: ΔE spectra at each scattering angle of Σ^+ in the middle-momentum region ($0.55 < p_\Sigma[\mathrm{GeV}/c] < 0.65$). The legends are the same as those in Figure 5.16.

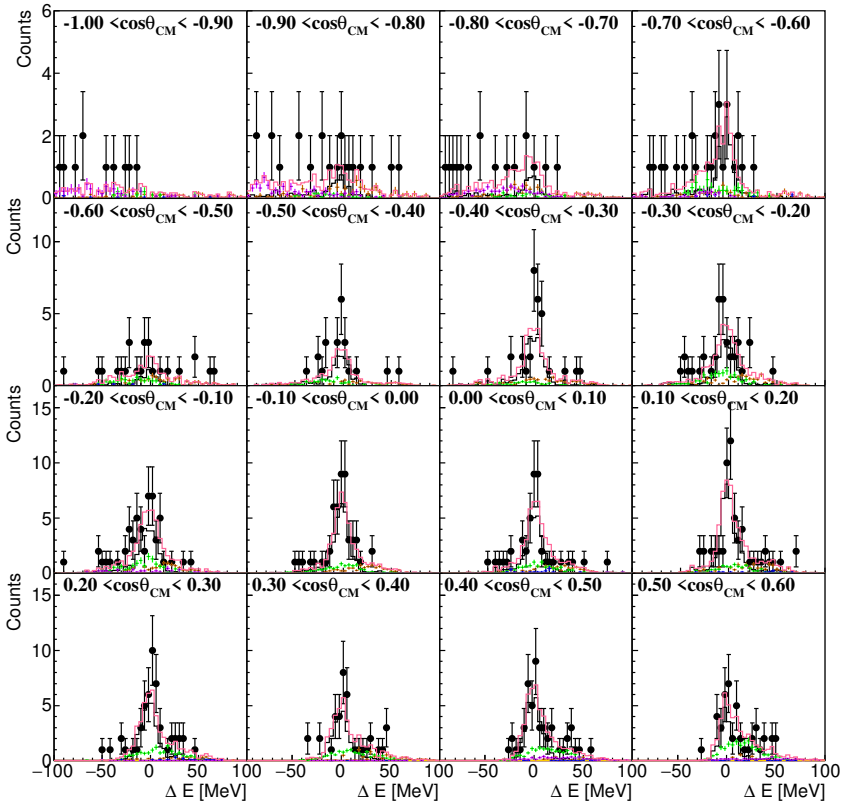

Figure 5.18: ΔE spectra at each scattering angle of Σ^+ in the high-momentum region ($0.65 < p_\Sigma[\mathrm{GeV}/c] < 0.80$). The legends are the same as those in Figure 5.16.

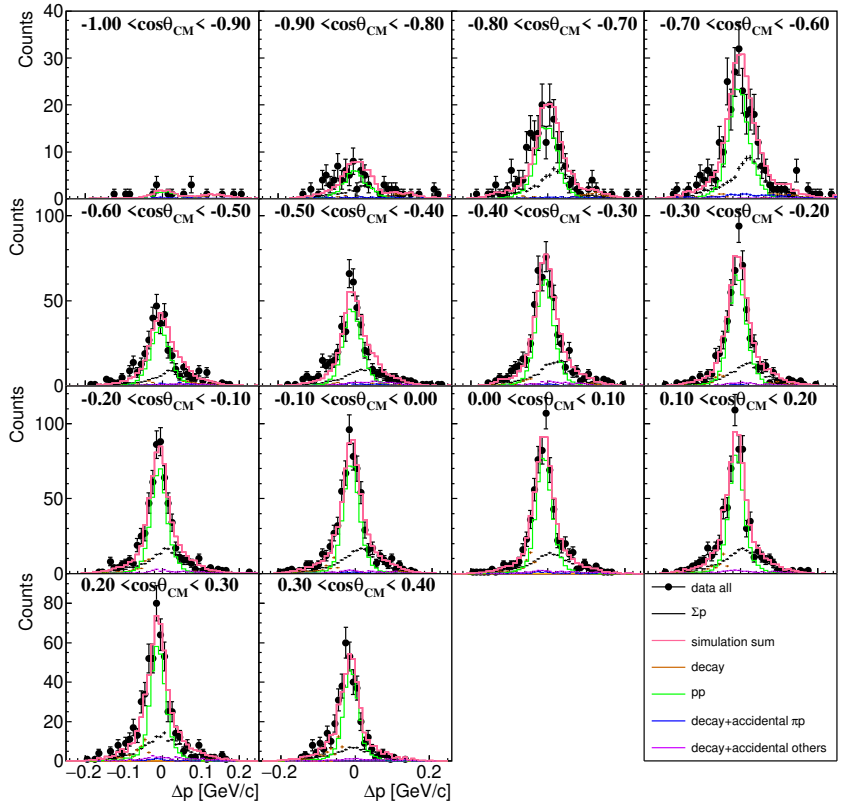

Figure 5.19: Δp spectra at each scattering angle of Σ^+ in the low-momentum region ($0.44 < p_\Sigma[\mathrm{GeV}/c] < 0.55$). The legends are the same as those in Figure 5.16.

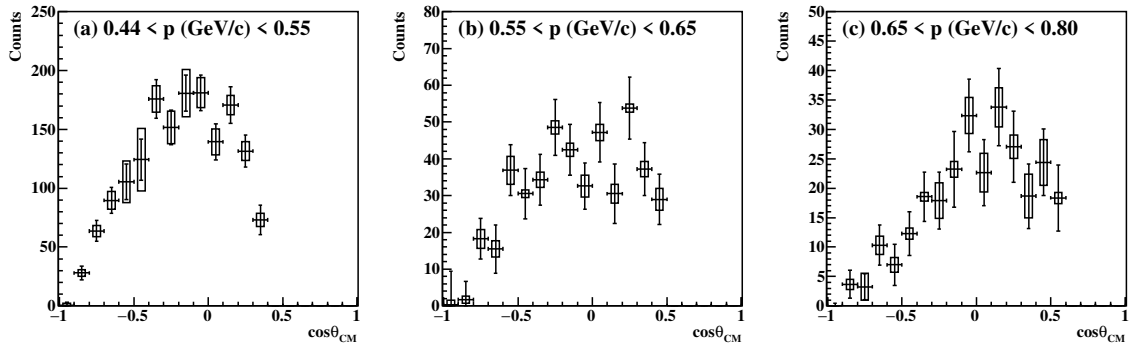

Figure 5.20: Estimated numbers of the $\Sigma^+ p$ scattering events for each scattering angle and momentum region of Σ^+: (a) the low momentum region ($0.44 < p_\Sigma[\mathrm{GeV}/c] < 0.55$), (b) the middle momentum region ($0.55 < p_\Sigma[\mathrm{GeV}/c] < 0.65$), and (c) the high momentum region ($0.65 < p_\Sigma[\mathrm{GeV}/c] < 0.80$). The error bars and boxes indicate the statistical and systematic errors, respectively.

Chapter 6

Analysis III: Evaluations of factors to derive the differential cross sections

6.1 Outline

For deriving the differential cross sections, several values should be evaluated for each scattering angle and Σ^+ momentum region. Therefore, these values are denoted as a function of p_Σ and $\cos\theta_{\rm CM}$, such that $N(p_\Sigma, \cos\theta_{\rm CM})$ represents the number of scattering events. The differential cross section was calculated as follows:

$$\frac{d\sigma}{d\Omega} = \frac{N(p_\Sigma, \cos\theta_{\rm CM})}{\rho \cdot N_A \cdot L(p_\Sigma) \cdot \bar{\varepsilon}(p_\Sigma, \cos\theta_{\rm CM}) \cdot \Delta\Omega}, \tag{6.1}$$

where ρ and N_A represent the density of the LH_2 target, 0.071 g/cm^3, and Avogadro's number, respectively. $L(p_\Sigma)$ is the total flight length of the incident Σ^+ in the LH_2 target. $\bar{\varepsilon}$ represents the efficiency of the Σ^+p scattering event averaged for the vertex position. $\Delta\Omega$ represents a constant solid angle of $\Delta\Omega = 2\pi\Delta\cos\theta_{\rm CM}$. The following sections describe the evaluation of each factor.

6.2 Total track length of the incident Σ^+ in the LH_2 target

In ordinary scattering experiments, the expression $\rho \cdot N_{Avo} \cdot t \cdot N_{\rm beam}$ is used for the luminosity, where t and $N_{\rm beam}$ represent a target thickness and number of beam particles, respectively. However, this evaluation is inappropriate in this experiment because the incident Σ^+ was produced in the LH_2 target, and primarily decayed inside the target. The direct measurement of the Σ^+ track length, event-by-event, is also difficult because of the limited acceptance for the decay proton. However, the total track length of the incident Σ^+ can be reliably evaluated using a Monte Carlo simulation. Information regarding the production vertices and momentum vectors of all identified incident Σ^+ particles was obtained from the spectrometer analysis. Σ^+ particles with measured momenta were generated at the production points in the passage simulator described in Section 3.2. The flight length of Σ^+ was subsequently summed until Σ^+ decayed or exited the target. Figure 6.1 shows the estimated Σ^+ track length distribution. The total track lengths for each momentum region $L(p_\Sigma)$ were obtained by integrals of these histograms. The

background contribution in the Σ^+ identification was also estimated from the sideband event in the m^2 distribution. Table 6.1 summarizes the estimated total track lengths after subtracting background contributions.

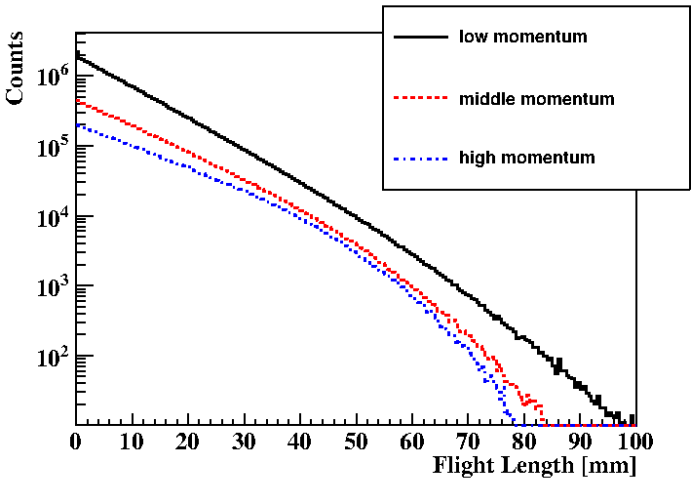

Figure 6.1: Distribution of estimated Σ^+ track lengths for the three momentum regions.

Table 6.1: Estimated Σ^+ total track lengths for the three momentum regions: low-momentum region ($0.44 < p_\Sigma[\mathrm{GeV}/c] < 0.55$), middle-momentum region ($0.55 < p_\Sigma[\mathrm{GeV}/c] < 0.65$), and high-momentum region ($0.65 < p_\Sigma[\mathrm{GeV}/c] < 0.80$). The values in the row of "All events" include the contributions from the miscalculated background events. The background contributions are listed in the row of "Sideband BG". By subtracting "sideband BG" from "All events", the Σ^+ track length was calculated and is listed in the row labeled "Σ^+".

Region	Low	Middle	High
All events [cm]	3.69×10^7	1.13×10^7	6.70×10^6
Sideband BG [cm]	0.27×10^7	0.12×10^7	0.86×10^6
Σ^+ [cm]	3.42×10^7	1.00×10^7	5.84×10^6

In this procedure, the simulation inputs of the vertex point and momentum vector contained uncertainties owing to the resolution and systematic errors of the spectrometers. This may have caused uncertainties in the estimated track length. The error of the total track length derived from the resolutions was at most 1%. If the Σ^+ momentum was systematically shifted due to the accuracy of the spectrometers, the track length would be affected. The momentum accuracy of the spectrometers depended on the scattering angle of K^+. In the worst case, the analyzed momentum of Σ^+ was expected to be 13 MeV/c larger. Even if the momenta of all Σ^+ were shifted +13 MeV/c systematically, the estimated total track length would change in 2-3 %. These uncertainty is considerably smaller than other uncertainties, such as the statistical errors shown in Figure 5.20.

6.3 Average efficiency of the Σ^+p scattering events including the detection and analysis efficiency

The average efficiency $\bar{\varepsilon}$ for the Σ^+p scattering events, including the detection and analysis efficiencies, was evaluated by analyzing the simulated data with the same analyzer program for the real data. Here, the difference in the detection efficiency of CATCH for protons between the simulation and real data should be considered. In the following, the evaluation of the CATCH efficiency was firstly discussed. Then, the average efficiency $\bar{\varepsilon}$ is obtained by correcting the difference between the simulation and real data.

6.3.1 Detection efficiency of CATCH

The detection efficiency of CATCH includes the geometrical acceptance, tracking efficiency of CFT, and the energy measurement efficiency for protons. They depend on the angle in the laboratory frame $\theta_{\rm lab}$, the kinetic energy E, and z-vertex position z. The efficiencies were evaluated based on the pp scattering data with seven beam momenta between 0.45 and 0.85 GeV/c. In the real pp scattering data, $(\theta_{\rm lab}, E)$ region were constrained by the kinematics, as shown in the left side of Figure 6.2. Therefore, the proton efficiency is also estimated with a Monte Carlo simulation, where protons with arbitrary angles and energies can be generated.

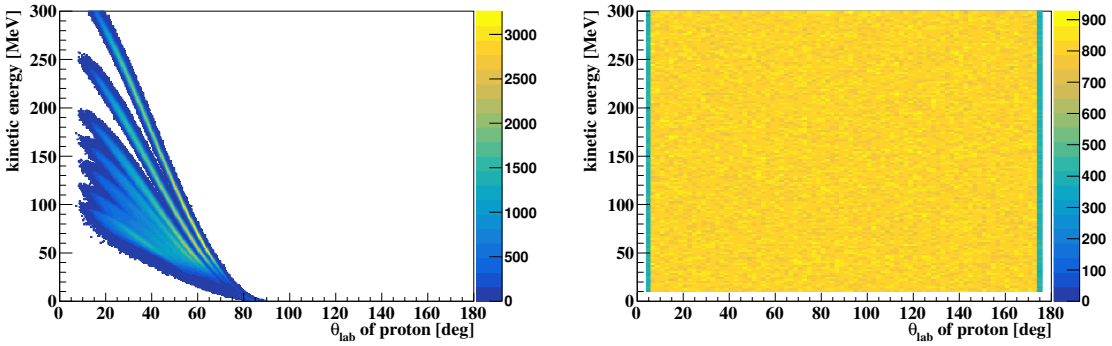

Figure 6.2: Correlations between the angle and energy of proton used for the efficiency evaluation. The left is the real pp scattering data and the right is the simulation.

The procedures for the efficiency evaluation using the pp scattering data are as follows:

1. For the efficiency estimation, at least one proton among the two protons in the final state must be detected by CATCH. From the kinematics, the momentum $(\boldsymbol{p}'(\theta'))$ of the detected proton with the recoil angle θ' was calculated. The scattering vertex $(x_{\rm scat}, y_{\rm scat}, z_{\rm scat})$ was also reconstructed as the closest point between the beam and recoil proton tracks.

2. The momentum vector of the other proton was obtained as $\boldsymbol{p} = \boldsymbol{p}_{\rm beam} - \boldsymbol{p}'(\theta')$, where the $\boldsymbol{p}_{\rm beam}$ was the proton beam momentum analyzed by the K1.8 beam-line spectrometer. From the momentum vector $\boldsymbol{p}$, the angle and kinetic energy of the second proton can be predicted; they are denoted as θ and E, respectively.

3. The CATCH efficiency was estimated by checking whether the predicted track and energy were measured or not. The tracking and energy measurement efficiencies were derived separately.

First, energy measurement efficiency $\varepsilon_{\mathrm{BGO}}(\theta, E, z_{\mathrm{scat}})$ is explained. In this case, we checked whether the measured energy for the predicted track agreed with the predicted E within 40 MeV. The obtained $\varepsilon_{\mathrm{BGO}}(\theta, E, z_{\mathrm{scat}})$ at $\theta = 37°$ is shown as the red points in the left side of Figure 6.3 as an example. This efficiency was compared with the efficiency estimated from the simulation. As shown in the left side of Figure 6.3, the simulation-based efficiency accurately reproduced the data-based efficiency. Therefore, the simulation-based efficiency for the energy measurement was used for further analysis to cover the entire θ, E, and z_{scat} regions. The efficiency was evaluated for each lattice in the (θ, E, z) space with a step of $(\Delta\theta, \Delta E, \Delta z) = (2.5°, 5\ \mathrm{MeV}, 30\ \mathrm{mm})$. For a given particle with (θ, E, z), a efficiency is calculated by the linear interpolation. The right side of Figure 6.3 shows the energy measurement efficiency map for $0 < z[\mathrm{mm}] < 30$ section, near the center of the target.

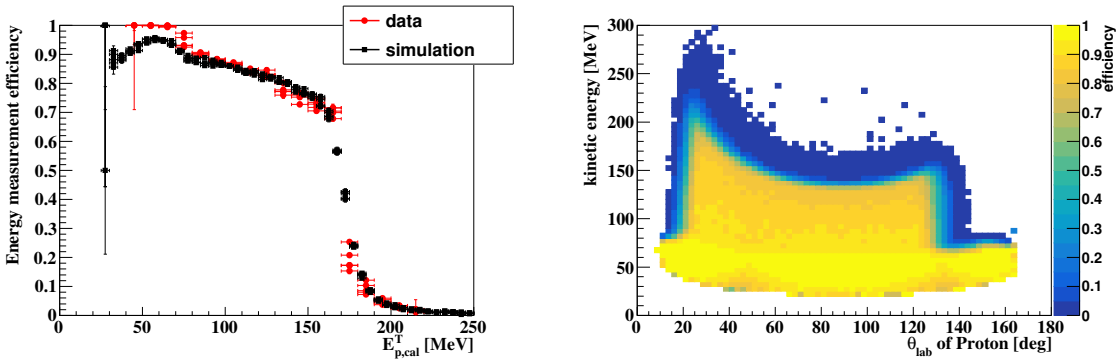

Figure 6.3: (Left) Energy measurement efficiency as a function of the kinetic energy at the scattering angle of $\theta_{\mathrm{lab}} = 37°$. The red circles and black squares represent the data and simulation, respectively. The efficiencies for the various z positions are written. The simulated efficiency reproduces the data well. (Right) Energy measurement efficiency map for $0 < z[\mathrm{mm}] < 30$ section evaluated by the simulation.

Hereafter, the tracking efficiency of CFT $\varepsilon_{\mathrm{CFT}}(\theta, E, z)$ is described. This was evaluated by checking whether a track with the predicted direction was detected. Therefore, the effect of detector acceptance was also included in $\varepsilon_{\mathrm{CFT}}$. The energy dependence of the tracking efficiencies estimated from the simulation and *pp* scattering data is shown by the black and red points in the left side of Figure 6.4, respectively. Because CFT tracking required at least six layer hits, the efficiency decreased sharply at low energies. This energy dependence of the efficiency can be phenomenologically represented by the Fermi function for both the data and simulation. The efficiency was then formulated as follows:

$$\varepsilon_{\mathrm{CFT}}(\theta, E, z) = \frac{\varepsilon_{\mathrm{max}}(\theta, z)}{1 + \exp\left(\frac{E - E_{\mathrm{half}}(\theta)}{d(\theta)}\right)}, \tag{6.2}$$

where $\varepsilon_{\mathrm{max}}(\theta, z), d(\theta)$ and $E_{\mathrm{half}}(\theta)$ are parameters representing the maximum efficiency, diffusion, and kinetic energy with half efficiency, respectively. These parameters were

determined for each (θ, z) area with a step of $(\Delta\theta, \Delta z) = (5°, 30\ \text{mm})$ by fitting Eq. (6.2) to the estimated efficiency, as indicated by the solid red line in the left side of Figure 6.4. The realistic efficiency is slightly lower than that of the simulation, typically by 10%. This difference is attributed to the geometrical effect of the fiber placement in the uv layers of CFT. There are ineffective regions for tracks with scattering angles of approximately 45°, owing to the zigzag fiber configuration in the uv layers. In addition, both the kinetic energy with half efficiency E_{half} and diffusion parameter d were slightly larger than those in the simulation. These differences indicated that the realistic amount of material in the experimental setup was larger than that considered in the simulation. It was difficult to incorporate the real spiral fiber configuration into the CFT uv layers and the missing amount of material within the simulation. Therefore, the data-based efficiency for CFT tracking was used for the analysis of the cross section. The right side of Figure 6.4 shows the efficiency map for $0 < z[\text{mm}] < 30$ section as a function of θ and E.

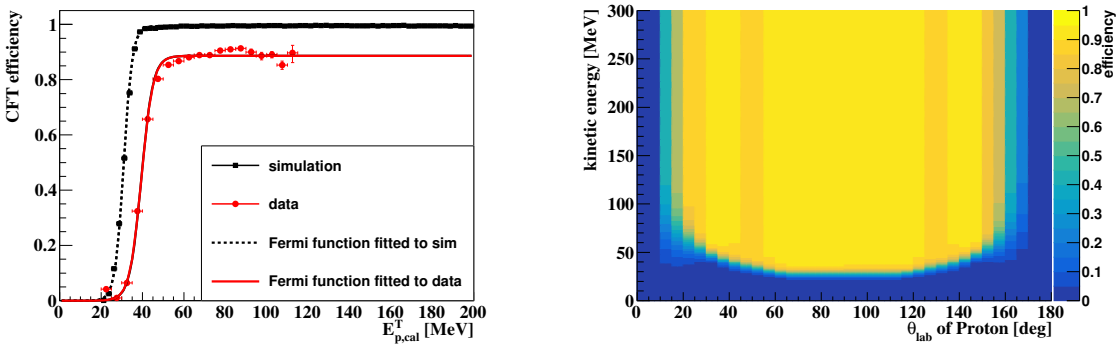

Figure 6.4: (Left) CFT tracking efficiency as a function of the kinetic energy at the scattering angle of $\theta_{\text{lab}} = 54°$. The red circles and black squares represent the data and simulation, respectively. The red and black curves are the fit functions obtained for the data and simulation. (Right) Data-based tracking efficiency map used for analysis, which was calculated from Eq. (6.2) and parameters were determined by the fitting to the real data. It is for $0 < z[\text{mm}] < 30$ section.

The obtained efficiency map was checked by deriving the differential cross sections for the calibration pp scattering data with proton beam. It was calculated as follows;

$$\frac{d\sigma}{d\Omega}(cos\theta_{\text{CM}}) = \frac{1}{\rho \cdot N_A \cdot \Delta z \cdot N_{\text{beam}} \Delta\Omega} \Big(\sum_{\text{events}}^{N(\cos\theta_{\text{CM}})} \frac{1}{\varepsilon_{\text{BGO}}(\theta_{\text{lab}}, E_{\text{cal}}, z_{\text{scat}}) \cdot \varepsilon_{\text{CFT}}(\theta_{\text{lab}}, E_{\text{cal}}, z_{\text{scat}})} \Big), \tag{6.3}$$

where ρ and N_A represent the density of the LH_2 target, 0.071 g/cm^3, and Avogadro's number, respectively. In the derivation, each z section with 30-mm length was regarded as the target. Therefore, target thickness Δz was 3 cm. N_{beam} was counted based on the beam tracking result: Whether a beam particle passed through the z section or not. The BGO and CFT efficiencies were corrected for each detected particle. Figure 6.5 shows typical derived differential cross sections for the pp scattering induced by the proton beam, which agreed with the reference values to within 5%, except for the acceptance edge.

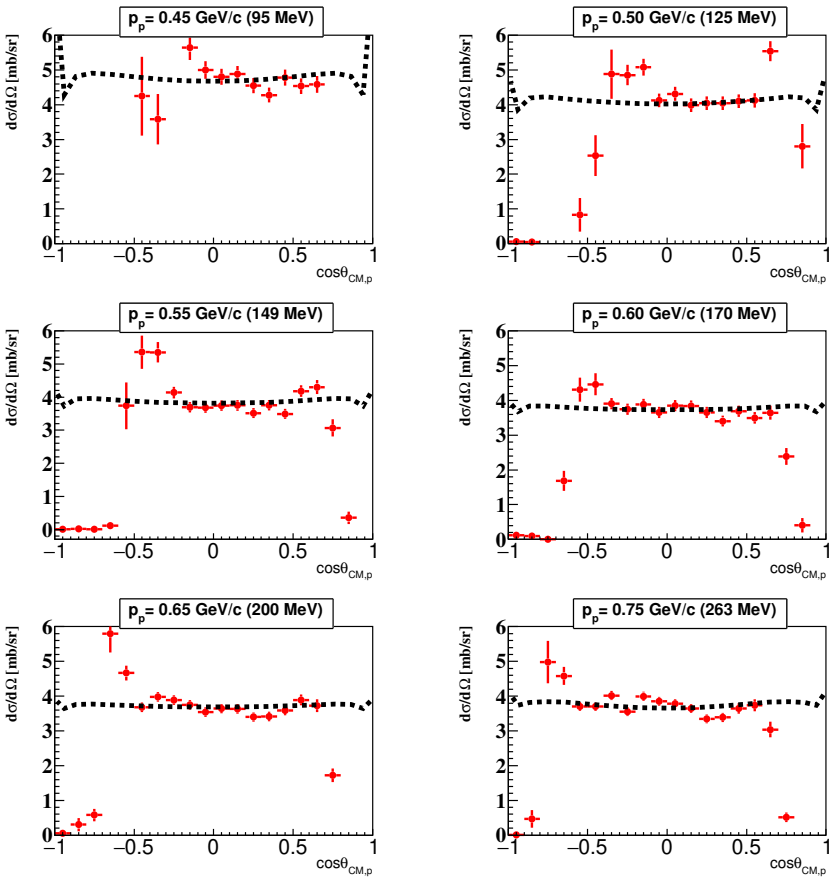

Figure 6.5: Typical differential cross sections of pp scattering derived from proton beam data. The red points represents the derived ones, and the black dotted line shows the calculated ones by ESC96 using calculator on [57].

To estimate the efficiency uncertainty at the acceptance edge, the possible lowest and highest CFT tracking efficiencies were also made by changing the parameters within a reasonable range, i.e., changing d within 20% and E_{half} within 4 MeV. The validity of the margin of efficiency defined by the lowest and highest cases was additionally verified using another calibration reaction. This calibration reaction was that of pp scattering following the $\Sigma^+ \to p\pi^0$ decay, which described in Subsection 5.2.2. From the data analysis, the angular distribution of the recoil proton was obtained, shown by the red points in Figure 6.6. This angular distribution was compared with a Monte Carlo simulation, including the secondary pp scattering process with a realistic angular distribution. While analyzing the simulated data, the data-based CFT tracking efficiencies for the lowest and highest cases were considered. The angular distribution in the data was sandwiched between the two distributions estimated using the highest and lowest efficiencies, as shown by the blue and green points in Figure 6.6. In the next subsection, the detection efficiency for $\Sigma^+ p$ scattering was corrected using these two efficiencies, and the difference was considered to be the systematic uncertainty.

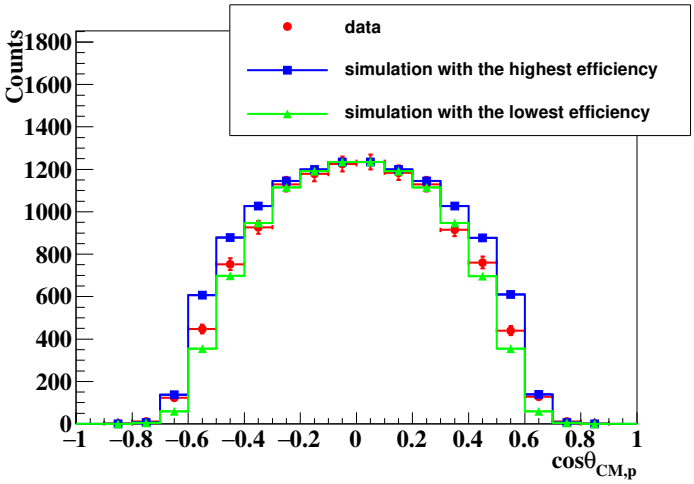

Figure 6.6: Angular distribution of the protons from the pp scattering following the $\Sigma^+ \to p\pi^0$ decay events. The red points represent the data. The green and blue points show the simulation results with the efficiency correction using the possible lowest and highest CFT tracking efficiencies, respectively. The simulations are normalized by the counts at $0 < \cos\theta_{\mathrm{CM},p} < 0.1$.

6.3.2 Average efficiency for the $\Sigma^+ p$ scattering events considering the real detection efficiency

The average efficiency $\bar{\varepsilon}$ for the $\Sigma^+ p$ scattering events, including the detection and analysis efficiencies, was evaluated by analyzing the simulated data with the same analyzer program for the real data. $\bar{\varepsilon}$ is defined as follows:

$$\begin{aligned}\bar{\varepsilon}(p_\Sigma, \cos\theta_{\mathrm{CM}}) &= \frac{N_{\mathrm{analyzed}}(p_\Sigma, \cos\theta_{\mathrm{CM}})}{N_{\mathrm{generated},\Sigma^+\mathrm{id}}(p_\Sigma, \cos\theta_{\mathrm{CM}})} \qquad (6.4)\\ &= \frac{N_{\mathrm{detected}}(p_\Sigma, \cos\theta_{\mathrm{CM}})}{N_{\mathrm{generated},\Sigma^+\mathrm{id}}(p_\Sigma, \cos\theta_{\mathrm{CM}})} \cdot \frac{N_{\mathrm{analyzed}}(p_\Sigma, \cos\theta_{\mathrm{CM}})}{N_{\mathrm{detected}}(p_\Sigma, \cos\theta_{\mathrm{CM}})}\\ &= \bar{\varepsilon}_{\mathrm{detect}}(p_\Sigma, \cos\theta_{\mathrm{CM}}) \cdot \bar{\varepsilon}_{\mathrm{ana}}(p_\Sigma, \cos\theta_{\mathrm{CM}}). \qquad (6.5)\end{aligned}$$

$N_{\mathrm{generated},\Sigma^+\mathrm{id}}$ in Equation (6.4) represents the number of generated $\Sigma^+ p$ scattering events in the simulation. Σ^+ identification from missing mass analysis in the analyzer program is required. N_{analyzed} represents the number of identified two-proton $\Sigma^+ p$ scattering events that satisfy all cut conditions for $\Sigma^+ p$ scattering. The effect of the branching ratio of the $\Sigma^+ \to p\pi^0$ decay is also included in N_{analyzed}. $\bar{\varepsilon}$ is factorized by the detection efficiency in CATCH, $\varepsilon_{\mathrm{detect}}$, and the analysis cut efficiency, $\varepsilon_{\mathrm{ana}}$, from the second equation. N_{detected} represents the number of two-proton events in the Σ^+ identification events. The difference in the CFT tracking efficiency between the data, $\varepsilon^{\mathrm{data}}_{\mathrm{CFT}}$, and simulation, $\varepsilon^{\mathrm{sim}}_{\mathrm{CFT}}$, was corrected by changing $\bar{\varepsilon}_{\mathrm{detect}}$ as follows:

$$\bar{\varepsilon}_{\mathrm{detect}} \mapsto \frac{1}{N_{\mathrm{generated},\Sigma^+\mathrm{id}}} \left(\sum_{\mathrm{events}}^{N_{\mathrm{detected}}} \frac{\varepsilon^{\mathrm{data}}_{\mathrm{CFT}}(\theta_{p_1}, E_{\mathrm{cal},p_1}, z_{\mathrm{scat}}) \cdot \varepsilon^{\mathrm{data}}_{\mathrm{CFT}}(\theta_{p_2}, E_{\mathrm{cal},p_2}, z_{\mathrm{decay}})}{\varepsilon^{\mathrm{sim}}_{\mathrm{CFT}}(\theta_{p_1}, E_{\mathrm{cal},p_1}, z_{\mathrm{scat}}) \cdot \varepsilon^{\mathrm{sim}}_{\mathrm{CFT}}(\theta_{p_2}, E_{\mathrm{cal},p_2}, z_{\mathrm{decay}})} \right), \qquad (6.6)$$

where the efficiency correction for both protons was considered. The analysis cuts are explained in Section 5.3; and the analysis efficiency for the entire angular region is summarized in Table 5.1. Here, the analysis efficiency was estimated for each scattering angle. The evaluated efficiencies are shown in Figure 6.7. The vertical error represents the difference between the lowest and highest possible CFT tracking efficiencies, as mentioned in the previous subsection. The angular dependence of the efficiency can be understood from the kinetic energies of protons. The efficiency decreases for the forward scattering angle, because the tracking efficiency also decreases for recoil protons with a lower kinetic energy. Similarly, the kinetic energy of the decay proton decreases for the backward angle, and the efficiency therefore decreases for the backward angle. The errors in the efficiency were considered as systematic errors in deriving differential cross sections.

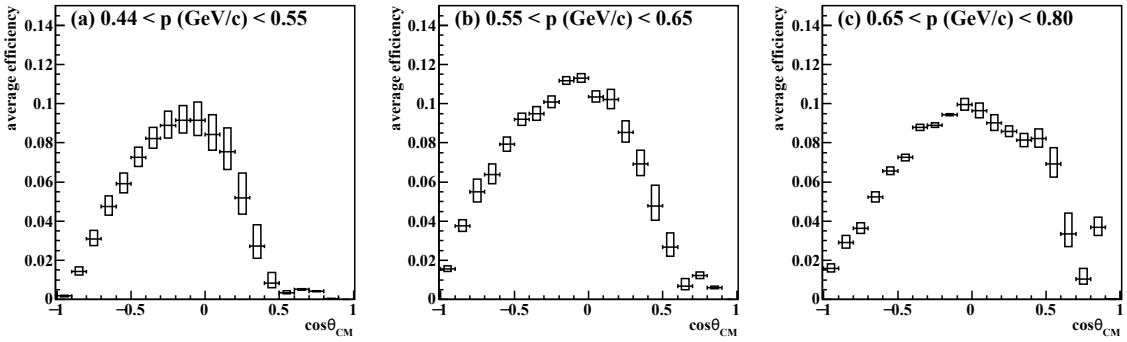

Figure 6.7: Average efficiencies for the $\Sigma^+ p$ scattering for each scattering angle and momentum region. The vertical error represents the difference in the obtained efficiency using the two possible lowest and highest CFT tracking efficiencies.

Chapter 7

Experimental result and discussion

7.1 Differential cross sections

The differential cross section was calculated using Eq. (6.1). The obtained differential cross sections for the three incident Σ^+ momentum regions are shown as black circles in Figure 7.1. The mean momenta of the three momentum regions are 0.50, 0.59, and 0.71 GeV/c, respectively. The error bars and boxes of the data points represent statistical and systematic uncertainties, respectively. The systematic error was estimated as the quadratic sum of the error from the background estimation, average efficiency, and Σ^+ total flight length. The data has small uncertainty typically less than 20% and a fine angular step of $\Delta \cos\theta = 0.1$. The values of the differential cross sections and their uncertainties are summarized in Tables A.1, A.2, and A.3 in Appendix A.

7.2 Comparison with the past experiments and theoretical calculations

The differential cross sections obtained from present experiments are shown as black circles in Figure 7.1. For the lower two momentum regions, past measurements at KEK PS are plotted with red boxes [24] and blue triangles [26] in Figure 7.1. The data quality in the present experiment was improved significantly. Thus, a meaningful comparison with theories has become possible.

Theoretical calculations were overlaid as lines in Figure 7.1. The blue dotted and dot-dashed lines show the calculations from the FSS and fss2 models [19], which include the QCM in the short-range region and naturally incorporate the quark Pauli effect. Therefore, the comparison with these models is important for the verification of the quark Pauli effect, which is an important motivation for this experiment. The difference between the two models is mainly caused by the different size parameter, which defines the harmonic oscillator wave functions of quarks in the baryons and determines the strength of the quark Pauli effect. The FSS model, using the larger size parameter, predicts a strong repulsive interaction, which increases the differential cross section. However, the predictions by FSS and fss2 are much larger than the present data, indicating that the repulsive forces in FSS and fss2 are too large and unrealistic. After the parameter tuning of these models using our precise data, the QCM picture itself will be validated.

The green solid and black-dashed lines show the predictions from the Nijmegen NSC97f

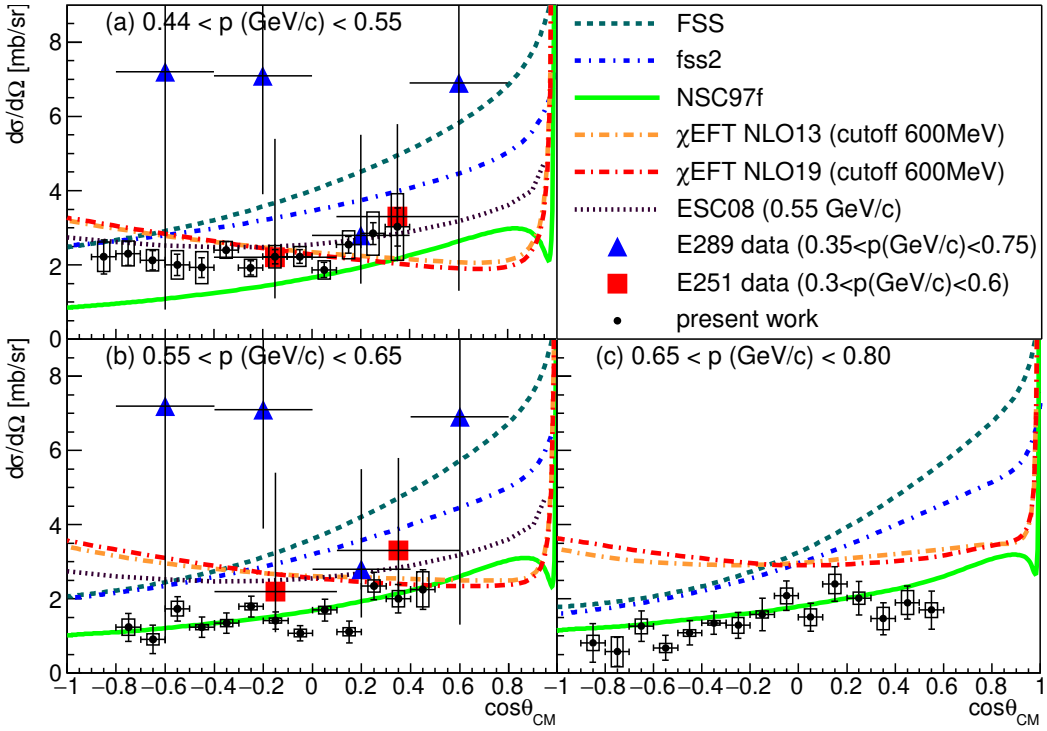

Figure 7.1: Derived differential cross sections of the Σ^+p scattering for the three momentum regions. The error bars and boxes show the statistical and systematic uncertainties, respectively. The red boxes and blue triangles represent the data of past measurements, KEK E251 [24] and KEK E289 [26], respectively. The blue dotted and dot-dashed lines show the calculations from FSS and fss2 [19], respectively. The green-solid lines and black-dashed lines show the calculations from the Nijmegen NSC97f [14] and ESC08 [15] models, respectively. The orange and red dot-dashed lines show the calculations from the χEFT NLO models [17] [18].

[14] and ESC08 [15] models, respectively, based on the boson-exchange picture. Historically, in the Nijmegen models, it has been difficult to describe the repulsive nature of the $\Sigma N(I = 3/2, {}^3S_1)$ channel. Although NSC97f agrees well with our data in terms of the differential cross sections, it predicts an attractive Σ^+p interaction, which does not agree with the current common understanding of the ΣN interaction. In ESC08, additional repulsive effects, including the quark picture, are considered by making an effective Pomeron potential as the sum of a pure Pomeron exchange and a Pomeron-like representation of the Pauli repulsion. Subsequently, ESC08 predicts a moderate repulsive force within this channel. Although there were sizable discrepancies between our data and ESC08, especially in the middle-momentum region, ESC08 was closer to present data than fss2. This suggests that the size of the repulsive force used in ESC08 is relatively reasonable.

The orange and red dot-dashed lines show the calculations using the χEFT models extended to the YN sector (NLO13 [17] and NLO19 [18], respectively), which use different sets of LECs. In both cases, a cutoff value of 600 MeV was used. The LECs are essential parameters of the χEFT models, representing the short-range part of the interaction, and should be determined from the experimental data. At present, the LECs for S waves have

been determined based on existing hyperon-proton scattering data in the low-momentum region. However, the LECs for P waves have not been well-constrained owing to the lack of experimental data for the momentum region around the present data. At present, χEFT predicts much larger cross sections, especially in the higher-momentum region. LECs for P waves in the χEFT models will be determined using our data, which may make at least angular dependences closer to our data.

For the first time, we presented precise data for the Σ^+p channel in the higher-momentum range than 0.4 GeV/c. Currently, no theoretical model can reproduce our data consistently for the three momentum regions. This was mainly because of the lack of precise data. Therefore, our data are essential inputs for improving these theoretical calculations in order to become realistic BB interaction models.

7.3 Phase-shift analysis

Extracting the contribution of the $^3S_1$ states from the differential cross section data is important to study the repulsive nature of Σ^+p system related to the quark Pauli effect. For this purpose, a phase-shift analysis was performed based on a general formulation of the scattering problem in quantum mechanics. This was the first application to hyperon-nucleon scattering data, whereas precise phase-shift analysis has been performed for the NN scattering data to derive the phase shifts for each partial wave [58].

7.3.1 Specific expressions of differential cross section as a function of phase shifts

Similarly to the NN scattering case [59], an asymptotic form of the wave function for the Σ^+p scattering can be written as follows:

$$\psi^{s'}_{m'}(\boldsymbol{r}) \sim e^{ikz}\xi^{s'}_{m'} + \frac{e^{ikr}}{r}\sum_{s,m}\xi^{s}_{m}M^{s,s'}_{m,m'}(\theta,\phi) \tag{7.1}$$

where k represents the wavenumber of relative motion in the CM system defined as $k = p_{\rm CM}/\hbar$, ξ^s_m denotes the spin state with spin quantum number s and the projection on the quantization axis m. $M^{s,s'}_{m,m'}$ are the matrix elements of the spin-1/2 spin-1/2 scattering amplitude with a polar angle θ and azimuthal angle ϕ. By the partial-wave decomposition, the matrix element becomes

$$\begin{aligned} M^{s,s'}_{m,m'}(\theta,\phi) = \sum_{L}\sum_{J=|L-s|}^{L+s}\sum_{L'=|J-s'|}^{J+s'} & \sqrt{4\pi(2L'+1)}Y_L^{m'-m}(\theta,\phi) \\ & \times C_{L\times s}(J,m',m'-m,m)C_{L'\times s'}(J,m',0,m')i^{L'-L}\frac{\langle L,s|\,S^{\rm mat}-1\,|L',s'\rangle}{2ik} \end{aligned} \tag{7.2}$$

where the $C_{L\times s}$ are Clebsch-Gordan coefficients defined as

$$C_{L\times s}(J,m_J,m_L,m_s) = \langle Lm_Lsm_s|LsJm_J\rangle\,,$$

and Y_L^m is a spherical harmonic, and $S^{\rm mat}$ is the scattering matrix. The differential cross section for scattering of an unpolarized incident particle on an unpolarized target I_0 is expressed by the matrix elements as follows:

$$I_0 = \frac{1}{4}|M^{0,0}_{0,0}|^2 + \frac{1}{2}|M^{1,1}_{1,1}|^2 + \frac{1}{4}|M^{1,1}_{0,0}|^2 + \frac{1}{2}|M^{1,1}_{0,1}|^2 + \frac{1}{2}|M^{1,1}_{1,0}|^2 + \frac{1}{2}|M^{1,1}_{1,-1}|^2. \tag{7.3}$$

The explicit formulae of the matrix elements as a function of the partial wave amplitudes h's for a general angular momentum L can be found in Ref. [60]. The specific expressions up to D wave ($L \leq 2$) are described as follows:

$$M^{0,0}_{0,0} = h_{^1S_0} + 3h_{^1P_1}\cos\theta + 5h_{^1D_2} \times \Big(\frac{3\cos^2\theta - 1}{2}\Big), \tag{7.4}$$

$$M^{1,1}_{1,1} = \Big(h_{^3S_1} - \frac{\sqrt{2}}{2}h^{^3S_1-{}^3D_1}\Big) + \Big(\frac{3}{2}h_{^3P_2} + \frac{3}{2}h_{^3P_1}\Big)\cos\theta + \Big(2h_{^3D_3} + \frac{5}{2}h_{^3D_2} + \frac{1}{2}h_{^3D_1} - \frac{\sqrt{2}}{2}h^{^3S_1-{}^3D_1}\Big) \times \frac{3\cos^2\theta - 1}{2}, \tag{7.5}$$

$$M^{1,1}_{0,0} = (h_{^3S_1} + \sqrt{2}h^{^3S_1-{}^3D_1}) + (2h_{^3P_2} + h_{^3P_0})\cos\theta + (3h_{^3D_3} + 2h_{^3D_1} + \sqrt{2}h^{^3S_1-{}^3D_1}) \times \frac{3\cos^2\theta - 1}{2}, \tag{7.6}$$

$$M^{1,1}_{0,1} = \Big(-\frac{3}{2\sqrt{2}}h_{^3P_2} + \frac{3}{2\sqrt{2}}h_{^3P_1}\Big) \times (-\sin\theta) + \Big(-\frac{4}{3\sqrt{2}}h_{^3D_3} + \frac{5}{6\sqrt{2}}h_{^3D_2} + \frac{1}{2\sqrt{2}}h_{^3D_1} - \frac{1}{\sqrt{2}}h^{^3S_1-{}^3D_1}\Big) \times (-3\cos\theta\sin\theta), \tag{7.7}$$

$$M^{1,1}_{1,0} = \Big(\frac{1}{\sqrt{2}}h_{^3P_2} - \frac{1}{\sqrt{2}}h_{^3P_0}\Big) \times (-\sin\theta) + \Big(\frac{1}{\sqrt{2}}h_{^3D_3} - \frac{1}{\sqrt{2}}h_{^3D_1} - \frac{1}{\sqrt{2}}h^{^3S_1-{}^3D_1}\Big) \times (-3\cos\theta\sin\theta), \tag{7.8}$$

$$M^{1,1}_{1,-1} = \Big(\frac{1}{6}h_{^3D_3} - \frac{5}{12}h_{^3D_2} + \frac{1}{4}h_{^3D_1} - \frac{1}{2\sqrt{2}}h^{^3S_1-{}^3D_1}\Big) \times (3\sin^2\theta), \tag{7.9}$$

where partial wave amplitudes h's were defined as

$$h_{^{2s+1}L_J} = \begin{cases} \frac{1}{2i\bar{k}}(\cos(2\bar{\epsilon}_1)\exp(2i\bar{\delta}_{^{2s+1}L_J}) - 1) & (^3S_1 \text{ and } {}^3D_1 \text{ cases}) \\ \frac{1}{2i\bar{k}}(\exp(2i\bar{\delta}_{^{2s+1}L_J}) - 1) & (\text{otherwise}) \end{cases} \tag{7.10}$$

$$h^{^3S_1-{}^3D_1} = \frac{1}{2k}\sin(2\bar{\epsilon}_1)\exp(i\bar{\delta}_{^3S_1} + i\bar{\delta}_{^3D_1}). \tag{7.11}$$

$\bar{\delta}_{^{2s+1}L_J}$ and $\bar{\epsilon}_1$ are the bar-phase shifts and mixing parameter for the $^3S_1 - {}^3D_1$ mixing. In a precise sense, bar-phase shifts are different from commonly-used nuclear bar-phase shifts, in which Coulomb effects were subtracted. Because the energies of the Σ^+p scattering are sufficiently high and the data for very-forward angle is absent, the Coulomb effects might be negligible. Therefore, the bar-phase shifts were equated with the nuclear bar-phase shifts and called merely "phase shifts δ" in the following.

In this way, the differential cross sections can be represented as a function of the phase shifts, scattering angle $\theta_{\rm CM}$, and momentum $p_{\rm CM}$ in the CM system. Here, the triplet-even and singlet-odd states of the Σ^+p system are expressed by the 10-plet of the flavor SU(3) multiplets and the other states are expressed by the 27-plet as shown in Table 1.1.

Therefore, this function is denoted by $I_0(\theta_{\rm CM}, p_{\rm CM}, \boldsymbol{\delta}_{[27]}, \boldsymbol{\delta}_{[10]})$. In present analysis, partial waves up to D are considered. The phase shifts for the 27-plet are taken up to five spin states: $\boldsymbol{\delta}_{[27]} = \{\delta_{^1S_0}, \delta_{^3P_2}, \delta_{^3P_1}, \delta_{^3P_0}, \delta_{^1D_2}\}$. For the 10-plet, five phase shifts and a mixing parameter for $^3S_1$-$^3D_1$ mixing, that is, $\boldsymbol{\delta}_{[10]} = \{\delta_{^3S_1}, \delta_{^1P_1}, \delta_{^3D_3}, \delta_{^3D_2}, \delta_{^3D_1}, \epsilon_1\}$, are included.

7.3.2 Consideration of the fixed phase shifts in the fitting

The function $I_0(\theta_{\rm CM}, p_{\rm CM}, \boldsymbol{\delta}_{[27]}, \boldsymbol{\delta}_{[10]})$ has 11 phase-shift parameters. Because a fitting with 11 free parameters results in a large ambiguity for each parameter, the number of free parameters should be reduced by fixing some of them to reasonable values.

The phase shifts $\boldsymbol{\delta}_{[27]}$ can be reliably constrained because $\boldsymbol{\delta}_{[27]}$ becomes identical to the phase shifts in the $NN(I = 1)$ channel in the limit of flavor SU(3) symmetry. In this limit, $\boldsymbol{\delta}_{[27]}$ can be obtained from the phase shifts of pp scattering for the corresponding momentum. However, in reality, $\boldsymbol{\delta}_{[27]}$ in the Σ^+p scattering should be slightly different from that in the pp scattering, owing to the breaking of flavor symmetry. In fact, all theories (FSS, fss2, ESC, and NSC97f) predict smaller $^1S_0$ phase shifts in Σ^+p scattering than those in pp scattering. However, the difference between the theoretical predictions of $\boldsymbol{\delta}_{[27]}$ is small because these models are also constrained by pp scattering data. In this analysis, the effect of the uncertainty in $\boldsymbol{\delta}_{[27]}$ was examined using three different sets of $\boldsymbol{\delta}_{[27]}$. The phase-shift values of pp scattering and theoretical predictions in ESC16 [22] and NSC97f [14] were used in this study.

In contrast, the phase shifts $\boldsymbol{\delta}_{[10]}$ are unique to the $\Sigma N(I = 3/2)$ channel, and these phase shifts should be determined from the fitting. The theoretically uncertain two phase shifts $\delta_{^3S_1}$ and $\delta_{^1P_1}$, representing the short-range interaction, were regarded as free parameters. For the remaining phase shifts, namely $\delta_{^3D_3}, \delta_{^3D_2}, \delta_{^3D_1}$, and ϵ_1, the variation among the theoretical models is rather small because the pion-exchange mechanism is expected to be dominant for the momentum range of present experiment. Therefore, these phase shifts were fixed at the theoretical values as an approximation.

In summary, the two phase-shift parameters, $\delta_{^3S_1}$ and $\delta_{^1P_1}$, were obtained by fitting the differential cross sections with the function $I_0(\theta_{\rm CM}, p_{\rm CM}, \boldsymbol{\delta}_{[27]}, \boldsymbol{\delta}_{[10]})$. To study the difference of the results due to the fixed parameter sets, fitting was performed for three conditions with different fixed parameter sets.

A $\boldsymbol{\delta}_{[27]}$ was fixed at values taken from the pp scattering. $\delta_{^3D_3}, \delta_{^3D_2}, \delta_{^3D_1}$, and ϵ_1 were fixed at 0.

B $\boldsymbol{\delta}_{[27]}$ was fixed at values from the ESC16 or NSC97f models. $\delta_{^3D_3}, \delta_{^3D_2}, \delta_{^3D_1}$, and ϵ_1 were fixed at 0.

C $\boldsymbol{\delta}_{[27]}$ was fixed at values from the ESC16 or NSC97f models. $\delta_{^3D_3}, \delta_{^3D_2}, \delta_{^3D_1}$, and ϵ_1 were fixed at the values from ESC16 or NSC97f.

Although the sign of $\delta_{^3S_1}$ is expected to be negative, as predicted by recent theoretical models including ESC16, numerical fittings with a positive $\delta_{^3S_1}$ are possible, which can be roughly understood from the fact that differential cross sections would be proportional to $(\sin\delta_0/k)^2$ in the S-wave limit. To investigate the negative and positive $\delta_{^3S_1}$ cases, two different sets of fixed parameters from ESC16 and NSC97f, respectively, were examined. The fixed phase shifts are presented in Table 7.1.

Table 7.1: $\boldsymbol{\delta}_{[27]}$ and $\boldsymbol{\delta}_{[10]}$ for the pp scattering and Σ^+p scattering in ESC16 [22] and NSC97f [14], respectively. The units of p_Σ and $p_{\rm CM}$ are [GeV/c]. $E^{pp}_{\rm lab}$ (unit: [MeV]) represents the kinetic energy of the beam proton in the pp scattering in which $p_{\rm CM}$ is equal to that of the Σ^+p scattering. The units of phase shifts are [°].

	low			mid			high		
	pp	ESC16	NSC97f	pp	ESC16	NSC97f	pp	ESC16	NSC97f
p_Σ	0.496	0.50	0.50	0.59	0.60	0.60	0.71	0.70	0.70
$p_{\rm CM}$	0.214	0.216	0.216	0.253	0.257	0.257	0.303	0.297	0.297
$E^{pp}_{\rm lab}$	87.6	–	–	122.1	–	–	173.7	–	–
$\delta_{^1S_0}$	27.9	19.1	20.2	19.5	10.8	11.8	10.4	2.80	3.71
$\delta_{^3P_2}$	9.92	6.76	6.44	12.7	8.50	8.02	14.9	9.82	9.04
$\delta_{^3P_1}$	−12.2	−13.2	−13.3	−15.5	−16.9	−17.1	−19.5	−20.8	−21.0
$\delta_{^3P_0}$	10.5	7.19	8.10	7.29	3.59	4.49	2.15	−0.92	−0.23
$\delta_{^1D_2}$	3.24	3.38	3.25	4.71	4.99	5.02	6.41	6.61	6.99
$\delta_{^3S_1}$	–	(−27.9)	(21.9)	–	(−32.6)	(28.5)	–	(−36.6)	(35.01)
$\delta_{^1P_1}$	–	(8.33)	(12.2)	–	(8.45)	(13.71)	–	(7.46)	(13.7)
$\delta_{^3D_3}$	–	1.14	1.42	–	1.59	2.29	–	1.93	3.18
$\delta_{^3D_2}$	–	−3.53	−3.23	–	−4.87	−4.23	–	−6.42	−5.31
$\delta_{^3D_1}$	–	1.35	1.48	–	0.69	1.30	–	−0.70	0.41
ϵ_1	–	−5.04	−1.65	–	−5.24	0.11	–	−5.14	1.87

7.3.3 Fitting results and phase shifts of $^3S_1$ and $^1P_1$ states

The fitting results in the three momentum regions are shown in Figure 7.2, 7.3, and 7.4. In all momentum regions, reasonable reduced χ^2 values of approximately one were obtained. The momentum dependencies of the obtained $\delta_{^3S_1}$ and $\delta_{^1P_1}$ values are plotted in Figure 7.5. The absolute values of $\delta_{^3S_1}$ for the low-, middle-, and high-momentum regions were $(28.3\pm1.5\pm2.1)^\circ$, $(23.4\pm2.0\pm3.0)^\circ$, and $(32.5\pm2.5\pm2.5)^\circ$, respectively. The former error comes from the fitting error and the latter reflects the effect of the different fixed parameters. If the sign is assumed to be negative, the momentum dependence of $\delta_{^3S_1}$ is consistent with the ESC16 model, suggesting that the repulsive force is moderate as in the ESC models, as discussed in section 7.2. In contrast, the obtained $\delta_{^1P_1}$ values deviate considerably in the range of $-5^\circ < \delta_{^1P_1} < 25^\circ$ depending on the conditions. Although the results of $\delta_{^1P_1}$ are ambiguous, they may support the predictions of fss2, ESC, and NSC97f, in which the interaction of the $^1P_1$ state in the Σ^+p system is weakly attractive.

By exploiting high-quality differential cross section data and the simple representation of Σ^+p interaction in the flavor SU(3) symmetry, we succeeded to determine the $\delta_{^3S_1}$ value with a small error less than 4 degrees. This result will impose a strong constraint on the size of the repulsive force in the Σ^+p systems.

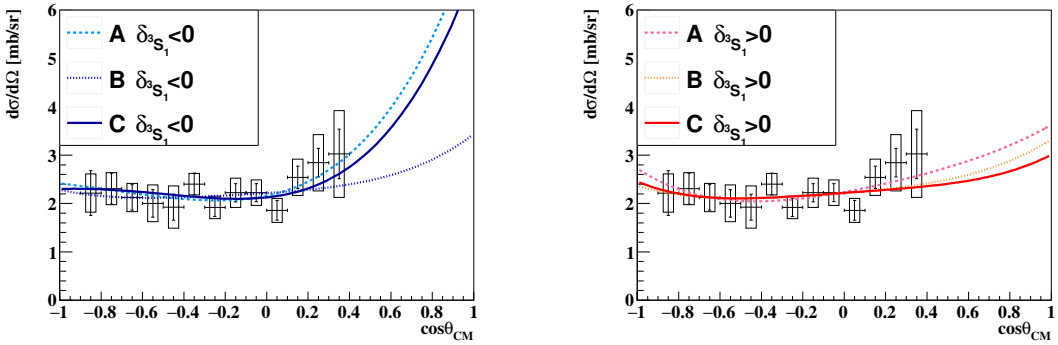

Figure 7.2: Differential cross sections as a function of the scattering angle together with the calculated angular distribution in the phase-shift analyses for the low-momentum region ($0.44 < p_\Sigma[\mathrm{GeV}/c] < 0.55$) in (Left) the negative $\delta_{^3S_1}$ case and (Right) the positive case. Three lines in each graph show the fitting results with three different fitting conditions A, B, and C, as described in the text. The typical χ^2/ndf is 4.4/11.

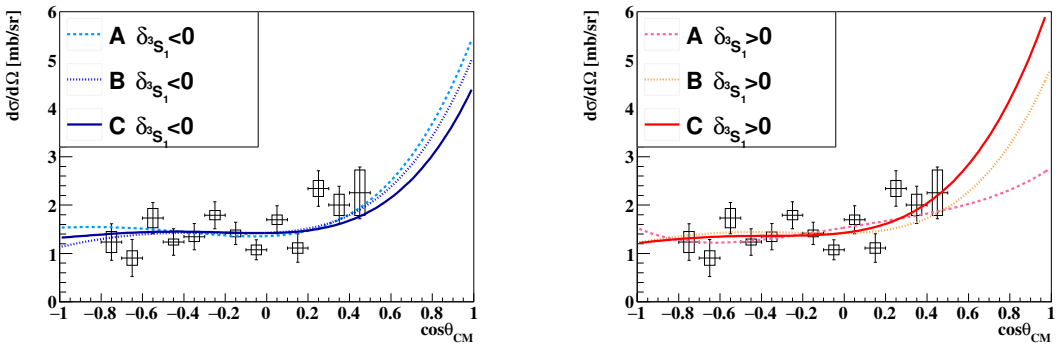

Figure 7.3: Differential cross section as a function of the scattering angle together with the calculated angular distribution in the phase-shift analysis for the middle-momentum region ($0.55 < p_\Sigma[\mathrm{GeV}/c] < 0.65$). The fitting conditions are the same as in Figure 7.2. The typical χ^2/ndf is 14.0/11.

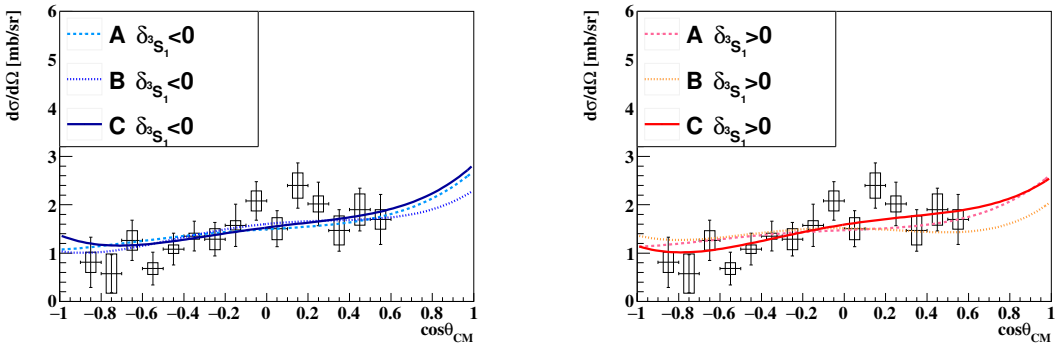

Figure 7.4: Differential cross section as a function of the scattering angle together with the calculated angular distribution in the phase-shift analysis for the high-momentum region ($0.65 < p_\Sigma[\mathrm{GeV}/c] < 0.80$). The fitting conditions are the same as in Figure 7.2. The typical χ^2/ndf is 11.0/13.

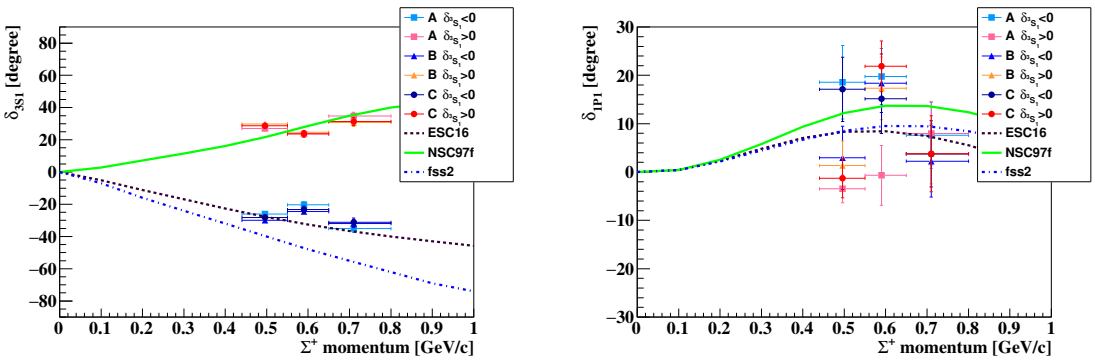

Figure 7.5: Obtained phase shifts $\delta_{^3S_1}$ and $\delta_{^1P_1}$ as a function of the incident momentum. The black-dashed, green-solid, and blue-dotted lines represent the calculated phase shifts of ESC16 [22], NSC97f [14], and fss2 [19], respectively.

Chapter 8

Summary

For the systematic understanding of the baryon-baryon interactions between octet baryons, revealing the nature of flavor SU(3) multiplets is important. Among them, the 10-plet is predicted to be considerably repulsive due to the Pauli effect in the quark level, which is related to the origin of the repulsive core in the nuclear force. The $\Sigma N(I = 3/2)$ channel is one of the best channels to study the repulsive nature in the 10-plet. However, the theoretical predictions for strengths of the repulsive force differ from each other and the reliable experimental inputs are needed to point out the strength. Hyperon-proton scattering experiment is one of the most direct methods to study the YN interaction, as in the case of the NN interaction. Although it was experimentally difficult due to short lifetime of hyperons for a long time, we successfully performed novel high-statistics $\Sigma^{\pm}p$ scattering experiment at J-PARC (J-PARC E40). In this experiment, we measured the differential cross sections of not only the Σ^+p elastic scattering but also the Σ^-p elastic and $\Sigma^-p \to \Lambda n$ inelastic scatterings. In this thesis, the data taking and detailed results of the Σ^+p elastic scattering experiment to investigate the $\Sigma N(I = 3/2)$ interaction were reported.

The experiment was performed at the K1.8 beam line in the J-PARC Hadron Experimental Facility in the separated periods of April 2019 and May-June 2020 for the data collection of the Σ^+p scattering. The π^+ beam, having a high intensity of approximately 2×10^7/spill and the central momentum of 1.41 GeV/c, was used to produce many Σ^+ particles inside the LH_2 target via the $\pi^+p \to K^+\Sigma^+$ reaction. The produced Σ^+ was momentum-tagged from the beam π^+ and outgoing K^+, which were analyzed using the beam-line and forward spectrometers, respectively. In total, 4.9×10^7 Σ^+ were tagged and these Σ^+, traveling inside the LH_2 target, were regarded as the incident particle for Σ^+p scattering. The recoil proton from Σ^+p scattering were detected using the surrounding detector system CATCH. Σ^+p scattering events were identified by checking the consistency for the recoil proton between the measured energy and the calculated energy from kinematics of the Σ^+p scattering. In total, approximately 2400 Σ^+p elastic scattering events were identified in the momentum range 0.44 – 0.80 GeV/c.

The differential cross sections of the Σ^+p scattering were derived for the three separated-momentum regions. Their uncertainties were typically less than 20% with an angular step of $\Delta \cos\theta_{\rm CM} = 0.1$, and the data quality was drastically improved. The angular dependences of the obtained differential cross sections are rather isotropic for the present angular regions of $-0.8 < \cos\theta_{\rm CM} < 0.6$, especially for the low momentum. The obtained values of the differential cross sections are around 2 mb/sr, which are not so large as predicted

by the fss2 and FSS based on the QCM in the short-range region [19], which naturally incorporate the quark Pauli effect. The Nijmegen ESC models [15][22], which include the moderate repulsive force by the Pomeron effect and phenomenological treatment of the quark Pauli effect, were close to the data. χEFT predicts much larger cross sections, especially at the higher momentum region. We expect that our data will be used to specify the LECs especially for P-waves in the χEFT models [17][18].

Owing to precise data points and the simple representation of the Σ^+p system with respect to the multiplets of the BB interaction, we derived the phase shifts of the $^3S_1$ and $^1P_1$ states by performing the phase-shift analysis for the obtained differential cross sections. This is the first-time application to hyperon-nucleon scattering data. In this analysis, the less uncertain phase shifts were fixed to the reasonable values and two important phase shifts, $\delta_{^3S_1}$ and $\delta_{^1P_1}$, were determined by the fitting. The $\delta_{^3S_1}$, which is closely related to the strength of repulsive force due to the quark Pauli effect was determined with a small error of approximately 4 degrees for each of the momentum regions. The absolute values of $\delta_{^3S_1}$ ranges 20° to 35° for the present momentum range. If the sign is assumed to be negative, the momentum dependence of the $\delta_{^3S_1}$ is rather consistent with ESC16, suggesting that the repulsive force is moderate like ESC16. Because theoretical models describing BB interaction has been built on little hyperon-proton scattering data, our data will be an essential input for making them realistic.

Acknowledgements

Owing to many helps of numerous people, I could finish the data taking of J-PARC E40 experiment and finally summarize results in this thesis. I would like to express my gratitudes here.

First of all, I'm very grateful to my supervisor, Prof. Tomofumi Nagae. He was one of the first person to teach me nuclear physics and the joy of experiment when I was an undergraduate student. After I got into graduate school, he led me into an interesting research field, strangeness nuclear physics. I learned many things in working for his project, the spectroscopic study of Ξ hypernuclei at J-PARC. After I changed my research theme to $\Sigma^{\pm}p$ scattering experiment, he watched over me and gave me a lot of sound advice.

I also deeply appreciate Prof. Koji Miwa, who is the spokes person of the J-PARC E40 experiment. He gave me a precious opportunity to conduct the $\Sigma^{+}p$ data taking and analyze the $\Sigma^{+}p$ scattering channel, which is the flagship channel of the J-PARC E40 experiment. He managed the whole of experiment and got the funding resources as a spokes person. Moreover, he was always at the forefront of all stages of experiment: R&D, preparation, data taking, and analysis. The paper for the $\Sigma^{-}p$ elastic scattering and the $\Sigma^{-}p \to \Lambda n$ inelastic scattering were written by him. In this way, he showed me an ideal images of a researcher. He made many essential comments on the analysis and writing of the published academic paper and this thesis.

I am thankful to "Research Group for Hadron nuclear physics" in Advanced Science Research Center of Japan Atomic Energy Agency (JAEA-ASRC) for accepting me as a granted student for four years and a research assistant for one year. Without this financial support, I could not survive my long doctoral course of six years. Prof. Hiroyuki Sako, the group manager, provided this research enviroment. Prof. Kiyoshi Tanida and Dr. Yudai Ichikawa gave me advice on many things from daily life in Tokai village to research as host researchers. The research group for hadron nuclear physics have a close relation ship with "Advanced Theoretical Physics group" in JAEA-ASRC. Especially, Prof. Makoto Oka, who is the pioneer of the quark cluster model, always encouraged me. Prof. Toshiki Maruyama gave me a hand-me-down car, which made my quality of life in Tokai village much better.

I would like to thank all the K1.8 beam line members and collaborators of J-PARC E40 experiment. We help each other to carry out many experiments in the beam line. Their help was essential in J-PARC E40 experiment and I learned many things about detectors and experimental systems through joining other experiments. Among them, I want to express my special thanks to E40 core members, shift members in the $\Sigma^{+}p$ data taking in 2020 May-June, and students of Prof. K. Miwa.

I discussed many things about experiments, analysis, and writing of the paper in weekly meetings and e-mails with J-PARC E40 core members, Prof. K. Miwa, Prof.

Toshiyuki Takahashi, Prof. Ryotaro Honda, Dr. Yuya Akazawa, Dr. Shuhei Hayakawa, Dr. Mifuyu Ukai, Dr. Takeshi O Yamamoto, Mr. Yoshiyuki Nakada, Ms. Norina Fujioka, Mr. Suharu Hoshino, Mr. Kunpei Matsuda, Mr. Ryohei Nagatomi, Mr. Tomomasa Kitaoka, Ms. Tamao Sakao, Mr. Shunsuke Wada, Mr. Taito Morino and Mr. Kazuma Ohashi. Discussions with them were very fruitful.

The latter half of the $\Sigma^+ p$ data taking was performed in 2020 May-June, when there was the severe movement restriction due to COVID-19. Therefore, shift members, Prof. K. Miwa, Prof. T. Takahashi, Prof. K. Tanida, Dr. Y. Akazawa, Dr. Manami Fujita, Dr. S. H. Hayakawa, Dr. Y. Ichikawa, Dr. M. Ukai , Dr. T. O. Yamamoto, Mr. Yuji Ishikawa, Ms. Honoka Kanauchi, Mr. T. Kitaoka, Mr. S. Wada, and Ms. T. Sakao, had to work almost without holidays for a month. Owing to their dedicated help, we successfully finished the data taking.

For recent 10 years, Prof. K. Miwa's students, Prof. R. Honda, Mr. Yuuki Matsumoto, Dr. Y. Akazawa, Mr. Takehiro Shiozaki, Mr. Kazuya Kobayashi, Mr. Michihiko Ikeda, Mr. Shotarou Ozawa, Ms. N. Fujioka, Mr. S. Hoshino, Mr. K. Matsuda, and Mr. T. Kitaoka developed detectors and readout systems for J-PARC E40 experiment and compiled them into a very good master's thesis. On the basis of their excellent work, we were able to conduct the experiment and I was able to get the results.

I also thank the staff of the J-PARC accelerator and the Hadron Experimental Facility for their support in providing the beam during beam time.

I want to express my gratitude to all the members of "Experimental Nuclear and Hadronic Physics"(NH) group in Kyoto University, including past constituent members. The staffs, Prof. T. Nagae, Prof. Megumi Naruki, Prof. Juzo Zenihiro, Dr. Toshiyuki Gogami, Dr. Masanori Dozono, Dr. Nastuki, Tomida, Prof. Takahiro Kawabata, Prof. Hiroyuki Fujioka, Prof. Masayuki Niiyama, and Dr. Tetsuya Murakami, run the group and cared about my research. Among seniors who have already graduated, Mr. Shunsuke Kanatsuki and Dr. Hiroyuki Ekawa taught me many things as the seniors of K1.8 beam line members. I have worked with members who got into graduate school after me, Mr. Masaya Ichikawa, Ms. Ami Koshikawa, Ms. Sakiko Ashikaga, Dr. Kazuki Suzuki, Mr. Eiichi Umezaki, Mr. Takeshi Harada, Mr. Tsubasa Ohashi, Mr. Kengo Ebata, and Mr. Shuji Takahashi for experiments at J-PARC or related test experiments. I learned a lot from them, but at the same time I wish I had been helpful to them.

Finally, I am grateful to my parents, Masanori Nanamura and Hiromi Nanamura, for not only emotional but also financial supports during my doctoral course.

Funding resources

J-PARC E40 experiment was supported by JSPS KAKENHI Grant Number 23684011, 15H00838, 15H05442, 15H02079 and 18H03693. This experiment was also supported by Grants-in-Aid Number 24105003 and 18H05403 for Scientific Research from the Ministry of Education, Culture, Science and Technology (MEXT), Japan.

Credits of published paper

This thesis is based on the content of the following academic paper;

T. Nanamura, K. Miwa, et al.,

Measurement of differential cross sections for $\Sigma^+ p$ elastic scattering in the momentum range 0.44-0.80 GeV/c

Progress of Theoretical and Experimental Physics, Volume 2022, Issue 9, September 2022, 093D01 (DOI: 10.1093/ptep/ptac101)

References

[1] T. Hamada, I.D. Hohnston, Nucl. Phys. **34**, 382 (1962).

[2] R. Machleidt, K. Holinde, C. Elster, Phys. Rep. **149**, 1 (1987).

[3] M. Oka, K. Shimizu, Prog. Theor. Phys. **66**, 556 (1981).

[4] M. Oka, K. Shimizu, Prog. Theor. Phys. **66**, 572 (1981).

[5] I. Vidaña, Nucl. Phys. A **914**, 367 (2013).

[6] M. Oka, K. Shimizu, K. Yazaki, Nucl. Phys. A **464**, 700 (1987).

[7] T. Inoue et al., Nucl. Phys. A **881**, 28 (2012).

[8] H. Nemura et al., AIP Conf. Proc. **2130**, 040005 (2019).

[9] S. Saito, Prog. Theor. Phys. **41**, 705 (1969).

[10] H. Walliser, S. Nakaichi-Maeda, Nucl. Phys. A **464**, 366 (1987).

[11] J. Schaffner, Nucl. Phys. A **804**, 309 (2008).

[12] H.T. Cromartie et al., Nature Astronomy **4**, 72 (2020).

[13] D. Lonardoni, A. Lovato, S. Gandol
, F. Pederiva, Phys. Rev. Lett **114**, 092301 (2015).

[14] T.A. Rijken, V.G.J. Stoks, Y. Yamamoto, Phys. Rev. C **59**, 21 (1999).

[15] T.A. Rijken, M.M. Nagels, Y. Yamamoto, Prog. Theor. Phys. **185**, 14 (2010).

[16] D.R. Entem, R. Machleidt, Y. Nosyk, Front. Phys **8**, 57 (2020).

[17] J. Haidenbauer, S. Petschauer, N. Kaiser, U.G. Meißner, A. Nogga, W. Weise, Nucl. Phys. A **915**, 24 (2013).

[18] J. Haidenbauer, U.G. Meißner, A. Nogga, Eur. Phys. J. A **56**, 91 (2020).

[19] Y. Fujiwara, Y. Suzuki, C. Nakamoto, Prog. Part. Nucl. Phys. **58**, 439 (2007).

[20] T. Inoue et al., AIP Conf. Proc. **2130**, 020002 (2019).

[21] P.M.M. Maessen, T.A. Rijken, J.J. de Swart, Phys. Rev. C **40**, 2226 (1989).

[22] M.M. Nagels, T.A. Rijken, Y. Yamamoto, Phys. Rev. C **99**, 044003 (2019).

[23] F. Eisele, H. Filthuth, W. Fölisch, V. Hepp, G. Zech, Phys. Lett. **37B**, 204 (1971).

[24] J.K. Ahn et al., Nucl. Phys. A **648**, 263 (1999).

[25] Y. Kondo et al., Nucl. Phys. A **676**, 371 (2000).

[26] J.K. Ahn et al., Nucl. Phys. A **761**, 41 (2005).

[27] M. Kurosawa et al., Jpn. J. Appl. Phys. **45**, 4204 (2006).

[28] T. Nagae et al., Phys. Rev. Lett. **80**, 1605 (1998).

[29] H. Noumi et al., Phys. Rev. Lett. **89**, 072301 (2002).

[30] P.K. Saha et al., Phys. Rev. C **70**, 044613 (2004).

[31] T. Harada, Y. Hirabayashi, Nucl. Phys. A **759**, 143 (2005).

[32] C.J. Batty et al., Phys. Lett. B **74**, 27 (1978).

[33] G. Backenstoss et al., Z. Phys **A273**, 137 (1975).

[34] R.J. Powers et al., Phys. Rev. C **47**, 1263 (1993).

[35] ALICE Collaboration, Phys. Rev. C **99**, 024001 (2019).

[36] ALICE Collaboration, Phys. Rev. Lett. **123**, 112002 (2019).

[37] ALICE Collaboration, Phys. Lett. B **805**, 135419 (2020).

[38] K. Miwa et al., J-PARC proposal P40 (2011).

[39] Y. Akazawa et al., Nucl. Inst. Meth. A **1029**, 166430 (2022).

[40] K. Miwa et al., Phys. Rev. C **104**, 045204 (2021).

[41] K. Miwa et al., Phys. Rev. Lett. **128**, 072501 (2022).

[42] S. Nagamiya, Nucl. Phys. A **774**, 895 (2006).

[43] S. Nagamiya, Prog. Theor. Exp. Phys **2012**, 02B001 (2012).

[44] H. Ohnishi, F. Sakuma, T. Takahashi, Prog. Part. Nucl. Phys **113**, 103773 (2020).

[45] K. Agari et al., PTEP **2012**, 02B009 (2012).

[46] T. Takahashi et al., PTEP **2012**, 02B010 (2012).

[47] R. Honda, K. Miwa, Y. Matsumoto, N. Chiga, S. Hasegawa, K. Imai, Nucl. Instr. Meth. A **787**, 157 (2015).

[48] J. Myrheim, L. Bugge, Nucl. Inst. Meth. **160**, 43 (1979).

[49] K. Kobayashi, Mater thesis, Osaka University (2017).

[50] S. Hoshino, Mater thesis, Osaka University (2019).

[51] Hadron Universal Logic module User Guide (https://hul-official.gitlab.io/hul-ug-en/).

[52] R. Honda, Ph.D. thesis, Tohoku University (2014). available http://lambda.phys.tohoku.ac.jp/~db/human_resource/thesis/2005_B_3_D_1.pdf.

[53] Geant4 homepage(http://geant4.web.cern.ch/).

[54] S. Morinobu, unpublished.

[55] ANSYS, (htpp://www.ansys.com).

[56] V.V. Avdeichikov et al., Nucl. Instr. Meth. A **336**, 381 (1993).

[57] NN-online homepage, (https://nn-online.org/).

[58] A. Arndt, I.I. Strakovsky, R.L. Workman, Phys. Rev. C **62**, 034005 (2000).

[59] V.F.J. Stoks, R.A.M. Klomp, M.C.M. Rentmeester, J.J. de Swart, Phys. Rev. C **48**, 792 (1993).

[60] N. Hoshizaki, Supplement of the Progress of Theoretical Physics **42**, 107 (1968).

Appendix A

Tables of the differential cross sections

The values of the differential cross sections and their uncertainties are summarized in Table A.1, A.2, A.3.

Table A.1: Data table of differential cross sections for $\Sigma^+ p$ scattering in the low-momentum region ($0.44 < p_\Sigma[\mathrm{GeV}/c] < 0.55$). The systematic error was estimated as a quadratic sum of the error from the background estimation (BG), averaged efficiency (eff), and Σ^+ total flight length (L).

$\cos\theta_{\mathrm{CM}}$	$d\sigma/d\Omega$ [mb/sr]	stat. [mb/sr]	syst. (Total) [mb/sr]	syst. (BG) [mb/sr]	syst. (eff) [mb/sr]	syst. (L) [mb/sr]
$-0.85\pm$ 0.05	2.22	$\pm$0.46	$\pm$0.40	$\pm$0.23	$\pm$0.32	$\pm$0.04
$-0.75\pm$ 0.05	2.31	$\pm$0.32	$\pm$0.33	$\pm$0.17	$\pm$0.28	$\pm$0.05
$-0.65\pm$ 0.05	2.12	$\pm$0.26	$\pm$0.29	$\pm$0.18	$\pm$0.22	$\pm$0.04
$-0.55\pm$ 0.05	2.00	$\pm$0.29	$\pm$0.38	$\pm$0.34	$\pm$0.17	$\pm$0.04
$-0.45\pm$ 0.05	1.93	$\pm$0.27	$\pm$0.43	$\pm$0.41	$\pm$0.13	$\pm$0.04
$-0.35\pm$ 0.05	2.40	$\pm$0.22	$\pm$0.22	$\pm$0.15	$\pm$0.15	$\pm$0.05
$-0.25\pm$ 0.05	1.92	$\pm$0.19	$\pm$0.23	$\pm$0.18	$\pm$0.15	$\pm$0.04
$-0.15\pm$ 0.05	2.22	$\pm$0.19	$\pm$0.31	$\pm$0.25	$\pm$0.17	$\pm$0.04
$-0.05\pm$ 0.05	2.22	$\pm$0.19	$\pm$0.26	$\pm$0.16	$\pm$0.21	$\pm$0.04
0.05$\pm$ 0.05	1.86	$\pm$0.21	$\pm$0.25	$\pm$0.15	$\pm$0.20	$\pm$0.04
0.15$\pm$ 0.05	2.54	$\pm$0.23	$\pm$0.37	$\pm$0.12	$\pm$0.35	$\pm$0.05
0.25$\pm$ 0.05	2.84	$\pm$0.29	$\pm$0.58	$\pm$0.17	$\pm$0.55	$\pm$0.06
0.35$\pm$ 0.05	3.02	$\pm$0.51	$\pm$0.90	$\pm$0.24	$\pm$0.86	$\pm$0.06

Table A.2: Data table of differential cross sections for Σ^+p scattering in the middle-momentum region ($0.55 < p_\Sigma[\mathrm{GeV}/c] < 0.65$).

$\cos\theta_{\mathrm{CM}}$	$d\sigma/d\Omega$ [mb/sr]	stat. [mb/sr]	syst. (Total) [mb/sr]	syst. (BG) [mb/sr]	syst. (eff) [mb/sr]	syst. (L) [mb/sr]
$-0.75\pm$ 0.05	1.24	$\pm$0.38	$\pm$0.22	$\pm$0.17	$\pm$0.13	$\pm$0.02
$-0.65\pm$ 0.05	0.90	$\pm$0.38	$\pm$0.15	$\pm$0.13	$\pm$0.07	$\pm$0.02
$-0.55\pm$ 0.05	1.73	$\pm$0.32	$\pm$0.20	$\pm$0.18	$\pm$0.08	$\pm$0.03
$-0.45\pm$ 0.05	1.24	$\pm$0.28	$\pm$0.06	$\pm$0.04	$\pm$0.04	$\pm$0.02
$-0.35\pm$ 0.05	1.35	$\pm$0.27	$\pm$0.10	$\pm$0.08	$\pm$0.05	$\pm$0.03
$-0.25\pm$ 0.05	1.79	$\pm$0.28	$\pm$0.09	$\pm$0.07	$\pm$0.05	$\pm$0.04
$-0.15\pm$ 0.05	1.42	$\pm$0.23	$\pm$0.07	$\pm$0.06	$\pm$0.02	$\pm$0.03
$-0.05\pm$ 0.05	1.07	$\pm$0.21	$\pm$0.10	$\pm$0.10	$\pm$0.02	$\pm$0.02
0.05$\pm$ 0.05	1.70	$\pm$0.29	$\pm$0.10	$\pm$0.08	$\pm$0.05	$\pm$0.03
0.15$\pm$ 0.05	1.11	$\pm$0.29	$\pm$0.11	$\pm$0.09	$\pm$0.05	$\pm$0.02
0.25$\pm$ 0.05	2.34	$\pm$0.37	$\pm$0.16	$\pm$0.05	$\pm$0.15	$\pm$0.05
0.35$\pm$ 0.05	2.00	$\pm$0.39	$\pm$0.22	$\pm$0.11	$\pm$0.19	$\pm$0.04
0.45$\pm$ 0.05	2.25	$\pm$0.53	$\pm$0.47	$\pm$0.23	$\pm$0.40	$\pm$0.05

Table A.3: Data table of differential cross sections for Σ^+p scattering in the high-momentum region ($0.65 < p_\Sigma[\mathrm{GeV}/c] < 0.80$).

$\cos\theta_{\mathrm{CM}}$	$d\sigma/d\Omega$ [mb/sr]	stat. [mb/sr]	syst. (Total) [mb/sr]	syst. (BG) [mb/sr]	syst. (eff) [mb/sr]	syst. (L) [mb/sr]
$-0.85\pm$ 0.05	0.81	$\pm$0.52	$\pm$0.21	$\pm$0.19	$\pm$0.09	$\pm$0.01
$-0.75\pm$ 0.05	0.58	$\pm$0.39	$\pm$0.41	$\pm$0.40	$\pm$0.04	$\pm$0.01
$-0.65\pm$ 0.05	1.26	$\pm$0.42	$\pm$0.20	$\pm$0.19	$\pm$0.06	$\pm$0.02
$-0.55\pm$ 0.05	0.68	$\pm$0.34	$\pm$0.12	$\pm$0.12	$\pm$0.02	$\pm$0.01
$-0.45\pm$ 0.05	1.08	$\pm$0.33	$\pm$0.09	$\pm$0.08	$\pm$0.02	$\pm$0.02
$-0.35\pm$ 0.05	1.35	$\pm$0.31	$\pm$0.06	$\pm$0.05	$\pm$0.02	$\pm$0.02
$-0.25\pm$ 0.05	1.29	$\pm$0.35	$\pm$0.22	$\pm$0.21	$\pm$0.02	$\pm$0.02
$-0.15\pm$ 0.05	1.58	$\pm$0.44	$\pm$0.10	$\pm$0.09	$\pm$0.01	$\pm$0.02
$-0.05\pm$ 0.05	2.08	$\pm$0.40	$\pm$0.21	$\pm$0.20	$\pm$0.06	$\pm$0.03
0.05$\pm$ 0.05	1.50	$\pm$0.37	$\pm$0.23	$\pm$0.22	$\pm$0.06	$\pm$0.02
0.15$\pm$ 0.05	2.40	$\pm$0.47	$\pm$0.26	$\pm$0.23	$\pm$0.10	$\pm$0.04
0.25$\pm$ 0.05	2.02	$\pm$0.45	$\pm$0.17	$\pm$0.15	$\pm$0.06	$\pm$0.03
0.35$\pm$ 0.05	1.47	$\pm$0.43	$\pm$0.30	$\pm$0.29	$\pm$0.06	$\pm$0.02
0.45$\pm$ 0.05	1.90	$\pm$0.44	$\pm$0.32	$\pm$0.30	$\pm$0.11	$\pm$0.03
0.55$\pm$ 0.05	1.70	$\pm$0.52	$\pm$0.20	$\pm$0.09	$\pm$0.18	$\pm$0.03

Appendix B

Derivation of the integrated cross sections for the $\Sigma^+ p$ elastic scattering with a fine momentum step

In the same way as the differential cross sections, the integrated cross section for the each momentum was calculated directly by the formula

$$\sigma_{-1<\cos\theta_{\mathrm{CM}}<0.5}(p_\Sigma) = \frac{N(p_\Sigma)}{\rho \cdot N_A \cdot L(p_\Sigma) \cdot \bar{\varepsilon}(p_\Sigma)}. \tag{B.1}$$

In this analysis, only the way of projecting ΔE spectrum was different from the case for differential cross sections. Because the events not divided by the scattering angle, data with fine momentum steps of 0.2 GeV/c could be obtained. Figure B.1 shows the fitting results of the ΔE spectra in the evaluation of $N(p_\Sigma)$. Figure B.2, Figure B.3 and Figure B.4 shows the evaluated number of $\Sigma^+ p$ scattering events, averaged efficiency, and total flight length of Σ^+ as a functions of momentum, respectively. The obtained integrated cross sections are shown in Figure B.5. In this figure, the integrated cross sections calculated from the differential cross sections are also plotted. The values of the integrated cross sections and their uncertainty are summarized in Table B.1.

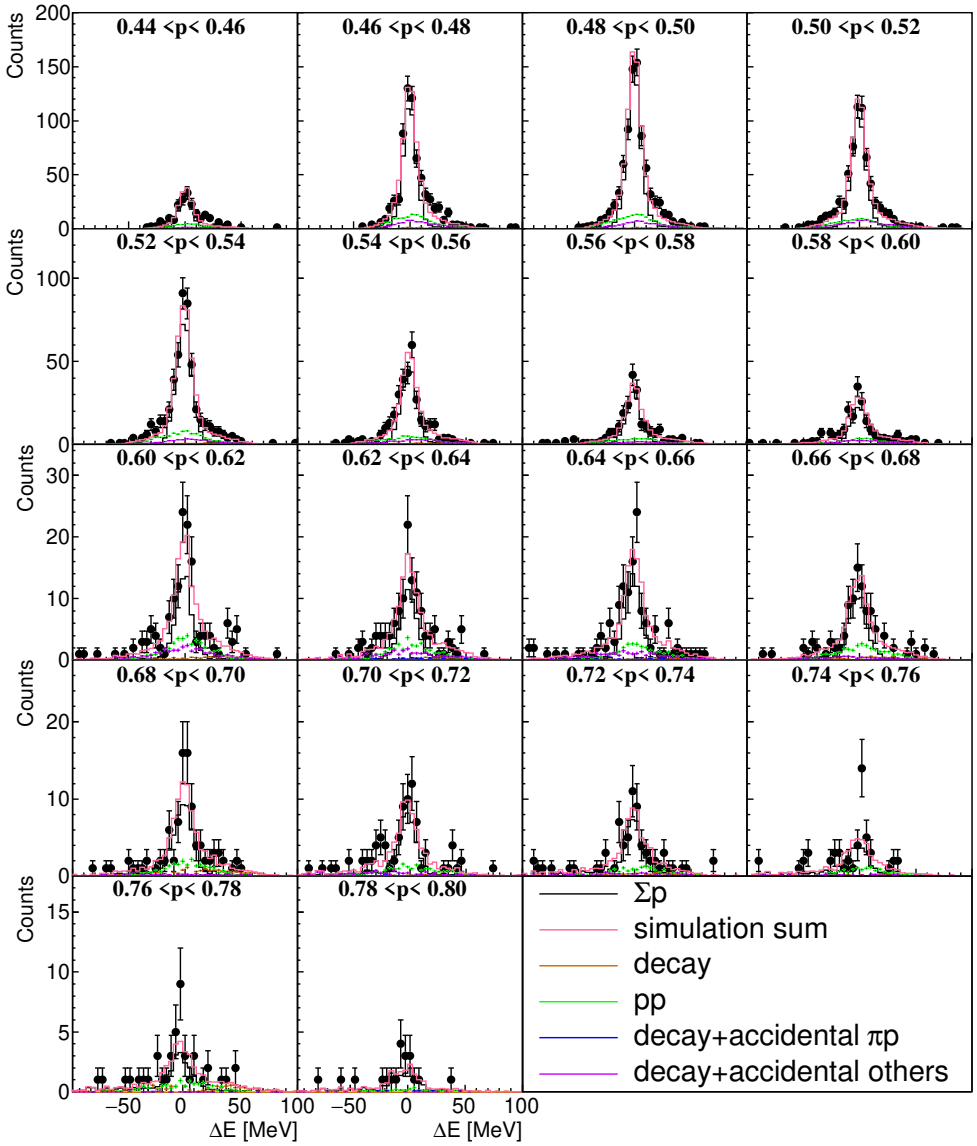

Figure B.1: ΔE spectra for the each fine-divided momentum region.

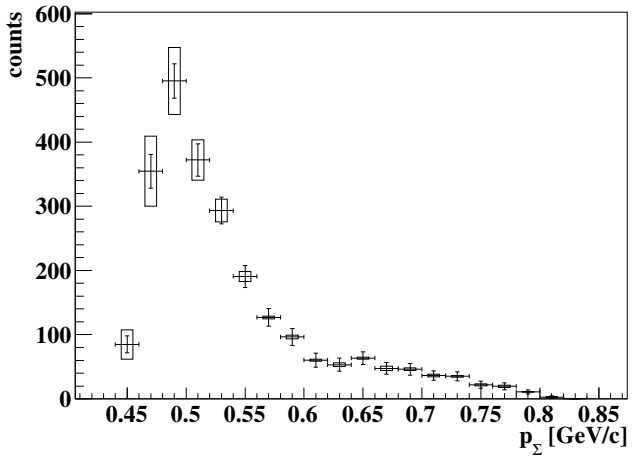

Figure B.2: Evaluated number of $\Sigma^+ p$ scattering $N(p_\Sigma)$ for each momentum.

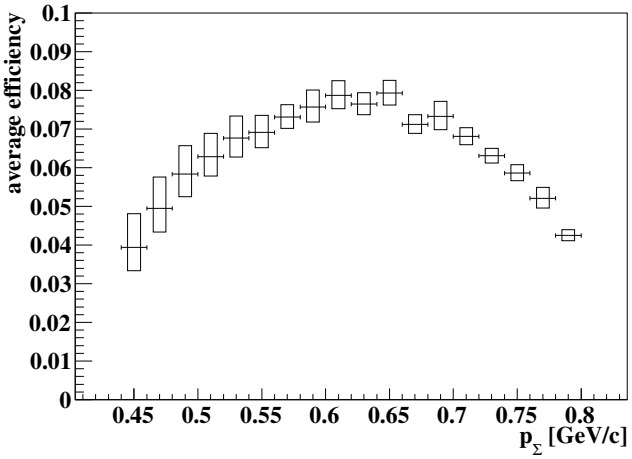

Figure B.3: Averaged efficiency $\bar{\varepsilon}(p_\Sigma)$ for each momentum.

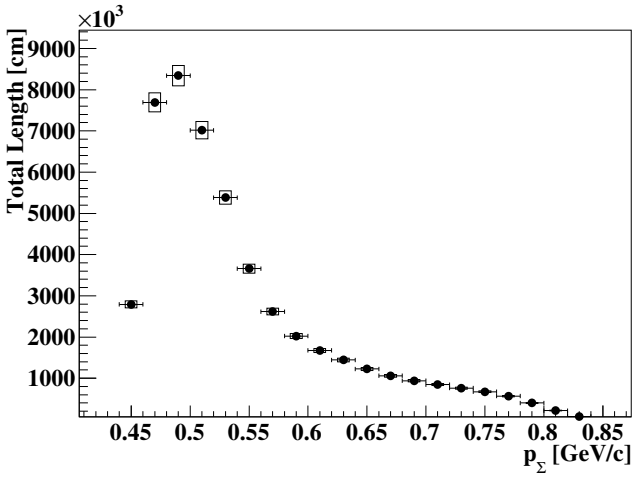

Figure B.4: Total flight length of $\Sigma^+(L(p_\Sigma))$ for each momentum.

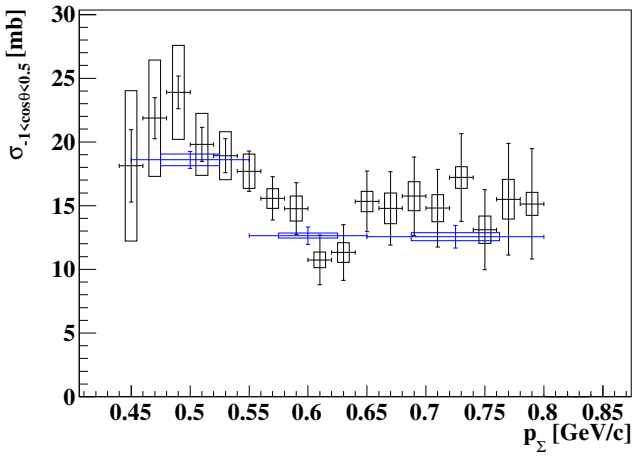

Figure B.5: Integrated cross sections $\sigma_{-1<\cos\theta_{\rm CM}<0.5}(p_\Sigma)$ for the Σ^+p scattering. The blue point represents the integrated cross sections calculated from the differential cross sections. The error bars and boxes show the statistical and systematic uncertainties, respectively.

Table B.1: Data table of the integrated cross section of the $\Sigma^+ p$ elastic scattering. The systematic error was estimated as a quadratic sum of the error from the background estimation (BG), averaged efficiency (eff), and Σ^+ total flight length (L).

p_Σ GeV/c	$\sigma_{-1<\cos\theta_{\rm CM}<0.5}$ [mb]	stat. [mb]	syst. (Total) [mb]	syst. (BG) [mb]	syst. (eff) [mb]	syst. (L) [mb]
0.45± 0.01	18.1	±2.8	±5.9	±4.9	±3.3	±0.4
0.47± 0.01	21.9	±1.6	±4.6	±3.4	±3.1	±0.4
0.49± 0.01	23.9	±1.3	±3.7	±2.5	±2.7	±0.5
0.51± 0.01	19.8	±1.3	±2.4	±1.7	±1.7	±0.5
0.53± 0.01	18.9	±1.3	±1.9	±1.1	±1.5	±0.4
0.55± 0.01	17.7	±1.6	±1.3	±0.7	±1.1	±0.4
0.57± 0.01	15.6	±1.7	±0.8	±0.3	±0.7	±0.3
0.59± 0.01	14.8	±2.0	±1.0	±0.5	±0.8	±0.3
0.61± 0.01	10.7	±1.9	±0.6	±0.3	±0.5	±0.2
0.63± 0.01	11.3	±2.2	±0.8	±0.6	±0.4	±0.2
0.65± 0.01	15.3	±2.4	±0.8	±0.4	±0.6	±0.3
0.67± 0.01	14.8	±2.9	±1.2	±1.1	±0.5	±0.3
0.69± 0.01	15.7	±3.1	±1.1	±0.8	±0.8	±0.3
0.71± 0.01	14.8	±3.0	±1.1	±0.9	±0.5	±0.3
0.73± 0.01	17.2	±3.4	±0.8	±0.6	±0.5	±0.3
0.75± 0.01	13.1	±3.1	±1.1	±0.9	±0.5	±0.3
0.77± 0.01	15.5	±4.4	±1.6	±1.3	±0.8	±0.3
0.79± 0.01	15.1	±4.3	±0.9	±0.7	±0.5	±0.3